

REPORT DOCUMENTATION PAGE			Form Approved OMB NO. 0704-0188		
<p>The public reporting burden for this collection of information is estimated to average 1 hour per response, including the time for reviewing instructions, searching existing data sources, gathering and maintaining the data needed, and completing and reviewing the collection of information. Send comments regarding this burden estimate or any other aspect of this collection of information, including suggestions for reducing this burden, to Washington Headquarters Services, Directorate for Information Operations and Reports, 1215 Jefferson Davis Highway, Suite 1204, Arlington VA, 22202-4302. Respondents should be aware that notwithstanding any other provision of law, no person shall be subject to any penalty for failing to comply with a collection of information if it does not display a currently valid OMB control number.</p> <p>PLEASE DO NOT RETURN YOUR FORM TO THE ABOVE ADDRESS.</p>					
1. REPORT DATE (DD-MM-YYYY) 24-06-2014		2. REPORT TYPE Ph.D. Dissertation		3. DATES COVERED (From - To) -	
4. TITLE AND SUBTITLE EFFECT OF TRANSLAMINAR REINFORCEMENTS AND HYBRIDIZATION ON DAMAGE RESISTANCE AND TOLERANCE OF COMPOSITE LAMINATES				5a. CONTRACT NUMBER W911NF-08-1-0120	
				5b. GRANT NUMBER	
				5c. PROGRAM ELEMENT NUMBER 611102	
6. AUTHORS Min Cheol Song				5d. PROJECT NUMBER	
				5e. TASK NUMBER	
				5f. WORK UNIT NUMBER	
7. PERFORMING ORGANIZATION NAMES AND ADDRESSES University of Florida Office of Engineering 339 Weil Hall  Gainesville, FL 32611 -6550				8. PERFORMING ORGANIZATION REPORT NUMBER	
9. SPONSORING/MONITORING AGENCY NAME(S) AND ADDRESS (ES) U.S. Army Research Office P.O. Box 12211 Research Triangle Park, NC 27709-2211				10. SPONSOR/MONITOR'S ACRONYM(S) ARO	
				11. SPONSOR/MONITOR'S REPORT NUMBER(S) 52873-EG.13	
12. DISTRIBUTION AVAILABILITY STATEMENT Approved for public release; distribution is unlimited.					
13. SUPPLEMENTARY NOTES The views, opinions and/or findings contained in this report are those of the author(s) and should not be construed as an official Department of the Army position, policy or decision, unless so designated by other documentation.					
14. ABSTRACT It was shown that the damage resistance and tolerance of laminated composites can be enhanced by the employment of translaminar reinforcements (TLR) such as stitching, z-pinning and 3D weaving and also by hybrid composites. A non-dimensional analytical model focused on Mode I delamination was developed to understand the role of the TLR on delamination behavior. An explicit formula for the apparent interlaminar fracture toughness was derived in terms of the					
15. SUBJECT TERMS Composite Laminates Resistance					
16. SECURITY CLASSIFICATION OF:			17. LIMITATION OF ABSTRACT UU	18. NUMBER OF PAGES	19a. NAME OF RESPONSIBLE PERSON Bhavani Sankar
a. REPORT UU	b. ABSTRACT UU	c. THIS PAGE UU			19b. TELEPHONE NUMBER 352-392-6749

## Report Title

# EFFECT OF TRANSLAMINAR REINFORCEMENTS AND HYBRIDIZATION ON DAMAGE RESISTANCE AND TOLERANCE OF COMPOSITE LAMINATES

## ABSTRACT

It was shown that the damage resistance and tolerance of laminated composites can be enhanced by the employment of translaminar reinforcements (TLR) such as stitching, z-pinning and 3D weaving and also by hybrid composites.

A non-dimensional analytical model focused on Mode I delamination was developed to understand the role of the TLR on delamination behavior. An explicit formula for the apparent interlaminar fracture toughness was derived in terms of the inherent fracture toughness of original materials and the bridging force due to z-pins. This model is capable of estimating the apparent fracture toughness, the bridging length and allowable bridging force thus can be useful in the design of TLR for composite laminates.

Along with understanding advantages of TLR in increasing the damage tolerance of laminated composites, the damage behavior of laminated composites subjected to low velocity impact loading was studied. Based on the similarity in damage development between quasi-static and dynamic loadings observed through the short beam shear (SBS) tests, the FE analyses of the SBS specimens for quasi-static indentation and at several rates of low-velocity impact loadings were performed. The results reveal that inertia effects in the typical velocity range of the striker in SHPB, around 10m/s, can be negligible, and hence the quasi-static analysis is useful and valid in the study of damage in composite specimens under low velocity impact loading.

The delamination behavior of 3D woven composites was investigated focusing on the effect of z-yarn. The 3D woven composites containing both single and double z102 yarns were chosen and compared with the 2D plain woven laminate. The double z-yarn woven composite exhibited enhanced damage tolerance compared to the single z-yarn and the plain woven laminate. The relative sliding motion between two layers is constrained by z-yarns thus the crack propagation of delamination is suppressed. This mechanism increases the apparent interlaminar fracture toughness of the composites. The interlaminar shear stress profiles in the various hybrid composites were obtained from linear FE analyses and compared within the framework of damage resistance. Some hybrid configurations resulted in reduced maximum shear stress value for a given contact force thus demonstrating higher damage resistance. Although matrix cracks may change the location of delamination and decrease damage resistance, hybrid composites can still be superior in structural applications.

EFFECT OF TRANSLAMINAR REINFORCEMENTS AND HYBRIDIZATION ON  
DAMAGE RESISTANCE AND TOLERANCE OF COMPOSITE LAMINATES

By

MIN CHEOL SONG

A DISSERTATION PRESENTED TO THE GRADUATE SCHOOL  
OF THE UNIVERSITY OF FLORIDA IN PARTIAL FULFILLMENT  
OF THE REQUIREMENTS FOR THE DEGREE OF  
DOCTOR OF PHILOSOPHY

UNIVERSITY OF FLORIDA

2012

© 2012 Min Cheol Song

To my family

## ACKNOWLEDGMENTS

I would like to express my deepest gratitude to my advisor Dr. Bhavani V. Sankar for his full support and excellent guidance through my years in graduate school. I would like to thank Dr. Ghatu Subhash for his supervision at my project meeting every week. I also would like to acknowledge my committee members Dr. John J. Mecholsky Jr. and Dr. Peter G. Ifju for their advice on my research and dissertation.

I would like to acknowledge Dr. Chian-Fong Yen at the U.S. Army Research Laboratory for the financial support for this project. I would like to thank Dr. Timothy R. Walter and Dr. Madhwapati Prabhakar Rao for their discussion and many suggestions. I also thank my fellow graduate students at the Center for Advanced Composites at the University of Florida.

I sincerely thank my parents for their love, support and encouragement. Finally I am very grateful to my beloved wife Jiyeon Sung, my son Dongkun Song and my daughter Lily Chaerin Song for their devotion and sacrifice.

## TABLE OF CONTENTS

	<u>page</u>
ACKNOWLEDGMENTS.....	4
LIST OF TABLES.....	7
LIST OF FIGURES.....	8
ABSTRACT .....	11
 CHAPTER	
1 INTRODUCTION .....	13
Motivation .....	13
Review of Research Approach .....	16
Representation of Bridging Zone.....	17
Delamination Modeling using FEM.....	19
Application of the Bridging and Delamination Model for a Z-pinned Composite.....	21
Static Indentation and Low-Velocity Impact.....	22
Damage Behavior in Woven Composites during Short Beam Shear Test.....	22
2 ANALYSIS OF MODE I DELAMINATION OF Z-PINNED COMPOSITE USING A NON-DIMENSIONAL ANALYTICAL MODEL .....	29
Non-Dimensional Analytical Model .....	30
Verification .....	35
A Sample Problem for Verifying the Non-Dimensional Analytical Model .....	35
A FE Simulation for Verifying the Non-Dimensional Analytical Model .....	37
Discussion of Results from the Non-Dimensional Model .....	39
Parametric Studies using the Non-Dimensional Analytical Model .....	39
Maximum Allowable Translaminar Reinforcement .....	40
Effect of Tri-Linear Bridging Law .....	42
Summary and Conclusions .....	43
3 APPLICABILITY OF QUASI-STATIC ANALYSIS FOR LOW VELOCITY IMPACT .....	52
Finite Element Analyses .....	53
Results.....	54
4 ANALYSIS OF DELAMINATION IN 3D WOVEN COMPOSITES UNDER QUASI-STATIC LOADING USING FINITE ELEMENTS.....	59
Finite Element Model for 3D Woven Composites .....	59

Geometry and Boundary Conditions .....	61
Damage Model and Modeling Strategy .....	63
Material Property and Data Selection .....	65
Finite Element Model for 2D Plain Woven Laminates .....	67
Results and Discussions .....	68
3D Woven Composites (SY3W and DY3W) .....	68
Plain Woven Laminated Composites (2DPL) .....	69
Summary and Conclusion .....	72
 5 DAMAGE RESISTANCE OF HYBRID COMPOSITES WITH FUNCTIONALLY GRADED MATERIALS .....	 83
Effect of Hybrid Composites on Reducing the Maximum Shear Stress .....	84
Finite Element Model for Maximum Shear Stress .....	84
Results and Discussion .....	85
Delamination Behavior of Hybrid Composites under a Quasi-static Indentation .....	86
Finite Element Model for Delamination .....	86
Results .....	87
Conclusions .....	89
 6 CONCLUSIONS AND FUTURE WORK .....	 101
Conclusions .....	101
Recommendations for Future Work .....	102
 LIST OF REFERENCES .....	 104
 BIOGRAPHICAL SKETCH .....	 111



## LIST OF TABLES

<u>Table</u>	<u>page</u>
1-1 Summary of results obtained by various researchers and present study. ....	28
2-1 The various dimensions and properties of the DCB used in the numerical simulation .....	51
3-1 Material properties of the DSBS specimen for FEA.....	58
4-1 Dimensions of geometric model of RVE .....	82
4-2 Material properties of the constituents the 3D woven composites .....	82
4-3 Elastic properties for plain woven composites .....	82
4-4 Parameters for cohesive element in baseline composite model .....	82
5-1 Various hybrid composite laminates and FGM .....	98
5-2 Elastic properties for composite materials in the FEM.....	100

## LIST OF FIGURES

<u>Figure</u>	<u>page</u>
1-1 Schematics of composites reinforced by the TLR.....	23
1-2 NASA and Boeing's advanced stitching machine.....	24
1-3 Inserting of z-pin.....	24
1-4 3D weaving machine .....	24
1-5 Schematics of 3D woven composites .....	25
1-6 Hybrid composites .....	25
1-7 Schematic of bridging zone developed during delamination.....	25
1-8 Bridging laws of TLR. ....	25
1-9 Spring model for bridging zone.....	26
1-10 Traction- separation law for the cohesive element. ....	26
1-11 Quasi-static SBS test setup.....	26
1-12 Damages after SBS test. ....	27
2-1 Schematic of initial geometry and development of bridging zone by z-pins in the composite DCB.....	45
2-2 Idealization of bridging zone using a beam model.....	45
2-3 Force-displacement relation of the z-pin.....	46
2-4 Flowchart of the procedures for solving the non-dimensional governing equation.....	46
2-5 DCB specimen reinforced by z-pins .....	47
2-6 Load and crack length variation as a function of DCB deflection.....	47
2-7 Bridging length and crack length as a function of DCB deflection. ....	48
2-8 Variation of apparent fracture toughness during crack propagation. ....	48
2-9 Traction- separation law for the cohesive element. ....	48
2-10 Cohesive and spring elements in the FE model of the DCB.....	49

2-11	Non-dimensional steady state bridging length. ....	49
2-12	Apparent fracture toughness as a function of maximum friction force and interlaminar fracture toughness. ....	49
2-13	Comparison of strain with different loading types. ....	50
2-14	The tri-linear bridging law. ....	50
2-15	Load-deflection curve from various bridging laws.....	51
3-1	Short beam shear test. ....	56
3-2	2D FE Model for the SBS test.....	56
3-3	2D FE Model for the SBS test.....	57
3-4	Load-displacement curves at the indenter.....	57
3-5	Load-displacement curves at the indenter.....	58
3-6	Shear stress profiles.....	58
4-1	3D woven composites for FE model.. ....	73
4-2	Geometric parameter of RVE. ....	73
4-3	Prediction of matrix cracks.. ....	74
4-4	Traction-separation law of cohesive element.....	75
4-5	2D plain woven composite.....	75
4-6	Implementation of the cohesive element on homogenized 2D plain woven composite. ....	75
4-7	Force-displacement curves of the single/double z-yarn 3D woven composites..	76
4-8	Strain energy and damaged energy versus displacement curves of the SY3W and DY3W. ....	76
4-9	Force-displacement curves of the single and double z-yarn 3D woven composites. ....	77
4-10	Strain energy and damage energy versus displacement curves of the 2DPW... ..	77
4-11	Damage evolution of baseline composite-Case I.....	78
4-12	Damage evolution of baseline composite-Case II.....	79

4-13	Damage evolution of baseline composite-Case III.....	80
4-14	Delamination patterns in the composites.....	81
5-1	FE model to determine the shear stress profile .....	89
5-2	Shear stress profiles of the hybrid composites stiffened on the loading side.....	90
5-3	Shear stress profiles of the hybrid composites stiffened on the free side .....	90
5-4	Shear stress profiles of the hybrid composites stiffened on the top and bottom sides .....	91
5-5	Shear stress profiles of homogeneous the FGMs.....	91
5-6	The maximum shear stress of various composites.....	92
5-7	The DSFGM specimen.. .....	92
5-8	Comparison of peak loads of various specimens with and without matrix cracks .....	93
5-9	The GFC.....	93
5-10	The CFC.....	93
5-11	The LS9Hybrid composite.. .....	94
5-12	The LS18Hybrid composite.. .....	94
5-13	The LS36Hybrid composite.. .....	94
5-14	The LSFGM composite.....	95
5-15	The FS9Hybrid composite.. .....	95
5-16	The FS18Hybrid composite.. .....	95
5-17	The FS36Hybrid composite.. .....	96
5-18	The FSFGM composite.. .....	96
5-19	The DS9Hybrid composite.....	96
5-20	Load-displacement curves.....	97

Abstract of Dissertation Presented to the Graduate School  
of the University of Florida in Partial Fulfillment of the  
Requirements for the Degree of Doctor of Philosophy

EFFECT OF TRANSLAMINAR REINFORCEMENTS AND HYBRIDIZATION ON  
DAMAGE RESISTANCE AND TOLERANCE OF COMPOSITE LAMINATES

By

Min Cheol Song

December 2012

Chair: Bhavani V. Sankar  
Cochair: Ghatu Subhash  
Major: Mechanical Engineering

The effects of translaminar reinforcements (TLR) and hybridization on impact damage resistance and damage tolerance of laminated composites were analyzed. The TLR increase the apparent fracture toughness of composite laminates and contribute to improved impact properties. Analytical and computational methods were used to investigate the damage of laminated composites with special focus on delamination. A non-dimensional analytical model for mode I delamination of z-pinned composites was developed and verified using finite element (FE) analysis. The analytical and FE models were compared with experimental results to evaluate the adequacy of the model in describing the role of translaminar reinforcements. The influence of the TLR on the apparent fracture toughness and bridging length was quantitatively investigated through parametric studies. The maximum allowable bridging force before inherent failure of the material was suggested as well.

A 3D woven composite was chosen to study the effect of z-yarns on impact damage. A detailed analysis was performed to understand the limitations of quasi-static analysis in low-velocity impact studies. The static equilibrium and shear stress evolution

in a beam made of orthotropic material subjected to quasi-static and impact loadings under various impact speeds were compared. The maximum impact velocity for which static analyses are adequate was determined.

Short beam shear (SBS) test specimens of plain woven laminated composite and 3D woven composites were analyzed for the purpose of evaluating the effect of z-yarns on delamination. The FE model, that considered both intralaminar and interlaminar fracture, predicted damage patterns (transverse cracks and delaminations) observed in the tests. The z-yarns in the composites increase damage tolerance by interrupting crack propagation.

Finally, the advantage of hybridization of laminate composites was evaluated using the FE models. Some hybrid composites reduce the maximum interlaminar shear stress in beam-type specimens, and therefore enhance the damage resistance of composite laminates. Suggestions for continuing this study in the future are included at the end.

## CHAPTER 1 INTRODUCTION

### **Motivation**

Composite materials are a combination of two or more materials with properties that cannot be achieved by any one of the constituent materials [Gibson 1994]. Composite laminates have been widely used in aerospace and automobile structures, sporting goods and military equipment because of their superior in-plane stiffness and strength. However, fiber composites are anisotropic, showing relatively low stiffness and strength in directions other than the fiber direction. In the case of laminated composites, delamination, i.e., separation of layers or plies, is one of the most significant damage modes, and is a key element of consideration in the design and operation of composite structures. Toughened resins can solve this problem to some extent. Rubber [Kumar and Singh 2000, Yan et al. 2002] or thermoplastic toughened epoxy [Wong et al. 2010] is an example of such an approach. Recently nano-particles have been added to the resin phase to improve the fracture toughness [Kalarikkal et al. 2006, Kim et al. 2008, Boesl et al. 2011]. However, the improvement in interlaminar fracture toughness due to the above mechanisms is not significant. Another method of improving interlaminar properties is the introduction of reinforcements in the thickness or z-direction. These are called translaminar reinforcements (TLR) which seem to increase the fracture toughness and strength by an order of magnitude. Thus, there seems to be a tremendous interest in TLR for laminated composites.

Stitching, z-pinning and 3D weaving are some of the methods by which TLR can be provided into composite laminates. Stitched composites can be manufactured by passing a sewing needle with a thread or yarn, looping or interlocking with bobbin

thread, through laminates (Figure 1-1A). Several researchers have studied delamination resistance and damage tolerance of stitched composites under Mode I, Mode II and Mixed Mode loading [Sharma and Sankar 1997, Chen et al. 2005, Dransfield et al. 1998, Sankar and Zhu 2000, Jang and Sankar 2005, Rys et al. 2010]. In general, stitching reduces the in-plane stiffness and strength properties [Dransfield 1994, Mouritz 1997, 2004]. Although stitching was found to reduce the impact damage resistance, it significantly improved the impact damage tolerance [Sharma and Sankar 1997] and compression after impact (CAI) [Farley et al. 1992].

Z-pinning is a form of TLR similar to stitching in which rigid rods or pins are inserted through the thickness of the composite structure (Figure 1-1B). It is an alternative method to stitching and suitable for thick composites and sandwich structures [Wallace et al. 2001]. The z-pinning process using an ultrasonic insertion device is efficient when pre-pregs are used [Lander 2008]. Z-pin increased the ultimate strength of joints [Byrd and Birman, Chang et al. 2006] while degrading in-plane stiffness and strength [Mouritz 2007, Steeves 2006, Chang et al. 2007]. Increase in interlaminar fracture toughness in z-pinned composites is due to the pull out mechanism of the pins and it depends only on the frictional and cohesive forces between the reinforcement and surrounding matrix material [Cartie 2000, Cartie et al. 2004, 2006, Dai et al. 2004]. However, it is not as effective as stitching as the ends of the z-pins are not anchored as in stitching.

Although stitching is a practical method of improving interlaminar properties, the reduction in in-plane properties due to damage to the composite preforms during the stitching process has become a matter of concern. At the same time developments in



textile technology has lead to advanced weaving and braiding processes which can produce three dimensionally reinforced composites. Textile processes are well developed, fast and easy to implement. Complicated performs could be made using textile processes where separate steps to implement TLR into 3D woven composites ((Figure 1-1C) are not necessary. One single weaving process can texture warp yarns (0-degree tows), weft yarns (90-degree tows) and z yarns concurrently.

Some of the 3D performs are: 3D orthogonal weave, layer to layer interlock, and angle interlock (Figure 1-5). From early on it has been recognized that 3D braided [Gong and Sankar 1991] and 3D woven composites [Brandt et al. 1996, Byun et al. 1990, Walter et al. 2010] improve impact properties and damage tolerance of composites. However, there has been no systematic study to understand the effectiveness of various 3D architectures mentioned above on the impact properties of composites. This can be studied either by experimental testing – by testing various woven architectures under various impact loading conditions or by simulating their behavior. The simulations could be performed using either analytical models or computational models. Analytical models are based on several simplifying assumptions and hence tend to be approximate. However, they are useful in revealing the important physical mechanisms that are responsible for the improvements in the impact behavior. They are also useful in optimization studies which require thousands of Monte Carlo simulations. Computational models use the finite element analysis. They tend to be more realistic. However, they are expensive and time consuming. In this research we propose to use both analytical and computational models to understand the effect of TLR in various 3D woven composites.

Hybrid composites also are capable of enhancing impact resistance [Wang et al. 1991] and interlaminar fracture toughness [Hwang and Huang 1999]. Numerous combinations with a variety of fibers and resins are possible in improving composite properties (Figure 1-6). The hybrid composites using carbon and glass woven fabrics shows superior in-plane properties [Pandya et al. 2011] and CAI [Naik et al. 2001] compared to glass woven fabric. And the carbon/glass hybrid composites have increased failure strain [Stevanovic, 1992]. Combination of Kevlar fiber composites and carbon fiber composites possess superior ballistic performance in armor applications [Grujicic et al. 2006].

The present study is concerned with the effect of TLR on the damage resistance and damage tolerance of composite laminates. Damage resistance (specifically impact damage resistance in the present context) is the ability of the material to function without undergoing significant damage as exhibited by the loss of stiffness or strength when subjected to a certain load. Damage tolerance pertains to material that is already damaged. Damage tolerance is the ability of the material that has sustained some damage to continue to perform and carry loads albeit with reduced stiffness of the structure. The advantages of hybrid composites - both inter-ply and intra-ply hybrid composites and functionally graded composites - will be evaluated.

### **Review of Research Approach**

In the following we discuss the technical challenges in solving the proposed problem and the approach we will take to address those challenges.

The major issues in the analytical model of TLR composites are to identify the interactions between the z-reinforcement and the surrounding composite and to represent them using appropriate mathematical models. In computational models,

damage modes should be defined and appropriate numerical strategy to represent the damage needs to be developed. The way to model delamination between layers of composites is crucial since impact resistance and damage tolerance are significantly affected by delamination. At the same time intralaminar failure should be considered since this failure mode seems to interact with interlaminar delamination. In order to characterize the effect of z-yarn on impact resistance and damage tolerance, the mechanism of damage initiation and evolution will be investigated by simulation of the static short beam shear (SBS) test, since static indentation tests are useful in understanding low velocity impact behavior. Experimental studies have indicated that damage mechanisms in static indentation and dynamic impact tests are similar and one can learn more from static tests about impact damage.

### **Representation of Bridging Zone**

One of the biggest characteristics during delamination of composites reinforced by TLR is the development of the bridging zone denoted by length  $c$  in Figure 1-7.

The bridging zone can be regarded as a process zone where extra energy is dissipated due to the failure of TLR. In other words, the energy to create delamination in transversely reinforced composites is higher than that for original unreinforced composites. This increase in energy required increases the delamination resistance. This increase due to TLR can be quantified by comparing fracture toughness. The relationship between the two values of the fracture toughness – that of reinforced composites with TLR and unreinforced composites - is given by

$$G_{c-app} = G_c + \Gamma \quad (1-1)$$

where  $G_{c-app}$  and  $G_c$ , respectively, are the apparent fracture toughness of reinforced composites with TLR and the fracture toughness of the original composite; and  $\Gamma$  is the energy dissipation rate due to the deformation and failure of TLR.

So, an analysis of the bridging zone can provide an understanding of the effect of TLR on delamination. The behavior of the entire bridging zone must be characterized by failure mechanisms or a bridging law for each TLR. Experiments [Tan et al. 2010, Dai et al. 2004] have been conducted to measure the bridging law. It has been found that a simple force-displacement relationship of the z-reinforcement could describe the effect of TLR with sufficient accuracy. Moreover, bridging laws of TLR can be idealized as linear elastic and linear softening (linearly decreasing function) laws for stitching and z-pinning, respectively.

The use of spring elements is very adequate and efficient since their behavior can be defined by a force-displacement relationship and makes it possible to simplify analysis. The spring elements with these bridging laws are capable of being directly implemented into double cantilever beam specimens (DCB) or end notch flexure (ENF) specimens since the relative displacement at the two end nodes can be related to the deflection of beam. So the DCB and ENF specimens incorporating spring elements have been used for representing Mode I and Mode II fracture using analytical model or finite element analysis (FEA). Discrete spring models and distributed traction models are available for these applications. The discrete spring models [Ratcliffe and O'brien 2004] place spring elements discretely to represent TLR while the distributed traction model [Sankar and Dharmapuri 1998, Sankar and Zhu 2000, Mabson and Deobald

2000, Sridhar et al. 2002, Robinson and Das 2004, Byrd and Birman 2005] uses continuous elements obtained by smearing the discrete forces.

### **Delamination Modeling using FEM**

In order to demonstrate delamination using FEM, J-integral [Rice 1968] and virtual crack closure technique (VCCT) based on fracture mechanics [Rybicki et al. 1977, Krueger 2002, Grassi and Zhang 2003] or the cohesive zone method (CZM) based on damage mechanics have been widely used. The CZM has advantages in that it is not necessary to define a pre-existing crack while the methods based on fracture mechanics require pre-existing cracks with which strain energy release rate (SERR) can be calculated and used in a fracture criterion. However, The CZM is also related to fracture mechanics since dissipated energy of cohesive elements is the same as fracture toughness of the material, and this fact makes it possible to model delamination. The CZM was introduced by Barenblatt [Barenblatt 1962] and Dugdale [Dugdale 1960]. The traction-separation law is a commonly adopted approach to describe behaviors of the cohesive zone. Several traction-separation laws [Tvergaard and Hutchinson 1992, Xu and Needleman 1994, Camacho and Ortiz 1996] were suggested. Among them, the bi-linear traction-separation laws [Geubelle and Baylor 1998] and have extensively used for delamination problems in Mode I, Mode II and Mixed mode problems. The bi-linear traction-separation law is depicted in Figure 1-10 and can be defined as

$$\sigma = (1 - D)Kd$$

$$D = \begin{cases} 0 & , d < d_0 \\ \frac{d_f (d - d_0)}{d (d_f - d_0)} & , d_0 < d < d_f \\ 1 & , d_f < d \end{cases} \quad (1-2)$$

where  $\sigma$  is traction,  $K$  is stiffness,  $D$  is damage variable,  $d$  is displacement,  $d_0$  is the displacement at damage initiation and  $d_f$  is the final displacement [Davila et al. 2007].

The damage behavior of the cohesive element incorporating the bi-linear traction-separation law can be defined by parameters – cohesive strength, critical displacement and fracture toughness among which only two parameters are independent, as the area under the stress-displacement diagram should be equal to the fracture toughness. In addition to the above three parameters, the initial stiffness or the penalty stiffness is also a crucial parameter that affects the compliance of the structure. The criteria for damage onset and propagation should be defined for progressive delamination modeling. Quadratic stress based failure criterion [Cui et al. 1992] given in Eq. (1-3) below has been used for delamination onset:

$$\left\{ \frac{\langle \sigma_n \rangle}{\sigma_n^o} \right\}^2 + \left\{ \frac{\sigma_s}{\sigma_s^o} \right\}^2 = 1 \quad (1-3)$$

where  $\sigma_n^o$  and  $\sigma_s^o$  are the interlaminar normal and shear strengths.

Power law criterion [Wu and Reuter 1965] (Eq. 1-4) and B-K criterion [Benzeggagh and Kenane 1996] (Eq. 1-5) are well established for damage propagation

$$\left\{ \frac{G_I}{G_{IC}} \right\}^\alpha + \left\{ \frac{G_{II}}{G_{IIC}} \right\}^\alpha = 1 \quad (1-4)$$

where  $\alpha$  is a material constant and

$$G_{IC} + (G_{IIC} - G_{IC}) \left( \frac{G_{II}}{G_T} \right)^\eta = G_C \quad (1-5)$$

where  $\eta$  is a material constant and  $G_T = G_I + G_{II}$ .

### **Application of the Bridging and Delamination Model for a Z-pinned Composite**

The FE models incorporating the cohesive element as well as the failure of TLR have been used for the simulation of progressive delamination behavior of DCB reinforced by TLR [Ratcliffe and Krueger 2006, Dantuluri et al. 2007]. The z-pinned composite subjected to Mode I loading has been studied, since the debonding of skin-stiffener T-joint is one of the main issues for designers. This analysis can provide direct insights in understanding the role of the TLR to damage tolerance by evaluating apparent fracture toughness.

A summary of past work in this area is provided in Table 1-1. In the following we briefly describe the salient features of the work listed in that table. Cartie [Cartie 2000] suggested a bi-linear bridging law through experiments and conducted FE simulation using plain strain elements. Robinson and Das [Robinson and Das 2004], Mabson and Deobald [Mabson and Deobald 2000] and Byrd and Birman [Byrd and Birman 2005] used a linear softening bridging model whereas Ratcliffe and O'Brien [Ratcliffe and O'Brien 2004] proposed a discrete element analytical model. For delamination modeling of z-pinned DCB, Dantuluri et al. [Dantuluri et al. 2007] used 2D cohesive elements

incorporating beam elements and a bi-linear bridging law. Ratcliffe and Krueger [Ratcliffe and Krueger 2006] used 3D cohesive model with solid elements. Grassi and Zhang [Grassi and Zhang 2003] used VCCT for delamination modeling. It is clear from the table that various researchers have used different approaches in modeling the stated problem.

### **Static Indentation and Low-Velocity Impact**

Numerous studies have shown [Kwon and Sankar 1993, Nettles and Douglas 2000] that static indentation tests and simulations are useful in understanding low velocity impact behavior. As long as the mass of the impactor is higher than the target mass, beam mass in the present case, and the impact velocity is much less than the velocity of wave propagation in the target medium, the impact can be considered as low velocity impact. In such cases static tests and analyses provide good information on forces at which damage initiates and also the residual stiffness which is a measure of damage tolerance.

### **Damage Behavior in Woven Composites during Short Beam Shear Test**

SBS test is a test method used to determine interlaminar shear strength (ILSS). SBS tests for various 3D woven composites were conducted to investigate the effect of z-yarns on ILSS and post-damage behavior. The test results revealed that delamination is a predominant damage mode, and the damage tolerance became high as the volume fraction of z-yarns increased. However, with the increased amount of z-yarns interlaminar shear strength decreased and the delaminations were contained, leading to post-damage behavior different from that of plain woven laminated composites [Walter et al. 2010].



One of the significant attributes of damage evolution was that matrix cracks occurred at the early stage of loading and induced interlaminar delamination. However, most matrix cracks developed inside of weft yarns (90-degree tows) as shown in Figure 1-12 where ellipses indicate the matrix phase. This damage pattern is a common feature in cross-ply laminated composites [0/90], where transverse cracks initiate in 90-degree plies followed by delamination between 90-degree ply and 0-degree ply [Geubelle and Baylor 1998, Ling et al. 2011]. In fact each of the yarns in a 3D woven composite can be regarded as a unidirectional composite, which is weak in the transverse direction. Therefore the effect of parameters such as interlaminar shear strength, interlaminar fracture toughness and transverse strength of yarns on damage initiation and evolution should be investigated.

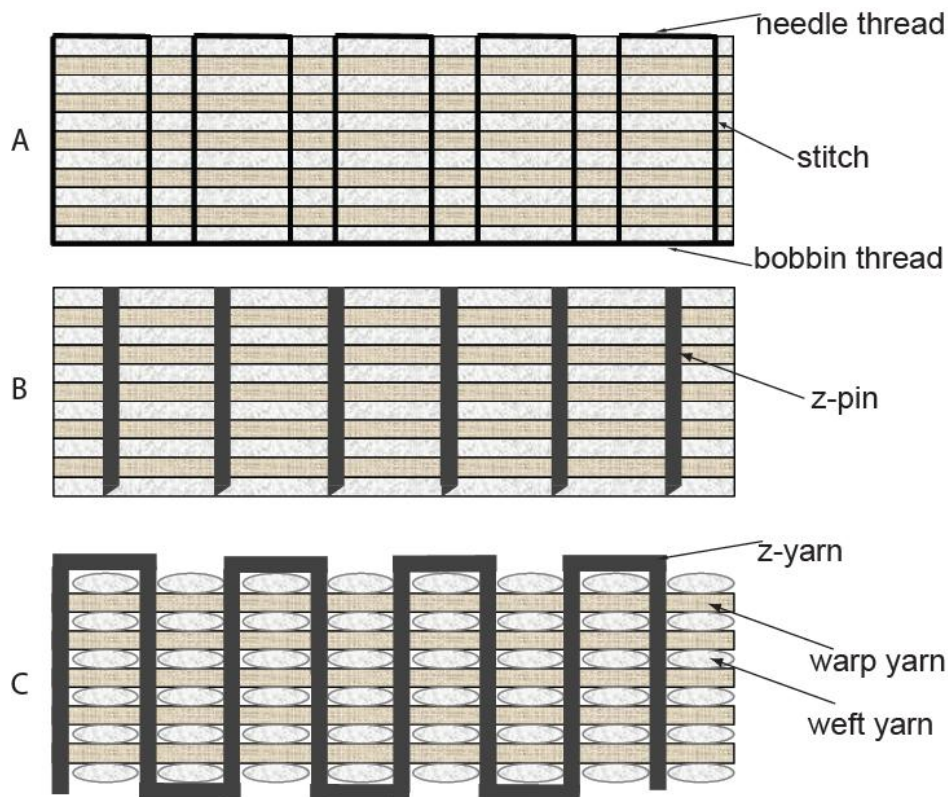


Figure 1-1. Schematics of composites reinforced by the TLR. A) Stitched. B) z-pinned. C) 3D woven. [Mouritz 2008].



Figure 1-2. NASA and Boeing's advanced stitching machine [Lander 2008].

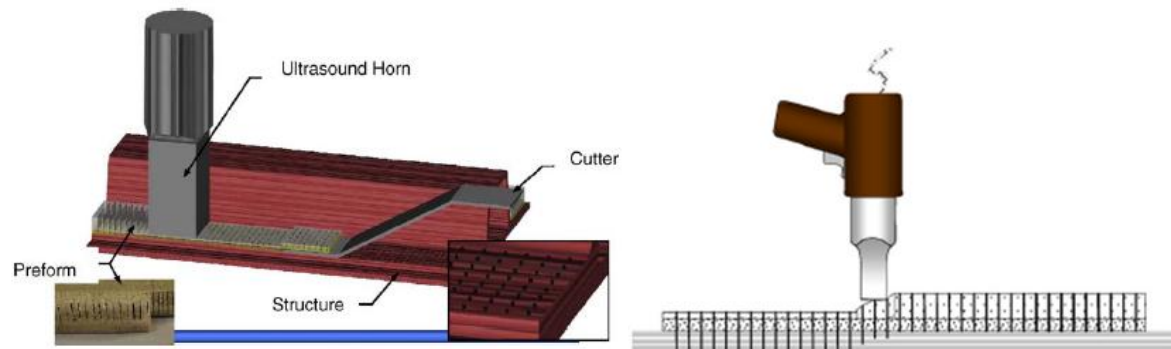


Figure 1-3. Inserting of z-pin [Cartie 2000, Mouritz 2007].

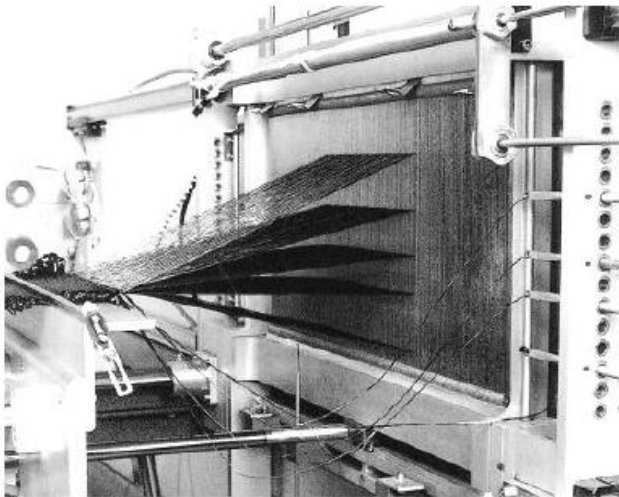


Figure 1-4. 3D weaving machine [Brandit 2001].

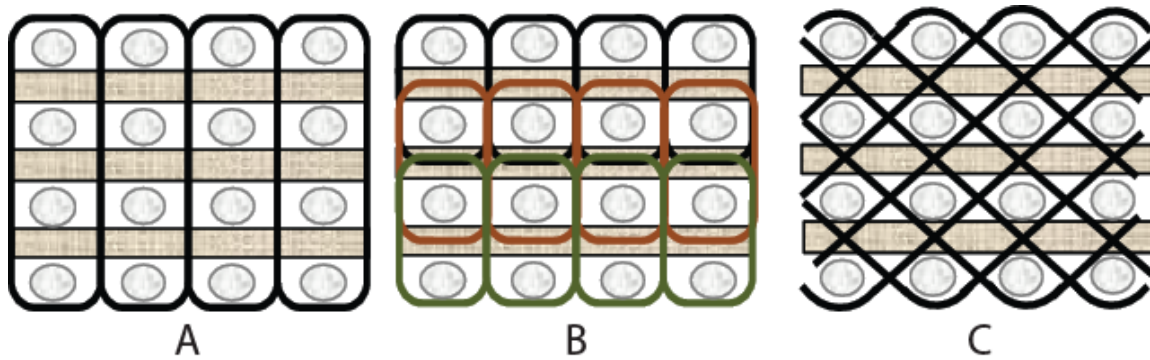


Figure 1-5. Schematics of 3D woven composites. A) 3D Orthogonal. B) Layer to layer interlock. C) Angle interlock. [Mahmood et al. 2011].

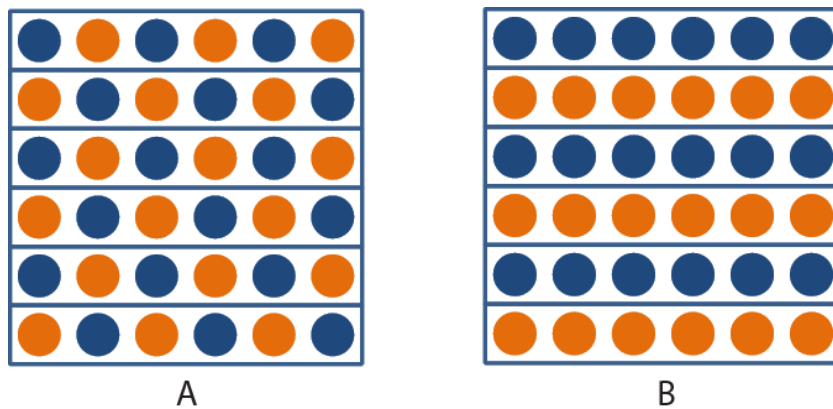


Figure 1-6. Hybrid composites. A) Intraply. B) Interply.



Figure 1-7. Schematic of bridging zone developed during delamination

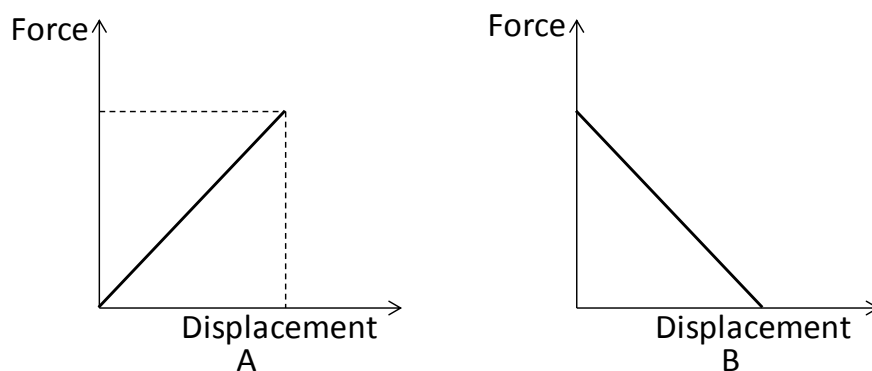


Figure 1-8. Bridging laws of TLR. A) Linearly increasing (stitching). B) Linearly decreasing (z-pinning).

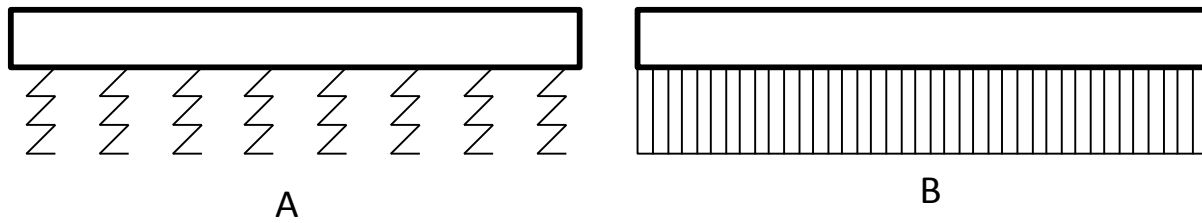


Figure 1-9. Spring model for bridging zone. A) discrete spring model. B) distributed traction model.

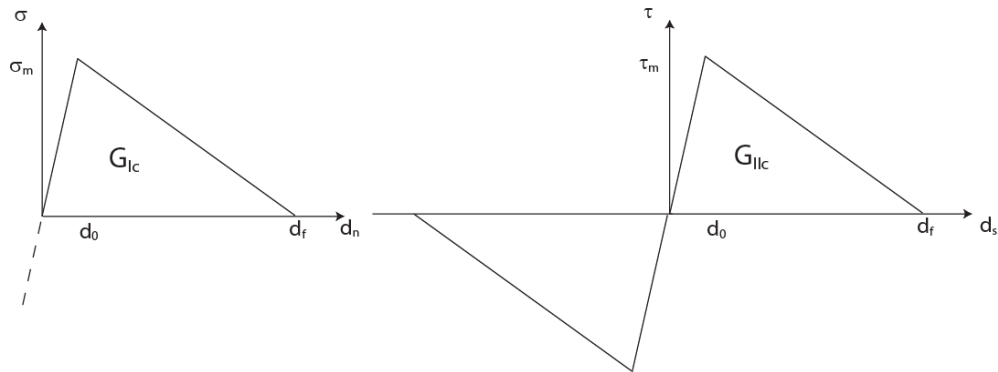


Figure 1-10. Traction- separation law for the cohesive element.

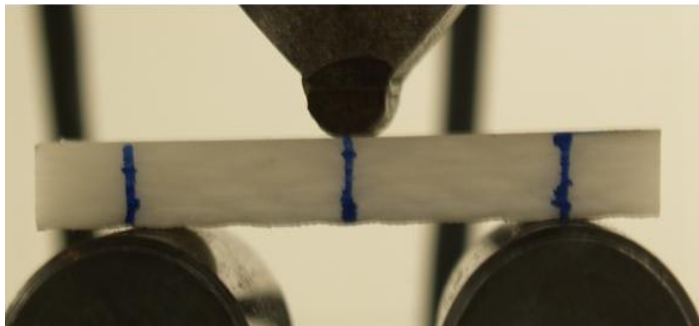


Figure 1-11. Quasi-static SBS test setup.

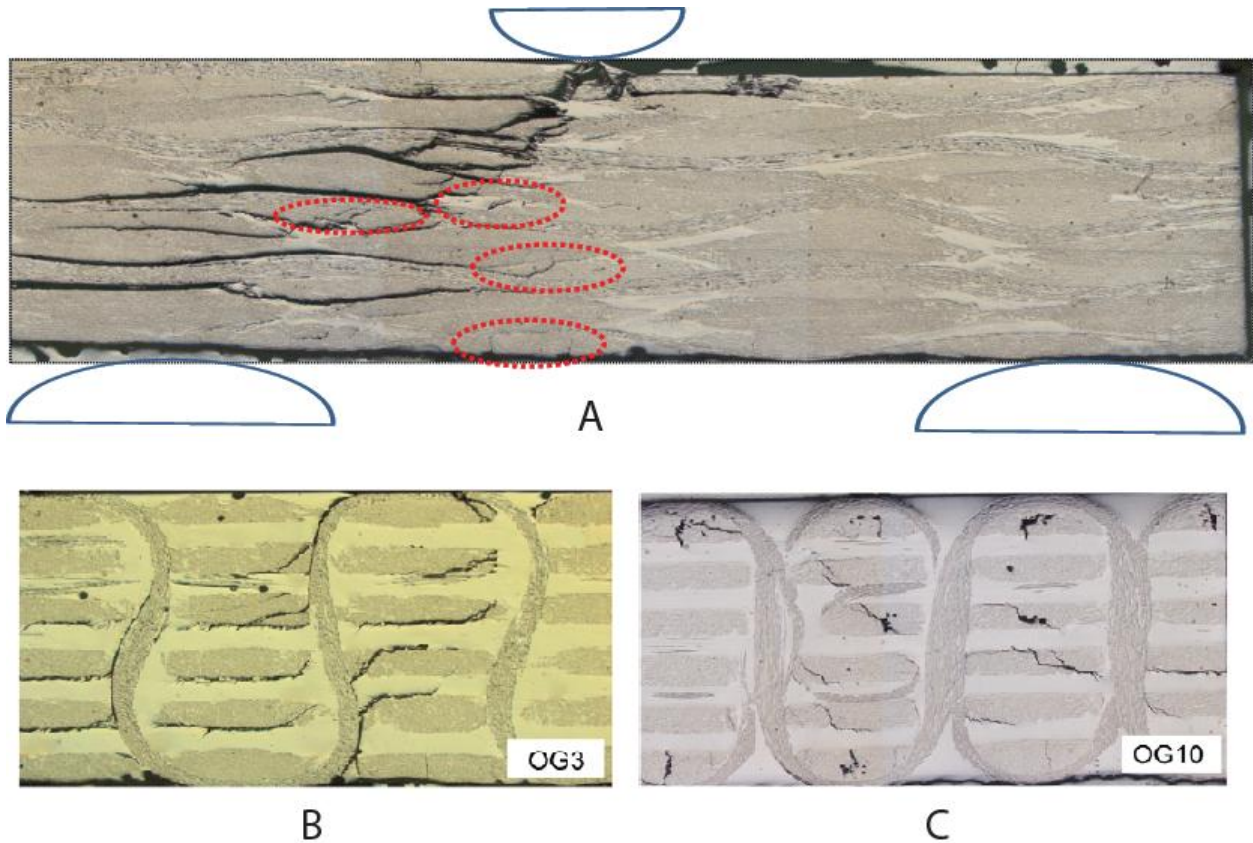


Figure 1-12. Damages after SBS test. A) In plain woven laminated composites. B) In 3D woven composites. [Walter et al. 2010].

Table 1-1. Summary of results obtained by various researchers and present study.

Reference	Z-pin in Analytic model	Z-pin model in FEM	Crack propagation criterion in FEM	Sub-laminate model in FEM	Comparison with experimental data
Cartie 2000	-	Bi-linear traction	J integral	Plane strain	Yes
Mabson and Deobald 2000	Distributed force (Non-dimensional form-1)	-	-	-	-
Byrd and Birman 2005	Distributed force (Dimensional form-1)	-	-	-	-
Robinson and Das 2004	Distributed force (Dimensional form-2)	-	-	-	Yes
Grassi and Zhang 2003	-	Nonlinear spring (Bi-linear function)	VCCT	Shell element	Yes
Ratcliffe and O'Brien 2004	Discrete force	-	-	-	Yes
Dantuluri et al. 2007	-	Nonlinear spring (Bi-linear function)	2D cohesive element	Beam element	Yes
Ratcliffe and Krueger 2006	-	Nonlinear spring (Bi-linear function)	3D cohesive element	Solid element	-
Present study	Distributed force (Non-dimensional Form-2)	Nonlinear spring (Linear softening unction and tri-linear bridging law)	3D cohesive element	Shell element	Yes



## CHAPTER 2

### ANALYSIS OF MODE I DELAMINATION OF Z-PINNED COMPOSITE USING A NON-DIMENSIONAL ANALYTICAL MODEL

Our goal here is to use both analytical and numerical approaches for studying the effect of z-pins and compare them with available experimental data. In particular, we have developed a non-dimensional model that will be useful in the design of translaminar reinforcements for a given application. In particular we have used a 3D shell model in conjunction with 3D cohesive elements. Both linear softening laws and more realistic tri-linear bridging laws are used to model the z-pins. In order to clarify the role of z-pins, a non-dimensional analytical model is proposed. The solution of the non-dimensional equation uses an iterative procedure. We have also derived an expression for the maximum density of z-pins that can be allowed before the beam fails otherwise. The efficacy of the analytical model is verified by finite element simulation of the DCB specimen. We have used the example given in [Cartie 2000] for this purpose. In the FE simulation, the ligaments of the DCB are modeled using shell elements. Cohesive elements are used to simulate the delamination and discrete nonlinear elements are used to model the z-pins. The agreement between the analytical model and FE simulations is found to be excellent for various results such as load-deflection, load-crack length and effective fracture toughness.

It was found that steady-state bridging length and maximum apparent fracture toughness can be related to interlaminar fracture toughness of the composite and maximum frictional force supported by z-pins. The relationships among various parameters are non-dimensionalized and the maximum pin friction that can be allowed before the composite beam itself fails is calculated. The non-dimensional analytical

model could be a useful design tool in selecting z-pins for composite structures to improve interlaminar fracture toughness.

### **Non-Dimensional Analytical Model**

Consider a z-pinned composite DCB specimen of thickness  $2h$  with initial crack length of  $a_0$  and subjected to Mode I loading as shown in Figure 2-1A. A pair of transverse forces  $F$  is applied at the tip of the DCB. Due to the applied transverse force  $F$  the initial crack tends to reach the current crack length denoted by  $a$  (Figure 2-1B). When the crack reaches the region reinforced by z-pins, a bridging zone of length  $c$  begins to develop (Figure 2-1C). We can define an apparent crack length  $a_p$  which is the length of the crack up to the beginning of the bridging zone. Current crack length ( $a$ ) is the sum of the apparent crack length ( $a_p$ ) and the bridging length ( $c$ ). When the z-pins start to be completely pulled out of the composite as shown in Figure 2-1D, the bridging zone becomes fully developed and a new fracture surface is created in the z-pinned zone. Therefore in the bridging zone the pull-out of pins is partial. Beyond the current crack tip the pins are assumed to be intact. The relative deflection at the tip of the DCB is denoted by  $\delta$  as shown in Figure 2-1E. Our goal is to determine the relationships among  $F$ ,  $a$ ,  $c$  and  $\delta$ . Once the bridging zone length  $c$  is determined other parameters such as  $F$ ,  $a$  and  $\delta$  can be found by solving the governing equations. In the following we describe the non-dimensional equation governing the bridging zone and procedures to determine the bridging length for a given load.

We assume that the shear deformation is negligible and use Euler-Bernoulli beam equations to model the ligaments of the DCB as shown in Figure 2-2B. We also assume that z-pins are rigid and there is sufficient friction between the z-pins and the composite



material surrounding it. For simplicity, the relation between the frictional force ( $f$ ) and pull out or slip distance ( $d_s$ ) is idealized as a linear softening function as shown in Figure 2-3. The validity of this assumption will be later verified in FE simulation. When the pins are intact they can exert a maximum friction force of  $f_m$ . As the pins pull out of the material, the loss of friction is proportional to the pullout distance  $d_s$ . When the pin is completely pulled out of the beam, the friction force reduces to zero. Thus the  $f$ - $d_s$  relationship is given by

$$f = f_m \left( 1 - \frac{d_s}{h} \right), 0 \leq d_s \leq h \quad (2-1)$$

where  $h$  is half the thickness of DCB.

Although the resistance offered by the pins on the beam is discrete, for the purpose of the analytical model we smear the discrete pin resistance as continuous distributed traction ( $p$ ) acting on the crack surfaces as shown in Figure 2-2C. Then the traction can be derived as

$$p = Nf = Nf_m \left( 1 - \frac{d_s}{h} \right) = p_m \left( 1 - \frac{d_s}{h} \right) \quad (2-2)$$

where  $N$  is z-pin density expressed as number of z-pins per unit area.

The Euler-Bernoulli beam equation for one of the ligaments, say upper ligament (Figure 2-2C), of the DCB can be written as:

$$EI \frac{d^4 w}{dx^4} = -bp \quad (2-3)$$

where  $b$  is the beam width. The effective bending rigidity of one of the ligaments of the DCB is represented by the term  $EI$ . Note that the flexural rigidity for a laminated

composite can be taken from the bending stiffness matrix in classical plate laminate theory. Substituting for  $p$  from Eq. (2-2) into Eq. (2-3), we obtain

$$EI \frac{d^4 w}{dx^4} - bp_m \frac{d_s}{h} = -bp_m \quad (2-4)$$

The pullout length  $d_s$  is equal to  $2w$ , where  $w$  is the deflection of the top or bottom beam. Hence, the governing equation takes the form

$$EI \frac{d^4 w}{dx^4} - 2p_m \frac{w}{h} = -bp_m \quad (2-5)$$

The origin of the x-coordinate is assumed to be the point at which the bridging zone begins. One should note that the origin moves as the crack propagates. The four boundary conditions (BCs) for the bridging zone are:

$$\begin{aligned} w(0) &= w_0, (0 < w_0 \leq h/2) \\ M_x(0) &= a_p V_z(0) \Rightarrow \frac{d^2 w}{dx^2}(0) = a_p \frac{d^3 w}{dx^3}(0) \\ w(c) &= 0 \\ \frac{dw}{dx}(c) &= 0 \end{aligned} \quad (2-6)$$

In the above equation  $w_0$  is a prescribed deflection at the origin of the coordinate system as shown in Figure 2-2C. This value will be less than  $h/2$  in the beginning and will increase to a maximum value of  $h/2$  as the DCB is loaded. Note that the slip distance of the z-pin is equal to the total opening of the DCB at that location, i.e.  $2w(x)=ds(x)$ . As the crack propagates, the bridging zone will also move with the crack, but the crack opening displacement will remain as  $h$  at the origin with  $2w(0)=ds(0)=h$ . The terms  $V$  and  $M$ , respectively, are the bending moment and transverse shear force on the beam cross section.

One should note that the bridging length  $c$  is still an unknown. It can be determined from the fact that the strain energy release rate at the actual crack tip should be equal to the Mode I fracture toughness at the instant of crack propagation. The energy release rate can be determined from the equation derived by Sankar and Sonik [Sankar and Sonik 1995] for beam-like specimens containing delamination.

$$G = \frac{(M(c))^2}{bEI} = \frac{EI}{b} \left( \frac{d^2 w(c)}{dx^2} \right)^2 \quad (2-7)$$

Thus the condition for determining  $c$  is

$$\frac{EI}{b} \left( \frac{d^2 w(c)}{dx^2} \right)^2 = G_{IC} \quad (2-8)$$

Before we solve the above equations we will non-dimensionalize the equations and BCs appropriately. Normalizing the length dimensions by  $h$  and forces by  $Eh^2$ , the governing equation and the BCs take the following form:

$$\frac{d^4 \tilde{w}}{d\tilde{x}^4} - 2\tilde{p}_m \tilde{w} = -\tilde{p}_m \quad (2-9)$$

$$\tilde{w}(0) = \tilde{w}_0, (0 < \tilde{w}_0 \leq 1/2)$$

$$\frac{d^2 \tilde{w}}{d\tilde{x}^2}(0) = \tilde{a}_p \frac{d^3 \tilde{w}}{d\tilde{x}^3}(0) \quad (2-10)$$

$$\tilde{w}(\tilde{c}) = 0$$

$$\frac{d\tilde{w}}{d\tilde{x}}(\tilde{c}) = 0$$

where  $\tilde{x} = \frac{x}{h}$ ,  $\tilde{a}_p = \frac{a_p}{h}$ ,  $\tilde{c} = \frac{c}{h}$ ,  $\tilde{w} = \frac{w}{h}$  and  $\tilde{p}_m = \frac{12p_m}{E}$

The equation for determining  $\tilde{c}$  (Eq. (2-8)) takes the form

$$\left( \frac{d^2 \tilde{w}(\tilde{c})}{d\tilde{x}^2} \right)^2 = \tilde{G}_{IC} \quad (2-11)$$

where the non-dimensional fracture toughness is given by  $\tilde{G}_{IC} = \frac{12G_{IC}}{Eh}$

The solution for the governing Eq. (2-9) is

$$\tilde{w}(\tilde{x}) = C_1 \cos \tilde{\lambda} \tilde{x} + C_2 \sin \tilde{\lambda} \tilde{x} + C_3 \cosh \tilde{\lambda} \tilde{x} + C_4 \sinh \tilde{\lambda} \tilde{x} + \frac{1}{2} \quad (2-12)$$

where  $\tilde{\lambda} = \sqrt[4]{2\tilde{p}_m}$

The boundary condition at the point  $\tilde{x} = 0$  varies since deflection at this point  $\tilde{w}_0$  increases from zero at the beginning of loading to 0.5 when the bridging zone is completely developed. Once the bridging zone is completely developed this value remains constant at 0.5 with additional increment of  $\tilde{a}_p$ . This is because the bridging zone is fully developed and it moves with the crack tip as it advances.

The procedures to solve the above set of equations are shown in the flow chart depicted in Figure 2-4. The initial data includes the beam properties, characteristics of the z-pins and the fracture toughness  $G_{IC}$ . The deflection at the beginning of the bridging zone ( $\tilde{x} = 0$ ) begins to increase as the load is applied.

When  $\tilde{w}(0) = 0.5$ , the bridging zone is fully developed and hereafter the deflection of the beginning of the bridging zone is constant. However, the apparent crack length increases during crack propagation. We need to use an iterative procedure as the bridging length ( $\tilde{c}$ ) is not known *a priori*. The strain energy release rate condition at the right end of the bridging zone ( $\tilde{x} = \tilde{c}$ ) as given by Eq. (2-11) is then used to check for correct value of  $\tilde{c}$ . When a given  $\tilde{c}$  satisfies Eq. (2-11), then the procedure to determine  $\tilde{c}$  is terminated. After bridging zone is fully developed, bridging length corresponding to every increment of crack length can be determined.

## Verification

### A Sample Problem for Verifying the Non-Dimensional Analytical Model

In order to verify the analytical model a z-pinned composites designed by Cartie [Cartie 2000] as shown in Figure 2-5 was selected. This z-pinned composite was also used in many previous works [Cartie 2000, Grassi et al. 2003]. The configurations and material properties are represented in Table 2-1. These values were used for both the analytical model and FE simulation presented in the next section.

First, the load-deflection curve (Figure 2-6) was found for  $a_p$  values ranging from 52.25 mm to 62.25 mm. Meanwhile the crack length as the summation of the apparent crack length ( $a_p$ ) and the bridging length ( $c$ ) obtained from the procedure depicted in Figure 2-4 was computed. The variation of the bridging length as a function of DCB deflection  $\delta$  is shown in Figure 2-7. The bridging length initially increases with loading until the bridging zone is fully developed, where the bridging length has the maximum value. In the beginning, the apparent crack length remains constant and the crack propagation is only due to evolution of the bridging zone. Once the bridging zone is fully developed there is little change in the bridging length thus the crack propagation is almost due to the apparent crack length. In fact there is a slight decrease in the bridging length after it reaches the maximum as the bending moment due to the transverse loads applied is a function of the apparent crack length. If a pair of couples is applied instead of a pair of forces as in the standard DCB test, then the bending moment will remain constant as the crack propagates, and one can see a steady state bridging length.

The force  $F$  acting on the DCB and opening displacement  $\delta$  at the end of the beam can be obtained using the following relations:

$$F = -EI \left. \frac{d^3 w}{dx^3} \right|_{x=0} \quad (2-13)$$

$$\delta = 2 \left( w(0) + a_p \left. \frac{dw}{dx} \right|_{x=0} + \frac{1}{3} \left. \frac{d^3 w}{dx^3} \right|_{x=0} a_p^3 \right) \quad (2-14)$$

The variations of transverse force and crack length with increments in opening displacement are shown in Figure 2-6. Initially the transverse force increases with opening displacement and begins to drop as interlaminar crack in unreinforced region propagates. However, the transverse force increases during the development of the bridging zone and decreases again with the movement of the fully developed bridging zone and the new crack surface.

In order to estimate the apparent fracture toughness during crack propagation we use the bending moment at the apparent crack tip as a measure of increased fracture toughness. This is similar to calculating the fracture toughness of the unreinforced beam using Eq. (2-7). Then the apparent fracture toughness is defined as

$$G_{IC-app} = \frac{EI}{b} \left( \frac{d^2 w(0)}{dx^2} \right)^2 \quad (2-15)$$

The above relation can be non-dimensionalized as :

$$\tilde{G}_{IC-app} = \left( \frac{d^2 \tilde{w}(0)}{d\tilde{x}^2} \right)^2 \quad (2-16)$$

The variation of apparent fracture toughness during crack propagation is shown in Figure 2-8. The apparent fracture toughness increases during development of the bridging length since the bending moment required at the beginning of bridging zone to overcome the bridging force increases gradually.

Maximum attainable apparent fracture toughness can be predicted by the relationship expressed in terms of interlaminar fracture toughness and bridging force due to z-pins. The relationship is exactly the same as the equation based on energy balance. As the crack propagates it has to overcome the frictional forces in the z-pins. The amount of extra work done is equal to the area under the load-deflection diagram in Figure 2-3. Thus the maximum apparent fracture toughness can be derived as:

$$G_{IC-app-max} = G_{Ic} + N \left( \frac{1}{2} f_m h \right) \quad (2-17)$$

Multiplying throughout by  $(12/Eh)$  we obtain the above relation in a non-dimensional form as:

$$\tilde{G}_{IC-app-max} = \tilde{G}_{Ic} + \frac{1}{2} \tilde{p}_m \quad (2-18)$$

This maximum value can be realized when a pair of couples is applied instead of a pair of transverse forces. As shown in Figure 2-8, the apparent fracture toughness for transverse loading is always less than the maximum value. Furthermore, our definition of apparent fracture toughness in Eq. (2-16) is also slightly different from the energy based relation given in Eq. (2-18) making the apparent fracture toughness under transverse loading less than the maximum realizable value. This is useful in evaluating the increase in apparent fracture toughness for a given design of z-pins. Moreover this value is related to strain exerted in the ligaments of DCB and will be discussed later.

### **A FE Simulation for Verifying the Non-Dimensional Analytical Model**

For the sake of comparison with the analytical model, FE simulation of the same specimen using the finite element software, ABAQUS<sup>®</sup>, was performed. The FE model containing discrete z-pins can verify the analytical model where z-pins are smeared and

represented by distributed traction. The three-dimensional FE analysis was used to simulate crack propagation in the DCB specimen with z-pins. The specimen was modeled using shell elements (S4), and cohesive elements (COH3D8) were used to simulate progressive delamination.

The behavior of cohesive elements can be characterized by a bi-linear traction separation law (Figure 2-9) [Davila et al. 2007] given by

$$\sigma = (1 - D)Kd$$

where

$$D = \begin{cases} 0 & , d < d_0 \\ \frac{d_f (d - d_0)}{d (d_f - d_0)} & , d_0 < d < d_f \\ 1 & , d_f < d \end{cases} \quad (2-19)$$

where  $\sigma$  is traction,  $K$  is stiffness,  $D$  is damage variable,  $d$  is displacement,  $d_0$  is displacement at damage initiation and  $d_f$  is final displacement.

The above parameters were taken as:  $K=10^6$  N/mm,  $\sigma_m=35$ Mpa and  $G_{IC}=0.258$  N/mm [Cartie 2000, Davila et al. 2007].

The nonlinear spring element (CONN3D2), whose behavior is defined by a linearly decreasing force (Figure 2-3) for each z-pin, was also implemented between the two ligaments of the DCB (Figure 2-10).

The load-deflection curves and the variations of crack lengths with deflection are shown in Figure 2-6. Both the FE and analytical model results are presented with that from the experiment by Cartie [Cartie 2000]. The agreement between the analytical model and the FE simulations is satisfactory for both load-deflection and delamination length. The slight discrepancy in the initial slope of the load-deflection curve between



the analytical model and the FE model is due to the fact that the analytical model uses Euler-Bernoulli beam theory whereas the FE model considered shear deformation as it occurs in test specimens. The good comparison between the analytical model and the results from FEA and experiments suggests that the discrete bridging force can be represented by a distributed traction.

## **Discussion of Results from the Non-Dimensional Model**

### **Parametric Studies using the Non-Dimensional Analytical Model**

Our goal was to study the effects of inherent interlaminar fracture toughness of the composite material  $\tilde{G}_{Ic}$  and the non-dimensional frictional force  $\tilde{P}_m$  on (i) the maximum apparent fracture toughness  $\tilde{G}_{Ic-app-max}$  and (ii) steady state bridging length  $\tilde{c}$ . Such relationships are extremely useful in the design process to evaluate the influence of design variables on performance of the composite. In this parametric study we assume that the DCB is loaded by end couples instead of transverse forces. This assures steady state crack propagation in the beam and the effect of increasing crack length on the results is thus eliminated. In the simulations,  $\tilde{G}_{Ic}$  is varied from  $10^{-7}$  to  $10^{-4}$  and  $\tilde{P}_m$  ranged from  $10^{-10}$  (almost zero friction representing the case of an unreinforced beam) to 0.1.

Figure 2-11 shows that the steady state bridging length decreases with increasing  $\tilde{G}_{Ic}$  and  $\tilde{P}_m$ . If the composite material is inherently tough, it will not allow a larger bridging length. Similarly a large friction force also will reduce the bridging length. The maximum apparent fracture toughness ( $\tilde{G}_{Ic-app-max}$ ) is another measure to evaluate the effect of translaminar reinforcement. Figure 2-12 shows that the maximum apparent

fracture toughness, computed by Eq. (2-16), varies linearly with increasing  $\tilde{G}_{lc}$  and  $\tilde{P}_m$ .

This result is in accordance with Eq. (2-18). Since the range of  $\tilde{P}_m$  is wider than that of  $\tilde{G}_{lc}$  in reality,  $\tilde{G}_{lc-app-max}$  is more sensitive to the value of  $\tilde{P}_m$ . In other words the apparent fracture toughness is dominated by translaminar reinforcement. From the results shown in Figures 2-11 and 2-12, it is clear that higher friction force exerted by the z-pins provides enhanced fracture toughness and at the same time reduces the bridging length. The latter is important to maintain the stiffness of the structure for a larger bridging length leads to reduction in the stiffness of the structure.

### Maximum Allowable Translaminar Reinforcement

Even though large frictional force between the z-pin and the surrounding matrix material is desirable for increased fracture toughness, a frictional force beyond a critical value will cause the beam to fail. The maximum normal strain in a beam cross section is given by

$$\epsilon_{\max} = \frac{h}{2} \left| \frac{d^2 w}{dx^2} \right| \quad (2-20)$$

Note the strain is already non-dimensional and the right hand side of the above equation can be written as

$$\epsilon_{\max} = \frac{1}{2} \left| \frac{d^2 \tilde{w}}{d\tilde{x}^2} \right| = \frac{\tilde{\kappa}}{2} \quad (2-21)$$

where  $\tilde{\kappa}$  is the non-dimensional curvature which has the maximum value at  $\tilde{x} = 0$ . Using Eqs. (2-16) and (2-18) we obtain

$$\tilde{\kappa} = \sqrt{\tilde{G}_{lc} + \frac{1}{2} \tilde{P}_m} \quad (2-22)$$

Let us assume the allowable strain in the composite is given by  $\varepsilon_u$

Then

$$\sqrt{\tilde{G}_{lc} + \frac{1}{2}\tilde{p}_m} < 2\varepsilon_u \quad (2-23)$$

From the above equation one can derive

$$\begin{aligned} \tilde{p}_m &< 2(4\varepsilon_u^2 - \tilde{G}_{lc}) \\ \text{or} \\ p_m = Nf_m &< \frac{2}{3}E\varepsilon_u^2 - \frac{2G_{lc}}{h} \end{aligned} \quad (2-24)$$

The above equation provides an upper limit on the z-pin density which should be taken into consideration in the design of translaminar reinforcements. Thus the allowable density or maximum frictional force of z-pins can be determined at a given geometry and material properties of a composite material.

In order to verify the result for the maximum allowable translaminar reinforcement given in Eq. (2-24), we performed finite element analysis of a specimen. The properties used were:  $G_{lc} = 0.258 \text{ N/mm}$ ,  $h = 1.6 \text{ mm}$ ,  $E = 138 \text{ GPa}$ ,  $Nf_m = 1.58 \text{ N/mm}^2$  [Cartie 2000].

The FE simulation was used to calculate the maximum strain in the ligaments of the DCB specimen at the instant of crack propagation, and it was compared with the  $\varepsilon_u$  obtained from Eq.(2-24). Two loading cases, namely end couples and transverse forces, were considered. For the set of properties used Eq.(2-24) yields a maximum strain  $\varepsilon_u = 4.5 \times 10^{-3}$ . Note that if  $Nf_m > 1.58 \text{ N/mm}^2$  then the maximum strain exceeds the ultimate strain. From the FE simulations we obtained  $\varepsilon_{\max} = 4.521 \times 10^{-3}$  for the case of end couples and  $\varepsilon_{\max} = 3.906 \times 10^{-3}$  for the case of transverse loading of the DCB (Figure

2-13). The results indicate the strains in the beam are higher for the moment loading compared to that due to the transverse loading. However, in a practical structure the delamination will experience a combination of shear and moment loadings, and hence the conservative value should be used. That means the maximum allowable stitch density given in Eq. (2-24) should be used although it is applicable only to moment loading case, and hence conservative.

### **Effect of Tri-Linear Bridging Law**

So far we have used the linear softening bridging law for developing the non-dimensional analytical model and verifying the same using FEA. Although this bridging law is simple, it may not be realistic. Dai et al. [Dai et al. 2004] performed pull-out tests using z-pins of various diameters to determine the actual bridging law. They found that a high value of debonding force was reached before the debonding of the pins began. After the debonding was initiated, the pull-out force dropped to a lower value before reducing linearly to zero value as the pins were pulled out steadily against frictional force that seemed to have a constant coefficient of friction. They represented this pullout behavior by a tri-linear bridging law as depicted in Figure 2-14. The tri-linear behavior can be attributed to an elastic deformation (from (0, 0) to (0.0185, 35.3) in Figure 2-14), debonding from surrounding matrix (from (0.0185, 35.3) to (0.17, 14.86) in Figure 2-14) and slip-out of z-pins (from (0.17, 14.86) to (1.6, 0) in Figure 2-14).

The finite element simulations of the DCB described above were repeated with the tri-linear bridging law. We did not attempt analytical solution as it will be very complicated due to the piecewise continuous bridging law. The numerical values for the tri-linear law were chosen such that the area under the force-displacement curve, which

is related to the increase in fracture toughness, is equal to the linear softening law used in the earlier example.

The areas under the two force-displacement curves in Figure 2-14 are equal to each other. The resulting load-deflection diagram of the z-pinned DCB specimen is shown in Figure 2-15. The load deflection behavior is almost identical to that obtained using the linear bridging law indicating that the apparent fracture toughness is same in both cases. It must be noted that the peak force in the tri-linear case is almost twice as that of the linear softening law. The variations of crack length as a function of the DCB specimen opening (deflection) are also similar in both cases. This indicates that the details of the bridging law do not seem to affect the global behavior of the specimen as long as the energy dissipated by the pins is properly accounted for.

### **Summary and Conclusions**

Mode I delamination propagation in DCB specimens containing z-pins is studied. A simple analytical model based on a linear softening type bridging law for the z-pins has been developed and suitable non-dimensional parameters have been identified. The load-deflection curve of the DCB specimen was calculated using the analytical model. It is seen that the bridging zone, wherein the pins are partially pulled out, develops as the crack propagates, but attains a steady state value. The length of the bridging zone is a function of the Mode I fracture toughness and the frictional force between the z-pins and the surrounding material. An expression was derived for the apparent or effective fracture toughness values. Although increase in frictional force as the z-pins increases the fracture toughness, there is an upper limit to this friction as the DCB ligaments would break if the friction is very high. The limiting value of the pin friction is derived.

The efficacy of the analytical model was evaluated by the simulation of the DCB specimen using finite element simulations. In the FE model the delamination propagation was simulated by cohesive elements and the z-pins were modeled as discrete nonlinear elements. The results for the load-deflection curve and the crack bridging zone length agreed quite well with the analytical model. As an alternative to the linear bridging law, a more realistic tri-linear bridging law was used in the FE simulations. It is found that the global delamination behavior of the specimen was not affected much as long as the energy dissipated by the pins is kept the same.

The non-dimensional model with few parameters will serve as a design tool when translaminar reinforcements such as z-pins are selected for laminated composite structures in order to improve their fracture toughness. The analytical models will also be useful in optimization studies and simulation of large composite structures containing translaminar reinforcements.

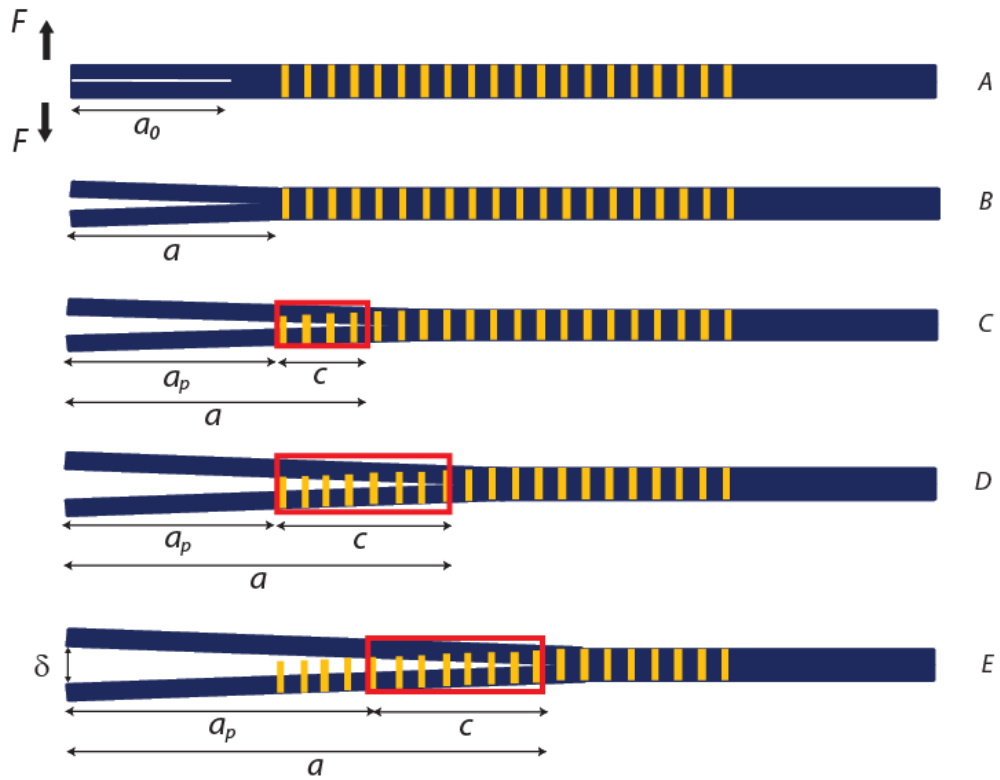


Figure 2-1. Schematic of initial geometry and development of bridging zone by z-pins in the composite DCB.

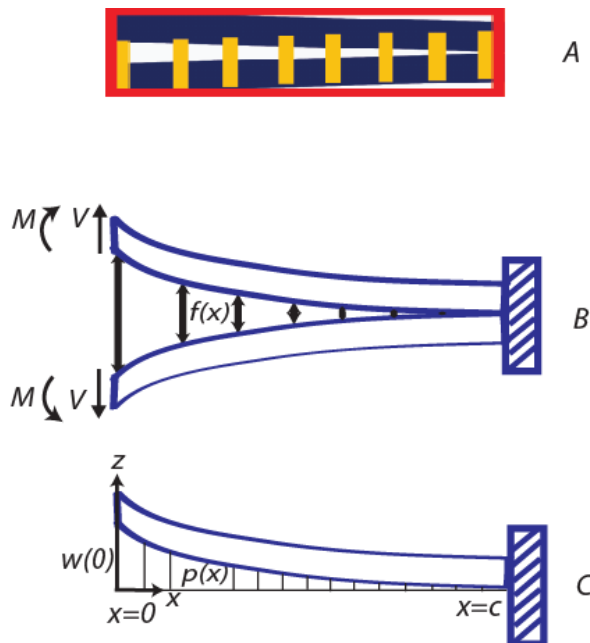


Figure 2-2. Idealization of bridging zone using a beam model.

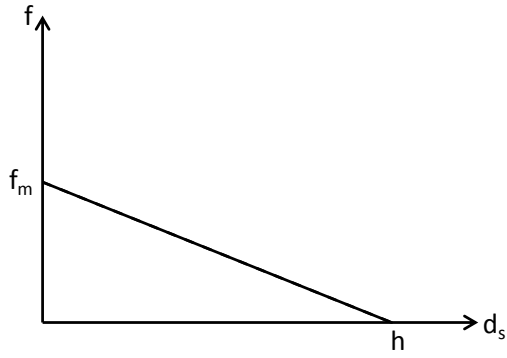


Figure 2-3. Force-displacement relation of the z-pin.

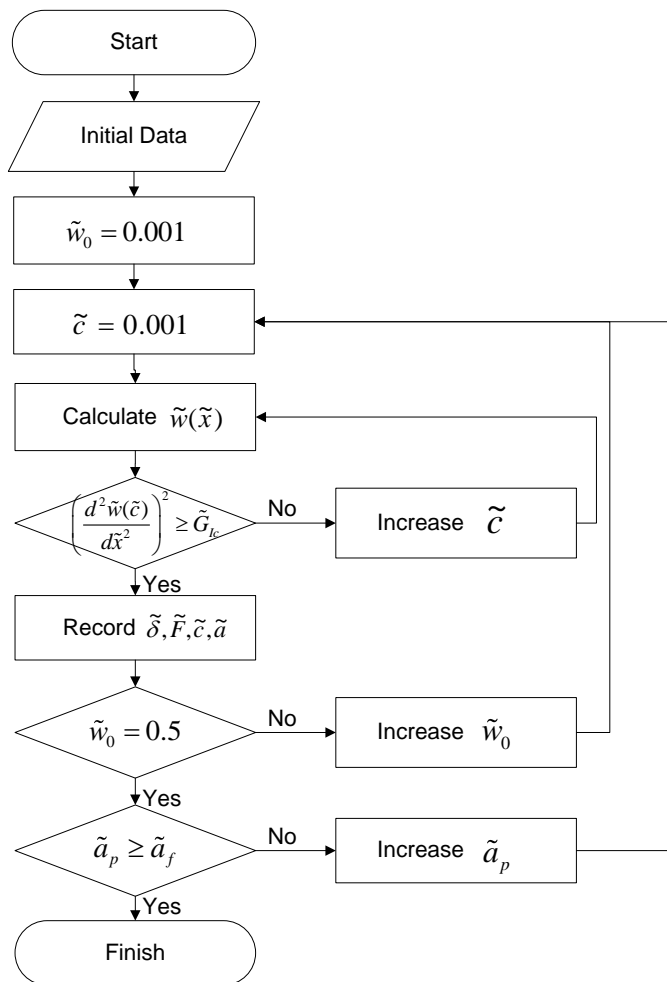


Figure 2-4. Flowchart of the procedures for solving the non-dimensional governing equation.



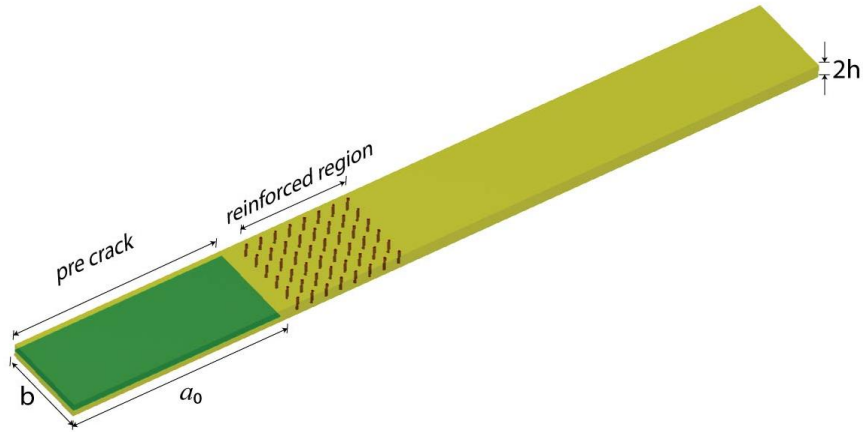


Figure 2-5. DCB specimen reinforced by z-pins [Cartie 2000].

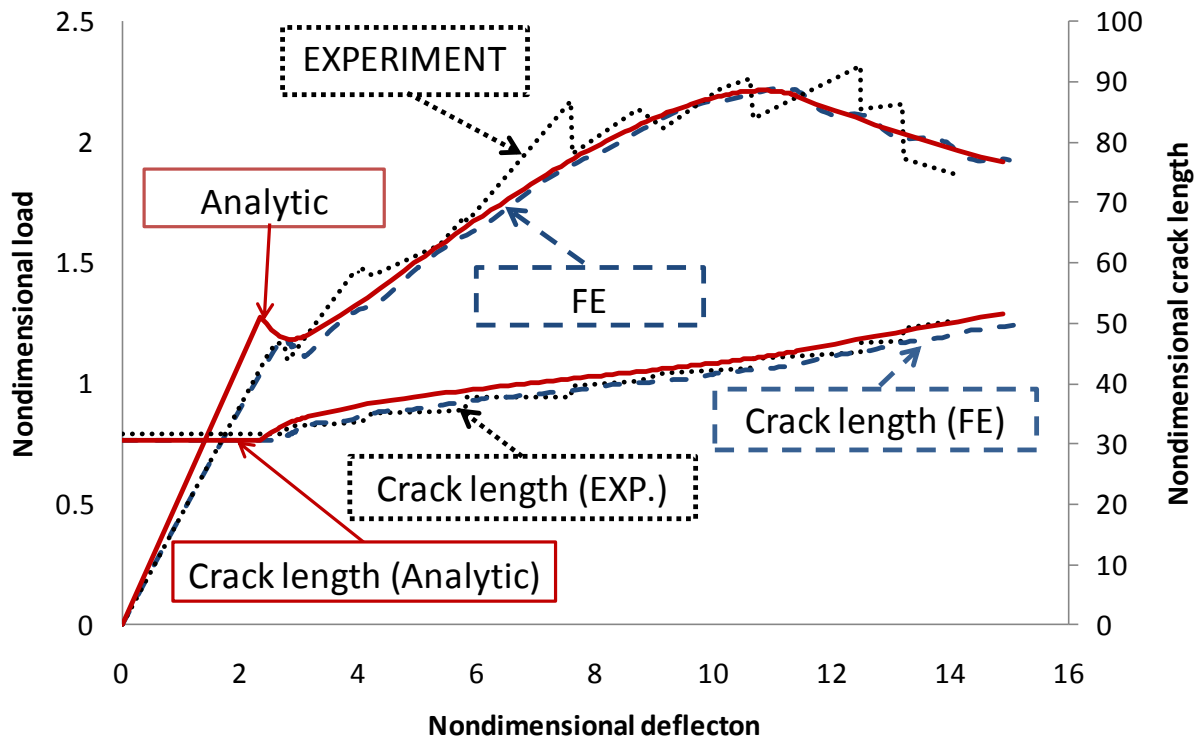


Figure 2-6. Load and crack length variation as a function of DCB deflection.

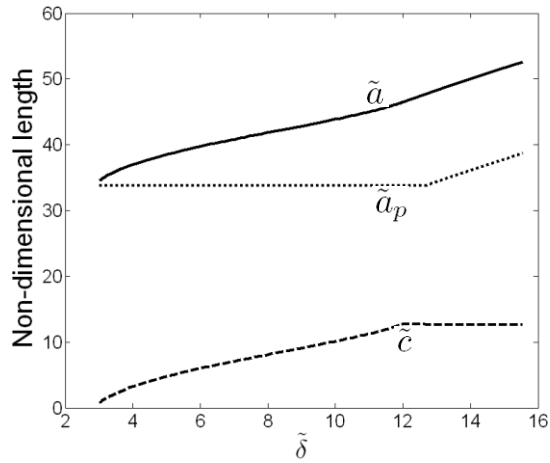


Figure 2-7. Bridging length and crack length as a function of DCB deflection.

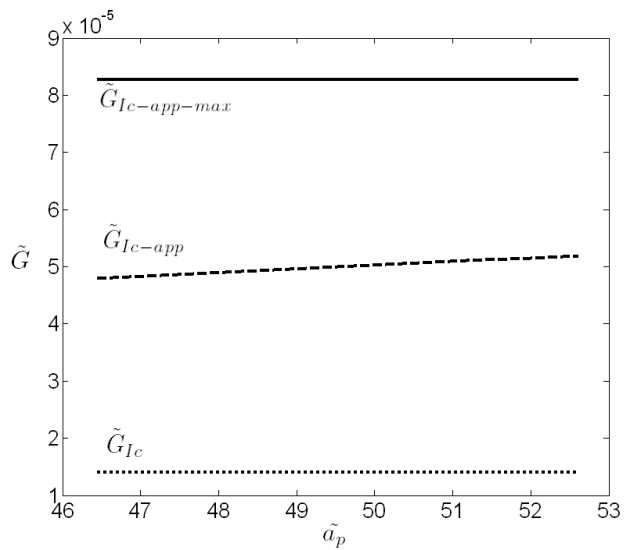


Figure 2-8. Variation of apparent fracture toughness during crack propagation.

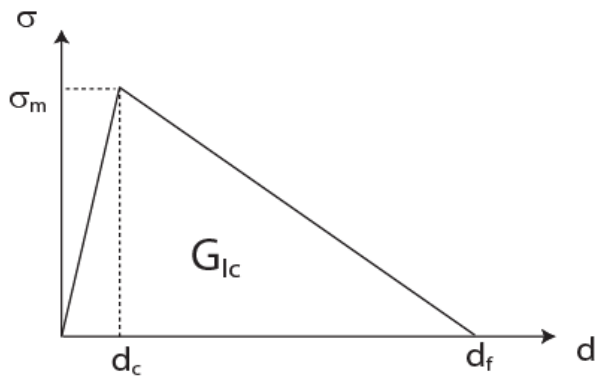


Figure 2-9. Traction- separation law for the cohesive element.

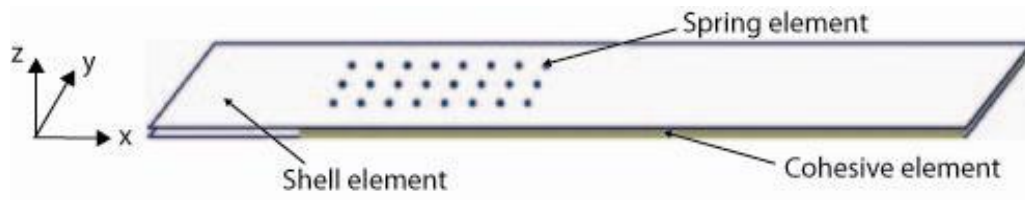


Figure 2-10. Cohesive and spring elements in the FE model of the DCB.

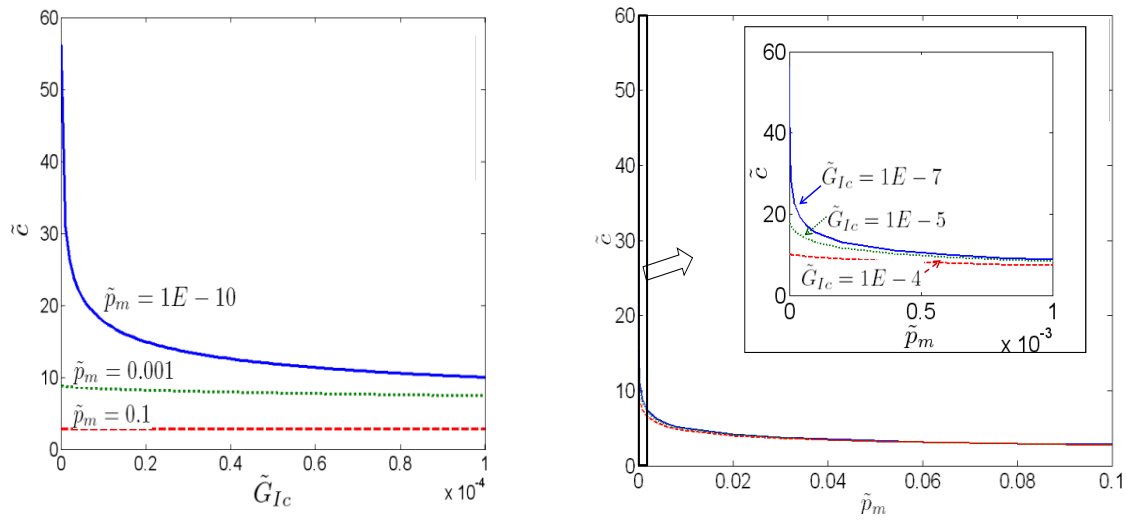


Figure 2-11. Non-dimensional steady state bridging length.

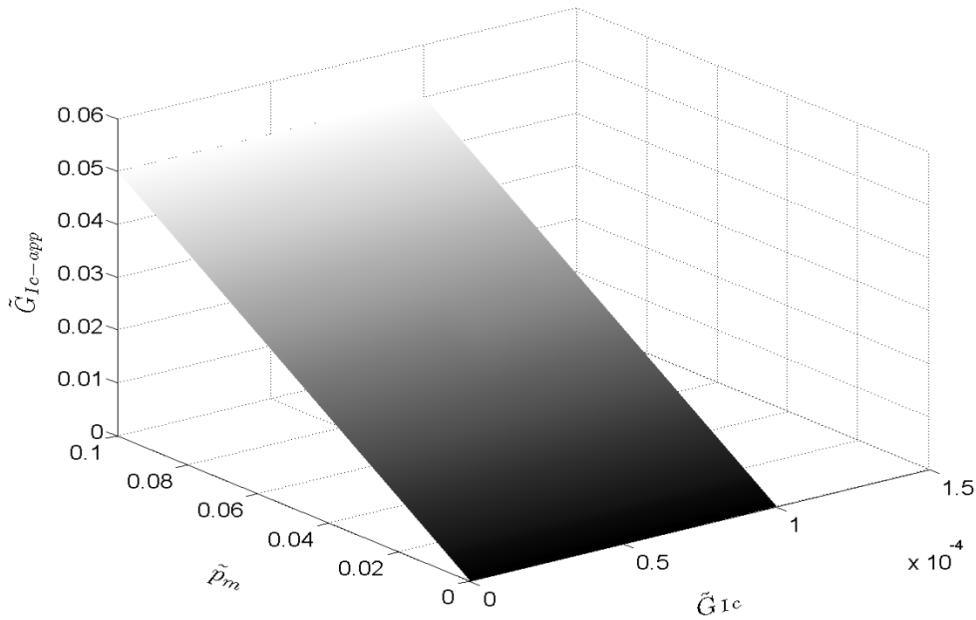
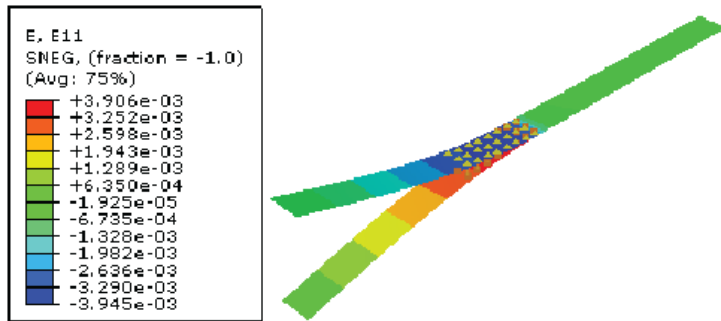
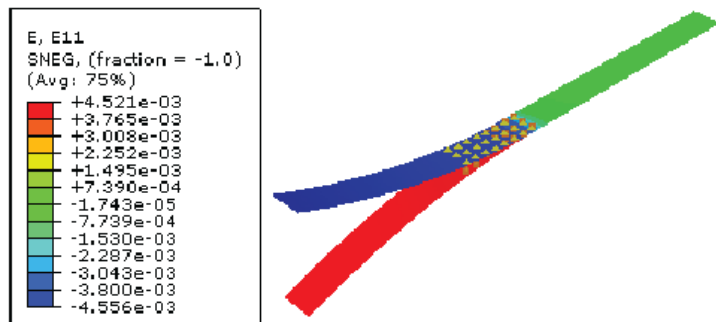


Figure 2-12. Apparent fracture toughness as a function of maximum friction force and interlaminar fracture toughness.



A) Force Input



B) Moment Input

Figure 2-13. Comparison of strain with different loading types.

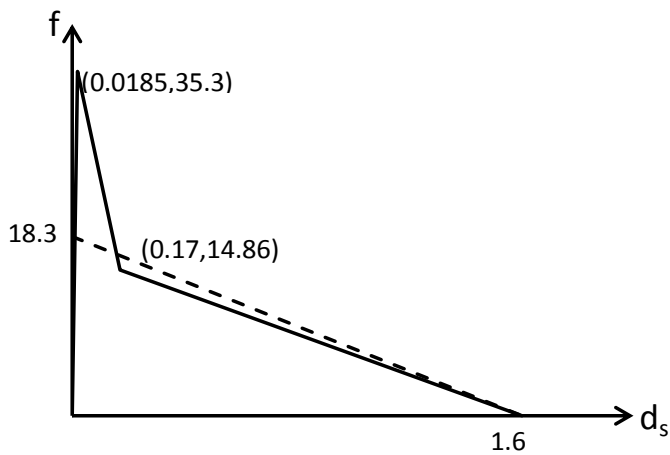


Figure 2-14. The tri-linear bridging law is indicated by the solid line. The dotted line is the linear softening law in Figure 2-3. The areas under the force-displacement diagram for both laws are the same.

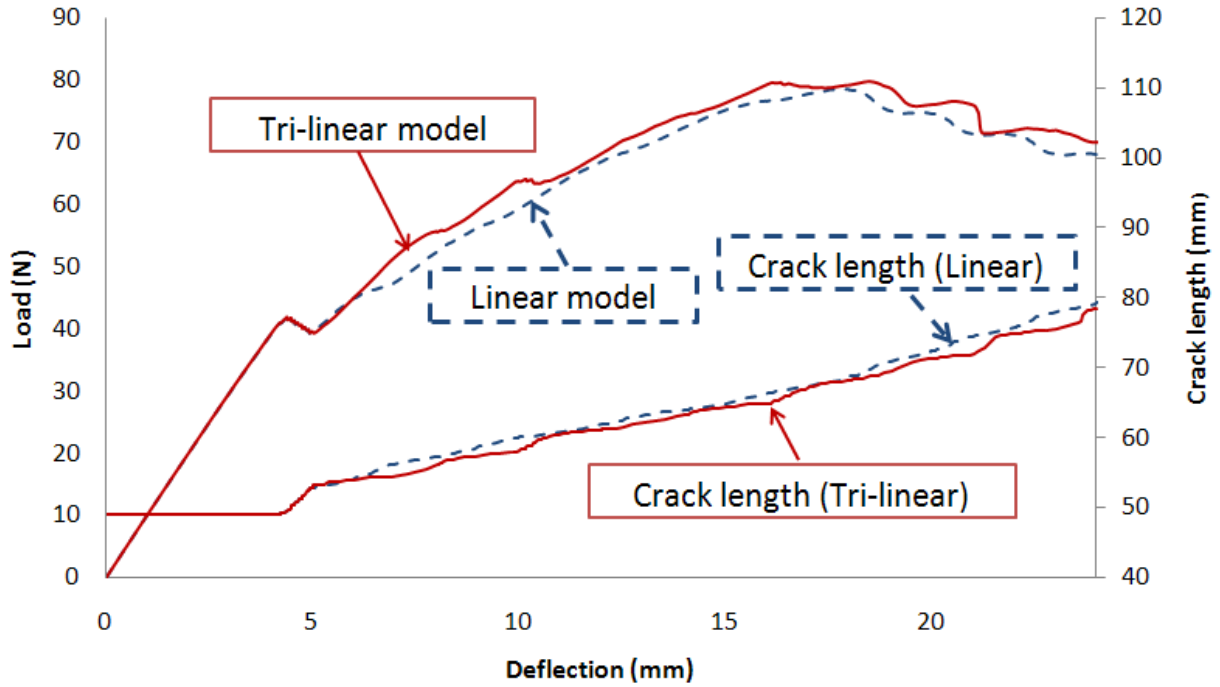


Figure 2-15. Load-deflection curve from various bridging laws.

Table 2-1. The various dimensions and properties of the DCB used in the numerical simulation [Cartie 2000]

Dimension or Property	Value
$B$	20 mm
$H$	1.6 mm
$E_1$	138 Gpa
$E_2$	11 GPa
$\nu_{12}$	0.34
$G_{12}$	4.4 GPa
$G_{Ic}$	258 N/m
$a_0$	49 mm
$F_m$	18.43 N
z-pin density	0.5 %
z-pin diameter	0.28 mm

### CHAPTER 3

#### APPLICABILITY OF QUASI-STATIC ANALYSIS FOR LOW VELOCITY IMPACT

Short Beam Shear (SBS) tests are widely used to characterize and quantify impact resistance of the composites with various constituent materials and fiber architectures for both quasi-static and dynamic loading. THE SBS test is basically a three-point bend test with a much shorter span length. The ratio of length to height of the specimen ( $L/h$  ratio) is typically less than 10. The test designated as ASTM D2344 was originally designed for measuring interlaminar shear strength of laminated composites. Since it closely mimics low-velocity impact response and damage, it has been used to measure impact resistance and impact damage tolerance of composite materials. The interlaminar shear strength (ILSS) is calculated from the maximum force  $P_{max}$  before failure initiates in the specimen.

The interlaminar shear strength is calculated as

$$ILSS = \frac{3}{4} \frac{P_{max}}{bh} \quad (3-1)$$

The above equation is based on parabolic variation of transverse shear stress through the thickness of the beam. It is true only for homogeneous materials and also the cross section should be away from the loading region. The above equation which is based on static loading is also being used for understanding impact damage. It assumes that the specimen is in quasi-static equilibrium, and neglects any dynamic effects. However, the above assumption would be valid only below certain impact velocity. Hence, we perform finite element simulations of dynamic loading cases and calculate the detailed stress

field and compare the results with corresponding static solution in order to verify the validity of quasi-static assumption for impact loading situations.

### **Finite Element Analyses**

Equation (3-1) used in this study in conjunction with the measured impact force for estimating ILSS implicitly assumes that the specimen is in quasi-static equilibrium neglecting any dynamic effects. In order to verify this assumption Finite Element Analysis (FEA) of the impact test was performed. The analysis was simplified by utilizing the symmetry of the specimen and therefore only one half of the SBS specimen was modeled as shown in Figure 3-2.

In addition, the specimen was homogenized as an orthotropic elastic material with properties given in Table 3-1 [Xiao et al. 2007]. The use of fully elastic model removes any material rate dependency and focuses the study on the effect of inertia and wave mechanics. The FEA study included three rates of dynamic impact as well as quasi-static loading to determine how loading rate affects the outcome of the analysis.

The commercial FE software codes, Abaqus Standard® and Abaqus Explicit® were used for the quasi-static and dynamic loading, respectively. The specimen was modeled using four-node plane strain elements with reduced integration (CPE4R) and a thickness set at 20 mm. Approximately 32,000 elements were used for both static and dynamic cases. The indenter and the support were modeled as rigid bodies.

Dynamic loading was simulated using three different impact velocities, 11, 22 and 33 m/s. The maximum impact velocity in the experiments corresponds to the lowest rate, 11 m/s.

The velocity profiles for the three impact simulations are depicted in Figure 3-3. The shape of the profiles was chosen such that they closely resemble the

experimentally measured profile discussed below. The duration of each profile was modeled to result in a final displacement of 2.5 mm. This displacement, which can be determined from the area under the  $v-t$  diagram, is consistent with experimental results [Walter et al. 2012]. Both the impact force (reaction force on the indenter) and the support reaction were calculated for each time increment. In the FEA the displacement of the rigid indenter was controlled by the velocity profile up to 2.5 mm under the displacement control. The time step for explicit analysis was calculated automatically by the FE program and it was in the order of  $10^{-8}$  seconds.

## **Results**

The impact force was determined from the reaction on the indenter. The impact force–displacement curves for various impact velocities are shown in Figure 3-4. The deviation of the dynamic loading curves from the quasi-static results indicates the effects of inertia on the load-displacement relation. From these curves it was observed that up to 22 m/s, the effect of inertia on the results may be neglected. At 33 m/s this effect becomes much more significant reducing the accuracy of the results. It is clear from these curves that inertia limits the loading rates to approximately 22 m/s.

Next the reaction force determined at the support is compared with the impact force at the indenter to verify quasi-static equilibrium. The results for the each of the dynamic loading simulations are shown in Figure 3-5 (note that the results for quasi static loading were not analyzed as it is in static-equilibrium).

If the specimen is in equilibrium the reaction forces at the indenter and the total force at the supports should be equal. From Figure 3-5A it can be noted that equilibrium is satisfied during impact at a velocity of 11 m/s. At 22 m/s impact velocity (Figure 3-5B), the two forces varied at the beginning of impact event however after approximately 0.5



mm of deflection, equilibrium is reached. It is observed from Figure 3-5C that equilibrium is never fully satisfied when loaded at a rate of 33 m/s.

Next the through thickness transverse shear stress profile was examined for the quasi-static, 11 m/s and 22 m/s results. Since the results from 33 m/s impact were previously shown to be invalid, due to a state of non-equilibrium, it was not analyzed for stresses. These profiles were determined at a plane midway between the support and indenter (as shown in Figure 3-2). The purpose of this comparison is to evaluate the effect of loading rate on the response of the sample and compare the FEA profiles with theoretical profiles. The profiles were determined at a displacement of 1.5 mm and are presented in Figure 3-6.

The theoretical profiles are determined using the indenter force and classical mechanics result for transverse shear stresses  $\tau = \frac{(P/2)Q}{Ih}$ , where  $P/2$  is the shear force,  $Q$  is first moment of area,  $I$  is moment of inertia and  $h$  is the thickness,) which is the basis for Eq. (3-1). The FEA profiles are shown as solid lines while theoretical profiles are shown as dashed lines. It is apparent from Figure 3-6A that there is only a slight deviation between quasi-static and dynamic shear stress profiles. This deviation is shown much more clearly in an enlarged view in Figure 3-6B. The theoretical results over-predict the FEA shear stress (about 8% for quasi-static and 11m/s impact velocity case, and 11% for 22m/s impact velocity case). The shear stress results for quasi-static and 11 m/s impact velocity cases were quite similar; but the results for 22 m/s were about 3% higher than the quasi-static results. As mentioned previously the actual shear stress is often much different than what is predicted using equation (1) and therefore is often used to compare different architectures. These results show that it is possible to

compare results from static tests as well as dynamic tests at rates up to 11 m/s with little deviation and rates of 22 m/s with moderate error.

From the above discussion it is clear that at an, or below, impact velocity of 11 m/s the specimen may be considered to be in equilibrium, and the use of equation (3-1) for estimating the ILSS of the material could be considered valid.

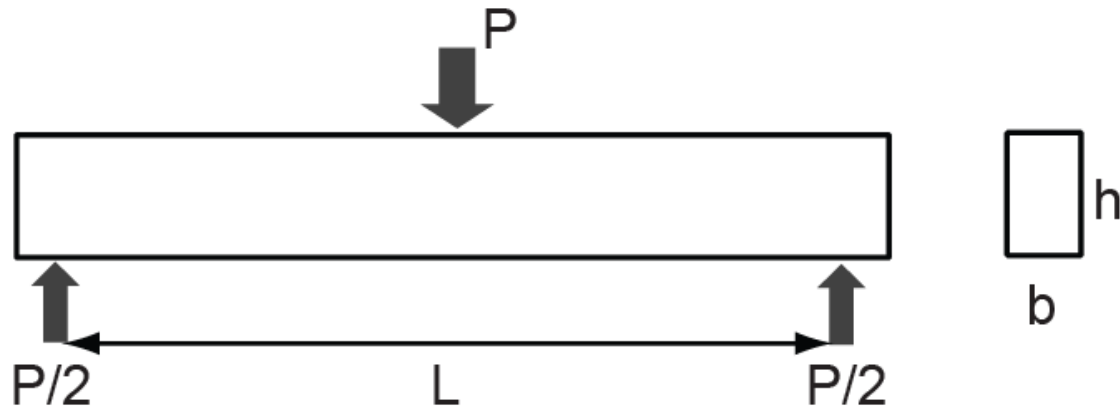


Figure 3-1. Short beam shear test.

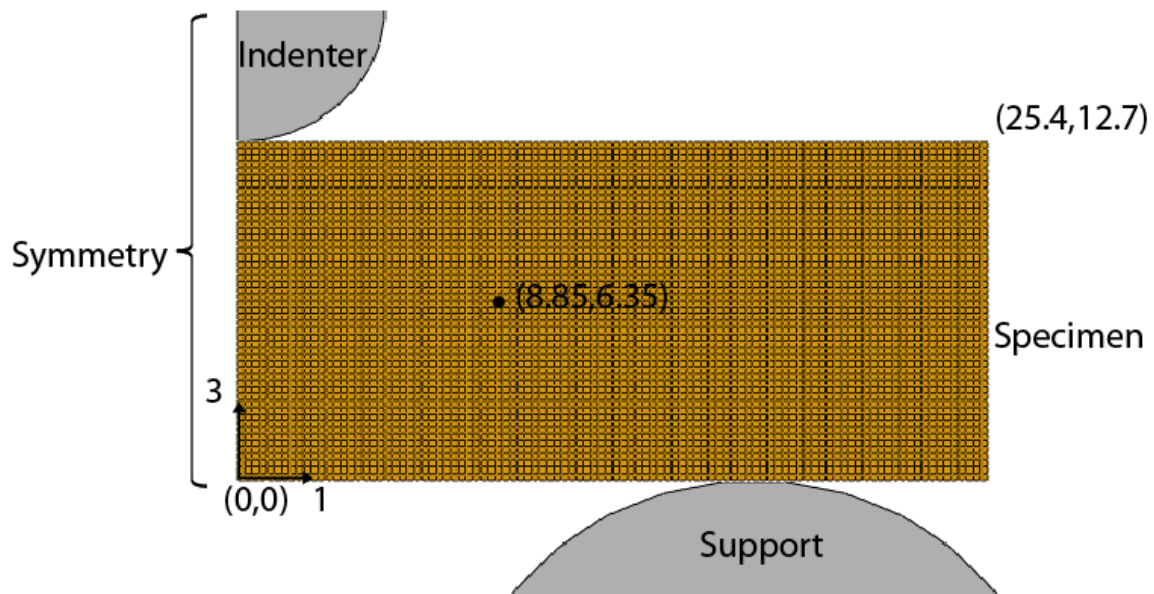


Figure 3-2. 2D FE Model for the SBS test.

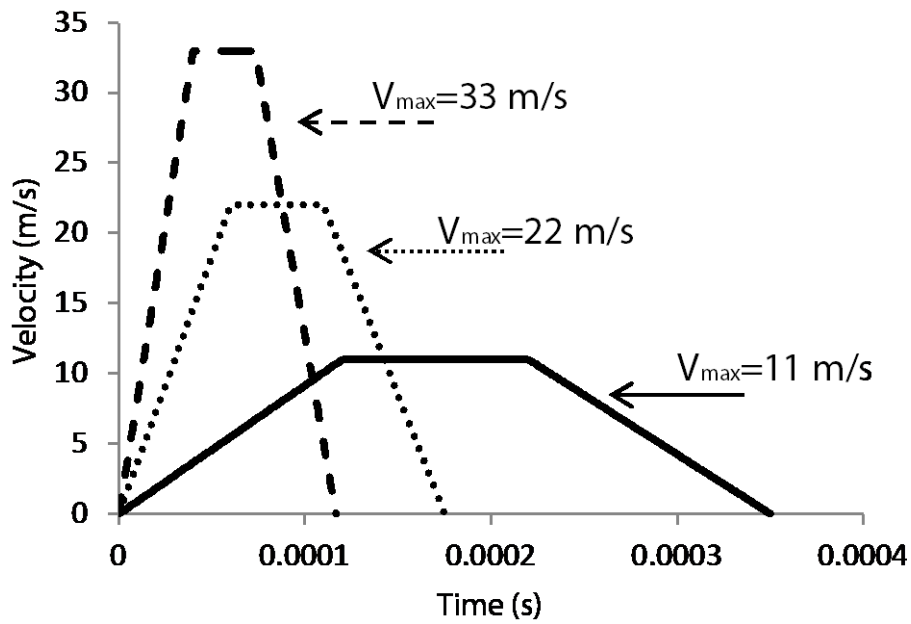


Figure 3-3. 2D FE Model for the SBS test.

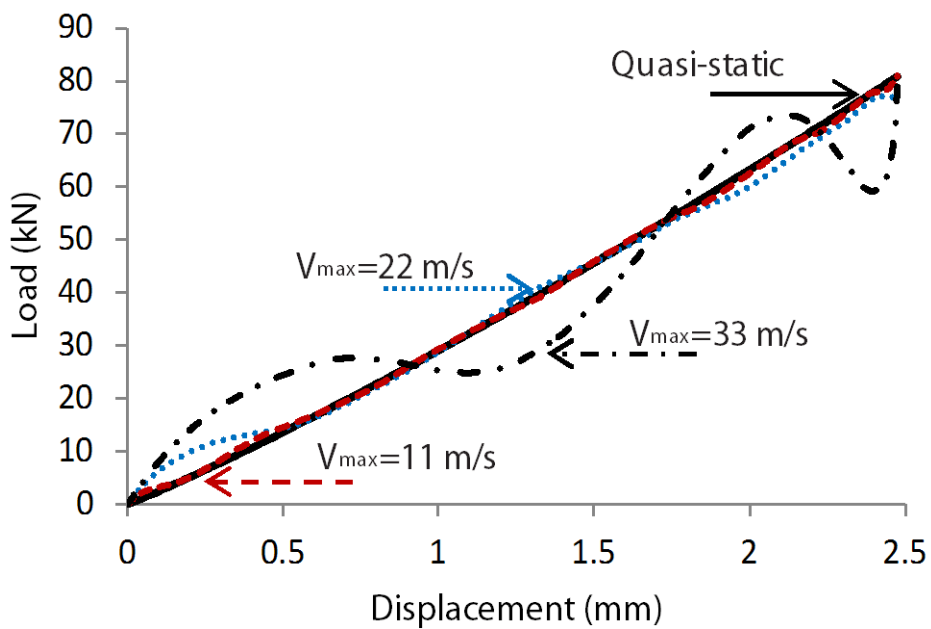


Figure 3-4. Load-displacement curves at the indenter.

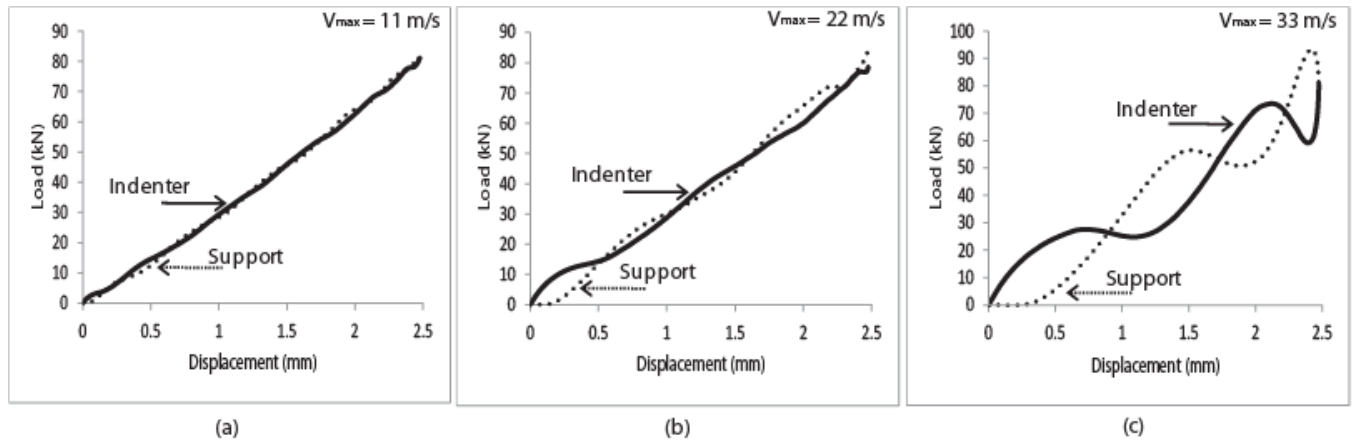


Figure 3-5. Load-displacement curves at the indenter.

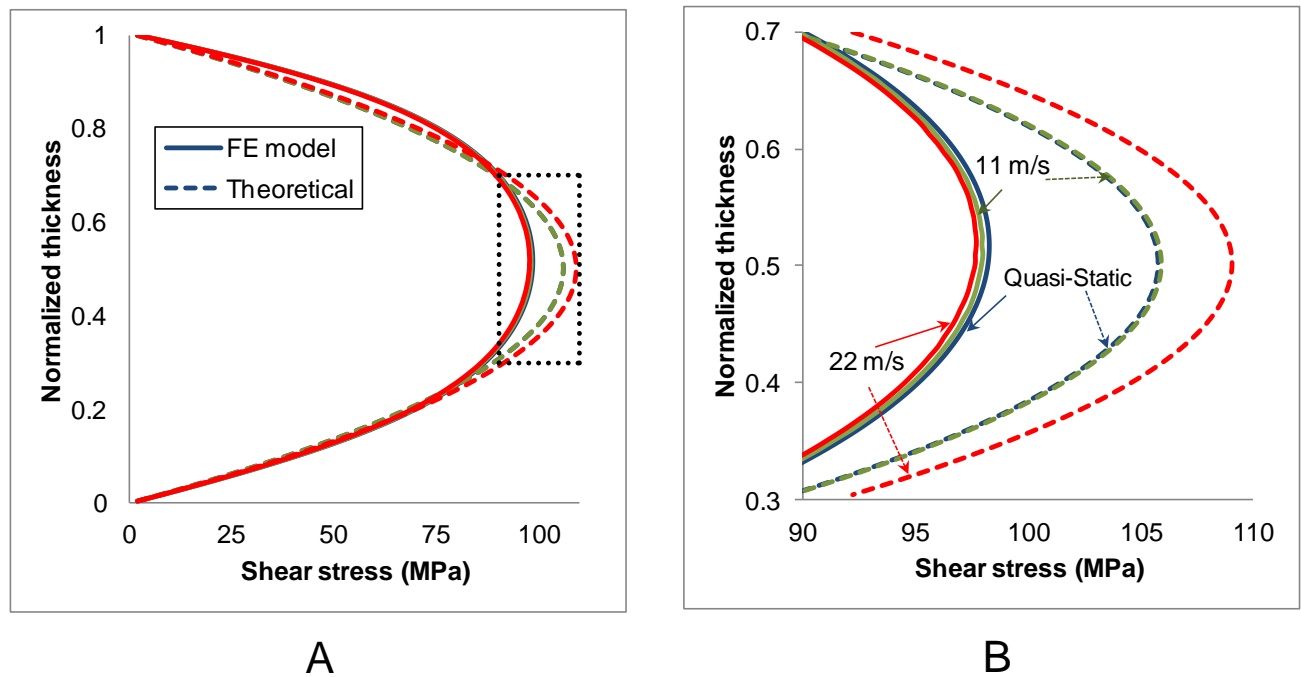


Figure 3-6. Shear stress profiles. A) Shear stress at the location of midplane between indenter and support. B) Magnified view.

Table 3-1. Material properties of the DSBS specimen for FEA [Xiao et al 2007]

Material property	Value
Density ( $\text{kg/m}^3$ )	2300
$E_1=E_2$ (GPa)	27.5
$E_3$ (GPa)	11.8
$G_{13}=G_{23}$ (GPa)	2.14
$G_{12}$ (GPa)	2.9
$\nu_{13}=\nu_{23}$	0.4
$\nu_{12}$	0.11

## CHAPTER 4

### ANALYSIS OF DELAMINATION IN 3D WOVEN COMPOSITES UNDER QUASI-STATIC LOADING USING FINITE ELEMENTS

Delamination initiation and propagation in plain woven and 3D orthogonal woven composite laminates under three-point bending were analyzed using finite element analysis. Both single and double z-yarn 3D woven composites were considered. The models were guided by experimental observations of short beam shear (SBS) tests of specimens of same material systems. A series of mechanisms including creation of transverse matrix cracks and their interaction with delamination were modeled discretely. The force-displacement curves obtained from the FE simulation were compared with those from experiments. Further parametric studies were conducted to understand the effect of z-yarns in the 3D orthogonal woven composites on delamination. The results from the FE simulations reveal that z-yarns in the 3D woven composites can play a substantial role to impede the propagation of interlaminar cracks, thus can remarkably enhance damage resistance and tolerance of the composite.

#### **Finite Element Model for 3D Woven Composites**

We selected three different types of specimens - 3D woven composites with single z-yarn and double z-yarn (SY3W and DY3W), and 2D plain woven laminated composite (2DPL) - for this study. The effect of z-yarns and inherent fracture toughness of the material on damage tolerance was investigated by comparing the SY3W and DY3W to the 2DPL specimens and varying inherent interlaminar fracture toughness of the 2DPL in a parametric study.

It is well known that matrix cracks precede delamination when a laminated composite beam/plate is subjected to quasi-static indentation or impact load. Walter et al. [Walter et al. 2010] performed short beam shear tests on 3D woven glass/epoxy

composites to understand the damage initiation and propagation mechanisms under impact loads. The experiments showed that matrix cracks initiated in resin pockets between the z-yarns and also in the weft yarns parallel to the  $y$ -axis (Figure 4-1).

Optical micrographs also showed short delaminations and crushing failure beneath the indenter. However, these failures were highly localized, but the delaminations emanating from matrix cracks significantly changed the global response of the specimens. In fact the interaction of matrix cracks and delaminations is a common feature typically observed in cross-ply laminated composites comprised of  $0^\circ$  and  $90^\circ$  layers. Woven composites, which consist of warp yarns ( $0^\circ$ ) and weft yarns ( $90^\circ$ ), are similar to cross-ply laminates, and understanding of damage mechanism in the latter can be useful for woven composites. Although continuum damage models are able to capture the non-linear behavior of composites in certain situations, they are not suitable for the discrete characteristics of damage process observed in the present study [Wisnom 2010]. So the interaction between matrix cracks and delaminations was studied and used for modeling the damage discretely [Hallett et al. 2008, Zhou et al. 2010].

Cohesive elements are widely used for modeling of delaminations and matrix cracks because of their versatility in dealing with damage initiation and evolution without defining any pre-crack [Nishikawa et al. 2011, Okabe et al. 2012]. Apart from delamination which mostly occurs at the interface between layers, the location and direction of matrix crack may be arbitrary. The extended finite element method (X-FEM) [Belytschko et al. 2009] or the augmented finite element method (A-FEM) [Ling et al. 2009] has been used to deal with these arbitrary discontinuities due to cracks in the

material system. However, it is difficult to predict exactly the creation of multiple cracks in complex material systems such as woven composites as observed in the experiment without considering uncertainties in geometric configurations, internal defects and material properties. Since our interest in the present study is focused on the investigation of delamination rather than exact prediction of the intra-laminar damage attributes in the given material system, we use the results from experiments as a guide to predict the location of matrix cracks. The results from the SBS tests conducted by Walter et al. [Walter et al. 2010] made it possible to predict the location of matrix cracks so that cohesive elements could be used in modeling of matrix cracks as well as delaminations. The potential locations for matrix cracks were assumed based on the SBS tests and found from principal stress directions for simplicity, which will be described in detail in the following sections.

As a result of FE simulation, the force versus displacement at the indenter were obtained for the 3D woven composites and used to investigate the effect of z-yarns as well as the interlaminar fracture toughness. The relationship between damage patterns and the global response was found and will be explained also.

### **Geometry and Boundary Conditions**

The microstructure of the specimens and their boundary conditions in the FE models were similar to that in previous experiments [Walter et al. 2010]. The geometric parameters of the DY3W such as yarn dimensions and yarn spacing were determined from the micrographs of 3D orthogonal woven composite [Walter et al. 2010] (Table 4-1). As shown in Figures 4-1 and 4-2 the cross-sections of the yarns were treated as rectangles.

Taking advantage of symmetry conditions, only a portion of the specimen is modeled. Due to symmetry about the  $yz$ -plane passing through the mid-span, only one-half of the specimen in the  $x$ -direction is modeled. Since the specimen is assumed to be under plane strain normal to the  $y$ -axis, one unit-cell in the width direction ( $y$ -direction) should be sufficient. Further reduction can be made as the unit-cell is symmetric about its mid-plane parallel to the  $xz$ -plane. Thus, only one half of the unit-cell needs to be considered as shown in Figure 4-1B. The indenter and support of the SBS test setup were modeled as rigid bodies.

The span of the beam (distance between the supports) in the FE model was 40 mm. The thickness of  $z$ -yarn ( $t_z$ ) in the SY3W was 0.4 mm while other geometric parameters remained the same as those in the DY3W including the configuration of crowns of  $z$ -yarns in order to investigate the effect of the thickness of  $z$ -yarn, hence the volume fraction of  $z$ -yarns, on delamination of the 3D woven composite. Since the vertical part of  $z$ -yarns play a significant role to interlaminar crack, this approach might be reasonable. In addition, the regions created by reducing the dimension of the  $z$ -yarn were replaced with matrix since the micrograph from the experiments showed more matrix region in the SY3W [Walter et al. 2010].

Plane strain boundary conditions were assigned on the front and back surface of 3D woven composites ( $x$ - $z$  planes in Figure 4-1) as well as the symmetry boundary conditions on the symmetry plane such that  $U_x=0$  (left  $y$ - $z$  plane in Figure 4-1). Eight-node brick elements were used in modeling the yarns and matrix phase and eight-node cohesive elements were used for damage modeling.



## Damage Model and Modeling Strategy

During the beginning stage of SBS tests 3D woven composite specimens undergo elastic deformation. As the load increases, matrix cracks and delaminations occur in the specimen.

The cohesive element associated with a bi-linear traction-separation law was selected for modeling of both matrix cracks and delamination. This damage law enables the traction between two surfaces to be expressed in terms of relative displacement and stiffness:

$$\sigma = (1 - D)Kd$$
$$D = \begin{cases} 0 & , d < d_0 \\ \frac{d_f(d - d_0)}{d(d_f - d_0)} & , d_0 < d < d_f \\ 1 & , d_f < d \end{cases}$$

where  $\sigma$  is the traction,  $K$  is stiffness,  $D$  is damage variable,  $d$  is displacement,  $d_0$  is the displacement at damage initiation and  $d_f$  is the final displacement [Camanho et al. 2003].

Quadratic stress-based failure criterion and mixed mode strain energy release rate criterion were used for damage initiation and propagation, respectively, for both the transverse crack and delamination:

$$\left\{ \frac{\langle \sigma_n \rangle}{\sigma_n^o} \right\}^2 + \left\{ \frac{\sigma_s}{\sigma_s^o} \right\}^2 = 1$$
$$\left\{ \frac{G_I}{G_{Ic}} \right\} + \left\{ \frac{G_{II}}{G_{IIc}} \right\} = 1$$

where  $\sigma_n^o$  and  $\sigma_s^o$  are interfacial normal and shear strength, and  $G_{Ic}$  and  $G_{IIc}$  are the Mode I and Mode II critical energy release rates. Since the locations of cohesive

elements, which would act as potential crack paths, should be defined *a priori*, it is necessary to predict accurately the locations of expected cracks. The prediction for delamination is straightforward as it occurs between adjacent plies or layers, while that for matrix crack is complex. Based on experimental observations [Walter et al. 2010] several assumptions have been made to determine the locations of potential cracks for the efficient use of cohesive elements. The assumptions are as follows:

- i) Matrix cracks occur both within the fill tows and in the matrix pocket at the tensile bottom layer.
- ii) Only a single matrix crack is created and allowed to evolve along the principal stress direction.
- iii) The crack path is a straight-line. The above assumptions are consistent with experimental observations.
- iv) The effect of a matrix crack at the compressive top-most layer on delamination can be negligible.

Formation of matrix cracks on the top layers of the beam needs special treatment. In the beginning of loading the top side is under compression and it is observed no matrix cracks form. However, after delaminations initiate, there is a redistribution of stresses and the delaminated top layers develop tensile stresses and they become sites for initiation of matrix cracks. These locations are identified from a preliminary FE analysis. To begin with, the principal directions at the centers of fill tows in the tensile region using the specimen without any damage (Figure 4-3A) were found and used for further simulation to seek the principal stress direction over the entire region as seen in Figure 4-3B. In the following FE model, other cohesive elements for delaminations were

placed between layers with the cohesive element for matrix cracks in the tensile region placed along the principal direction found in the previous step, thus the principal directions in the compressive region after delamination could be found. In the second FE analysis using the specimen of Figure 4-3B the load was applied until the moment that delamination occurred so that redistributed stress field could be obtained. In order to determine the principal stress directions in the weft yarns, stress values over the all elements of the weft yarns were checked and appropriate principal stress directions incurring tensile failure were chosen. The principal directions determined are shown in Figure 4-3. Note that the angles shown in Figure 4-3 are measured from the z-axis. As a result of consecutive finite element simulations, the final configuration of Figure 4-3C could be obtained and became the final FE model for the study of delamination damage of the 3D woven composite materials.

### **Material Property and Data Selection**

Material properties of the 3D woven composites used in the analyses are listed in Table 4-2. Elastic properties of the yarns were computed using the micromechanics formulas developed by Chamis et al. [Chamis et al. 2007]. The material system was S2 glass fiber/ SC-15 epoxy with 62% fiber volume fraction. The strength and critical energy release rate values for the cohesive elements were selected from the literature. The properties of cohesive elements for matrix crack and delamination were assumed to be same.

As Mode II shear strength value for the cohesive elements, the apparent ILSS value reported by Walter et al. [Walter et al. 2010] was chosen (Table 4-2). This value was much lower than the range, 55 to 103 MPa, given by AGY manufacturer of S2 glass yarn, [AGY]. The ILSS could be much lower due to the voids and the type of binder

used in the manufacturing process [Wisnom et al. 1996, Tanoglu et al. 2001]. The specimens test by Walter et al. were manufactured using vacuum assisted resin transfer molding (VARTM) process [Walter et al. 2010], the ILSS value could be lower because of inherent defects such as voids involved during VARTM process. Based on the Mode II shear strength determined for the cohesive element, a Mode I normal strength value was estimated appropriately as listed in Table 4-2

In addition, the critical energy value for the cohesive element could be determined using available sources such as a Mode II fracture toughness value of quasi-isotropic and cross-ply composite with SC-15 reported by Huang [Huang 2008], which was about 2000 N/m, as well as a Mode I fracture toughness of SC-15 epoxy provided by Applied Poleramic, the provider of SC-15 epoxy, which was 1000 N/m [Applied Poleramic]. A bi-linear traction-separation law controlling the behavior of the cohesive element can be depicted by a triangle as shown in Figure 4-4.

If the critical displacement denoted by 'C' in Figure 4-4 remains the same, the critical energy will be changed (from the area of 'OBD' to the area of 'OAD') with the change of the strength (from 'B' to 'A'). This approach can explain the fact that fracture toughness tends to decrease due to the lowered strength [Madhukar et al. 1992]. Otherwise the lowered strength value can enhance damage resistance by increasing the critical distance of cohesive element under the assumption of same fracture toughness value (from the area of 'OBD' to the area of 'OAE') and might not be practical for this study. With these considerations, the critical energy value for the cohesive element was determined as listed in Table 4-2.

### Finite Element Model for 2D Plain Woven Laminates

A plain woven laminate (2DPL) with stacking sequence  $\left[ (0^{pw}/45^{pw})_2/\bar{0}^{pw} \right]_S$  was also analyzed. The 2DPL was chosen for comparison with 3D woven composites thus investigating the effect of z-yarns on delamination behavior. For the sake of simplicity of the FE simulation, each plain woven lamina was homogenized as an orthotropic material and one-half of the beam was modeled using eight-node plane strain elements (Figure 4-5). The material properties of the homogenized plain-woven layer are listed in Table 4-3 [Xiao et al. 2007].

The material properties for  $\pm 45^{pw}$  could be obtained using coordinate transformation.

The creation of matrix cracks and placement of cohesive elements in 2DPL specimens were similar to the procedures used for 3D woven laminates. Our approach is confirmed by the experimental observation that a single matrix crack tended to occur inside weft yarns of the  $0/90^{pw}$  [Walter et al. 2010]. However, the tensile cracks in the matrix pocket of outer most layer seen in the 3D woven composites were not observed in plain woven laminates and hence they were not introduced in 2DPL specimens. Furthermore, transverse shear stress vanishes at the free surface. Therefore cohesive elements were merely placed in the middle regions of the specimen only. Cohesive elements for possible matrix cracks were placed in the three inner homogenized layers of  $0/90^{pw}$  as shown in Figure 4-6. Principal stress directions were found in locations corresponding to the centers of fill tows through same procedure as 3D woven composites considering tensile region and compressive region after delamination

individually. The possible matrix crack directions used in this simulation are shown in Figure 4-6.

A parametric study varying Mode I/Mode II interlaminar fracture toughness (370/830 N/m, 1000/2000 N/m and 1000/3300 N/m) was performed in order to investigate the effect of interlaminar fracture toughness on the global behavior and damage pattern of the 2DPL specimens. These studies are referred to as Case I, Case II and Case III (Table 4-4), respectively.

## **Results and Discussions**

### **3D Woven Composites (SY3W and DY3W)**

The force and displacement at the indenter were recorded during the FE simulations. The force at a given displacement can be a proper measure to examine the macroscopic behavior the specimen. The results for both SY3W and DY3W are shown in Figure 4-7.

Two force-displacement curves from the tests [Walter et al.] are also plotted for comparison. Note the two experimental curves of the SY3W type show slightly different behavior after damage initiation. The solid lines indicate the result from the FEM. Since the same properties for the cohesive element were used and most configurations remained the same except for the thickness of z-yarns in the simulation it can be inferred that the difference between two FEM simulations (solid curves in Figure 4-7) resulted from the effect of z-yarns on delamination. The peak load value of DY3W is higher than that of SY3W. This reveals that z-yarns can delay the damage initiation point. Besides the forces beyond the peak loads between two cases are quite different. The SY3W showed that an abrupt force-drop right after the peak loads whereas the force-drop in DY3W is not noticeable or fairly small. Additionally the SY3W has another

peak load followed by sudden force drop again which does not occur in the DY3W. These characteristics agree well with experimental results shown in Figure 4-7.

The variation of strain energy and damage energy as a function of indenter displacement obtained from the FE analyses are shown in Figure 4-8.

The strain energy represents the recoverable elastic energy stored in the specimen at any given instant. The damage energy is the unrecoverable energy dissipated by the cohesive elements. It is seen that the sudden force-drop in the load-deflection diagram corresponds to sudden increase in damage energy. One can note that the damage energy in the DY3W specimen increases steadily without any abrupt damage process or loss of stiffness. From these figures it is clear that z-yarn can enhance damage resistance and tolerance. However, optimum amount of z yarn should be used so that there is no deterioration in the composite properties [Rao et al. 2009 ].

### **Plain Woven Laminated Composites (2DPL)**

Unlike 3D woven composites, only one configuration, but with various cohesive parameters, was considered in studying of the 2DPL. Although the same properties for cohesive element as 3D woven composites were initially used for the 2DPL, interlaminar fracture toughness values seems to be different since woven laminated composites have higher fracture toughness than unidirectional fiber composite due to undulation of yarn or crimp [Kalarikkal et al. 2006]. The force-displacement curves of both SY3W and 2DPL obtained from the tests [Walter et al. 2010] showed different behavior during unloading. The force drop of the SY3W was very rapid while that of the 2DPL was gradual. This could be explained by the higher fracture toughness values of woven laminates compared to tape laminates. Out of the three sets of interlaminar fracture toughness values used the force-displacement curve of Case III with the

highest fracture toughness exhibited load-displacement behavior similar to experimental results as shown in Figure 4-9.

Lower fracture toughness values (cases I and II) resulted in different damage pattern and produced different load-displacement curves.

The force versus displacement curves at the indenter with respect to three different interlaminar fracture toughness values are plotted in Figure 4-9. The difference among the force-displacement curves due to different fracture toughness values is apparent. As the fracture toughness values were increased, the peak loads were increased and the rate of force drop just beyond the peak load became moderate. If the interlaminar cracks propagate mainly without other delaminations the forces will decrease rapidly. As seen in Figure 4-9, the rapid force drops in the Case I and Case II were attributed to the damages that occurred with very small increment of displacement and can be identified with the damage energy variation in Figure 4-10. Sudden increase of damage energy was accompanied by sudden loss of strain energy as well. But the damage energy of Case III increases gradually along with the increase of the strain energy.

These variations of global responses are highly dependent on how damage evolves. By observing the history of damage development, it is possible to gain insight into understanding delamination damage behavior of composites. Once delamination occurs from the matrix crack it will propagate and reach the free end of specimen (b-1 and b-2 in Figure 4-11).

The propagation of the crack to the free end causes the force to decrease abruptly. After a complete delamination developed over the region from matrix crack to



the end of the specimen, the force increases with displacement and strain energy is stored until the state of stress in another interlaminar region satisfies the criterion for crack initiation and propagation. Then the force will decrease suddenly again as shown in the Case I of Figures 4-9, 4-10 and Figure 4-11C. Case II showed that the resistance to crack propagation increased with the interlaminar fracture toughness. Further increase in interlaminar fracture toughness (Case III) totally changed the tendency of crack propagation.

High resistance against cracks kept the interlaminar delamination from propagating. Before a delamination reached the end of specimen, another delamination occurred. This caused a gradual force drop instead of an abrupt drop in Cases I and II (Figures 4-9, 4-10 and 4-13). The relationships between the damage pattern in Figures 4-10 through 4-12 and the force-displacement curves in Figure 4-9 are similar to the test results of Walter [Walter 2011].

It could be observed that the crack propagation of the SY3W reached the end of the specimen and resulted in the force-displacement curve in Figure 4-7, while 2DPL and DY3W didn't allow delamination to propagate to the end of the specimen and other delaminations occurred at the same time they resulted in gradual force drop as shown in Figure 4-14. It should be noted that Figure 4-14 has been obtained from a dynamic test but exhibited similar damage pattern as quasi-static test demonstrating that quasi-static indentation tests can provide insight into damage development due to impact loading in laminated 3D composites.

From these results, it is possible to identify that the role of z-yarns on interlaminar delamination. Z-yarns provide a constraint to reduce the relative displacement between

two layers thus enhancing the resistance against crack propagation. Thus the z-yarns result in higher apparent interlaminar fracture toughness.

### **Summary and Conclusion**

The effect of z-yarns on damage tolerance of 3D woven composites was studied using the SBS tests. It is found that tensile or transverse matrix cracks develop in the matrix pocket between z-yarn crowns and the center of weft yarns. Cohesive elements associated with bi-linear damage model were placed along the principal stress direction for the matrix cracks. These elements are used in modeling of interlaminar delamination as well. The RVE model and simplified plain strain FE model provided good results to understand the role of z-yarns and inherent interlaminar fracture toughness.

From the FE simulation of SY3W and DY3W specimens, it is found that proper amount of z-yarns can enhance damage resistance and tolerance. This conclusion agrees well with the result from the end notch flexure (ENF) specimen of 3D woven composites by Pankow et al. [Pankow et al. 2011]. It was found that the z-yarns prevent two neighboring layers from being separated. In the case of 2DPL crimp or undulation of the yarns seems to interrupt the propagation delamination crack providing better damage tolerance than single z-yarn 3D woven composites. However, double yarn 3D woven composites (DY3W) have superior damage tolerance compared to 2DPL and SY3W. As it turned out, the prevention of crack growth along an entire interface is a key element to enhance damage tolerance. When damage occurs in different layers before the delamination propagates in the entire specimen, more energy is dissipated in various interlayer damage mechanisms increasing the damage tolerance of the laminated composite structure.

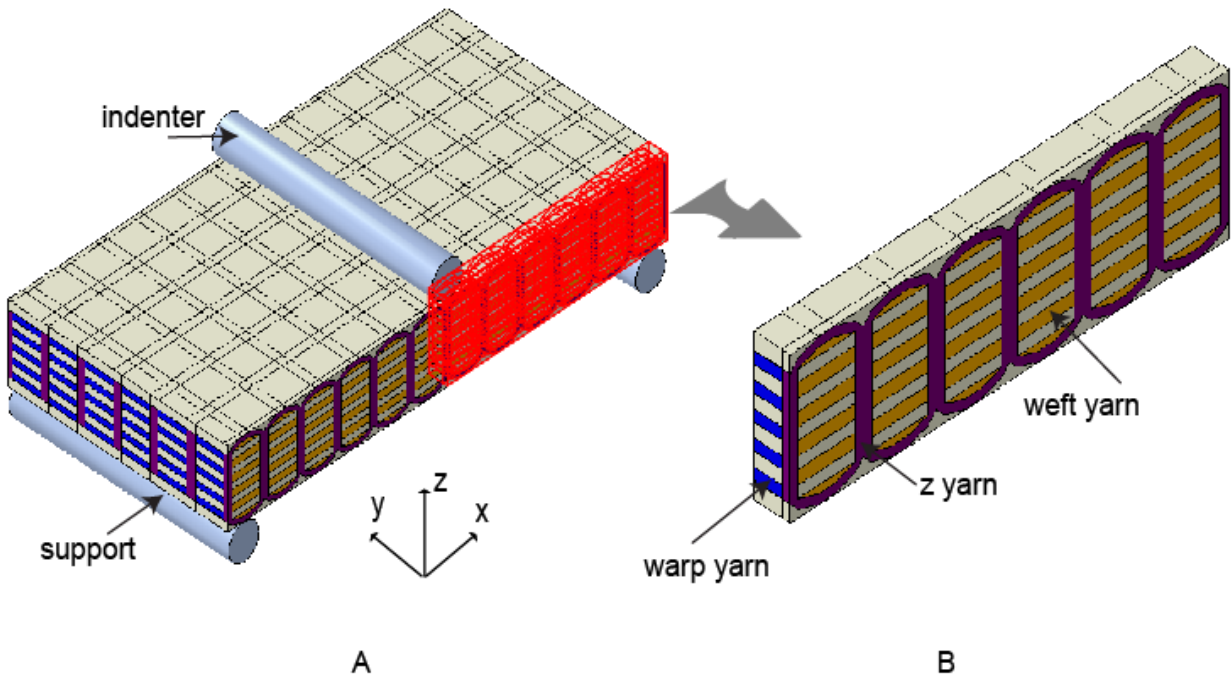


Figure 4-1. 3D woven composites for FE model. A) Orthogonally woven 3D composite with SBS setup. B) Representative Volume Element (RVE) for FE model.

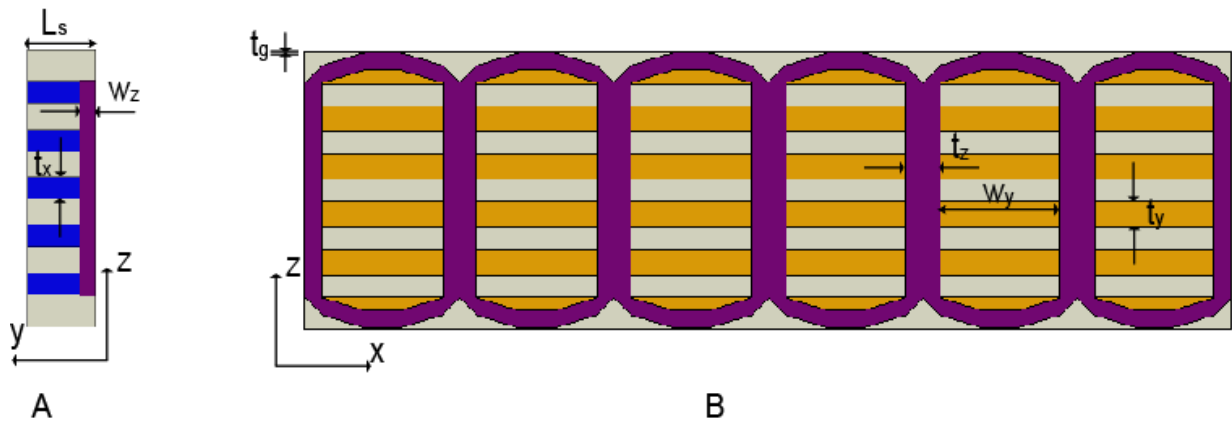


Figure 4-2. Geometric parameter of RVE. A) left side view. B) front side view.

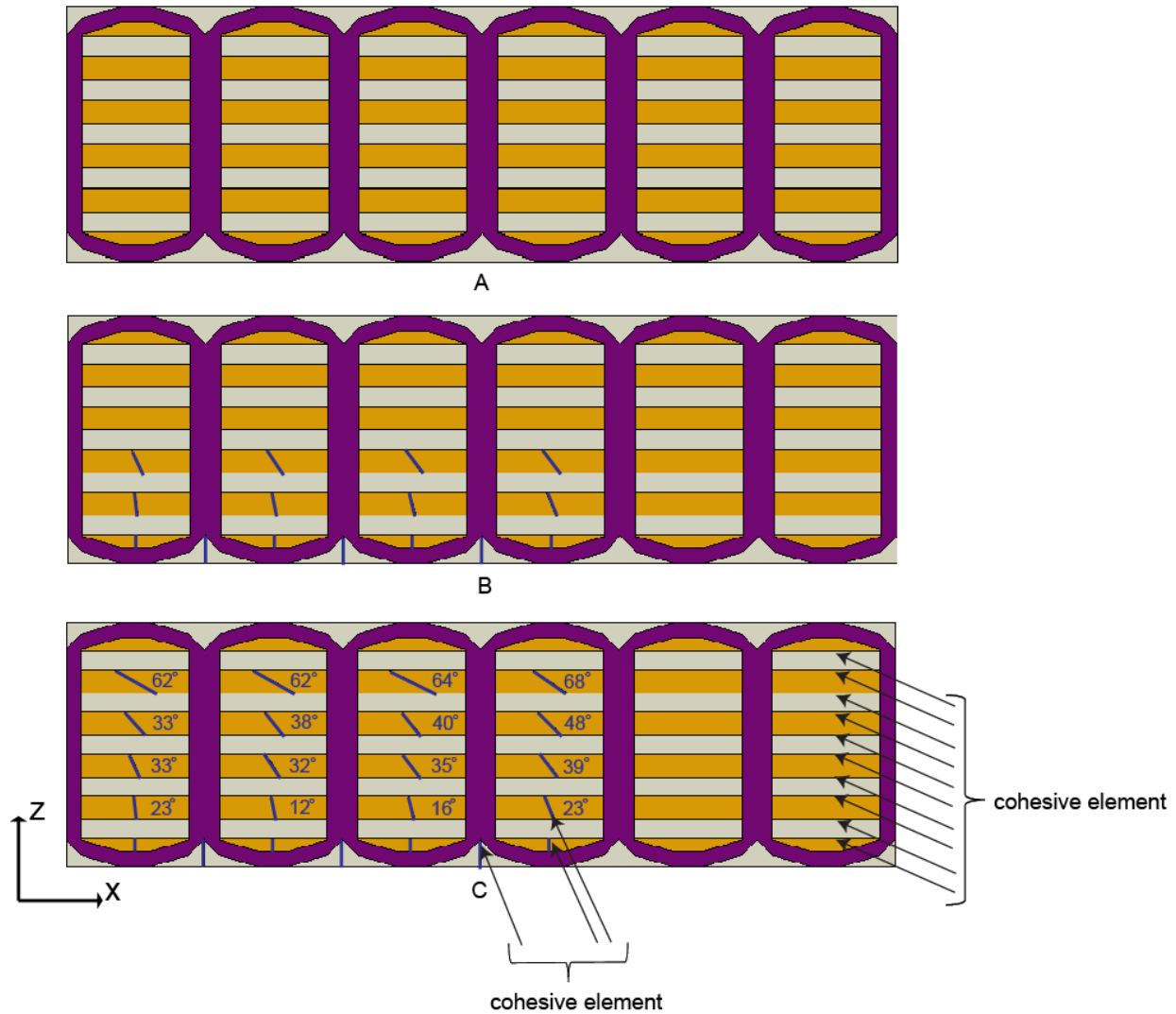


Figure 4-3. Prediction of matrix cracks. The lines indicate potential crack paths. A) Cross-section for exploring principal stress directions. B) Principal stress directions in the tensile region. C) Principal stress directions in the entire regions.

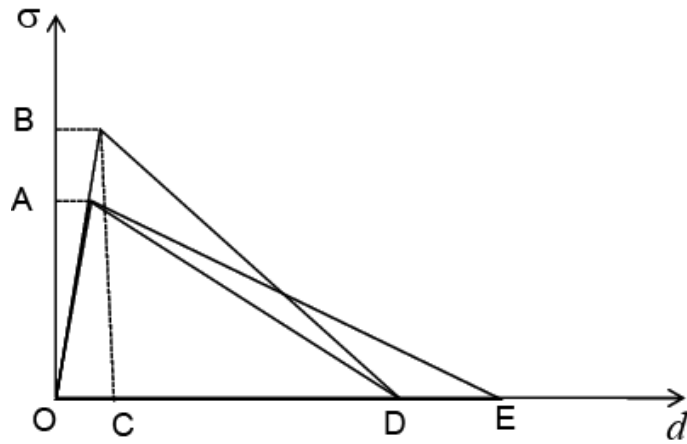


Figure 4-4. Traction-separation law of cohesive element.

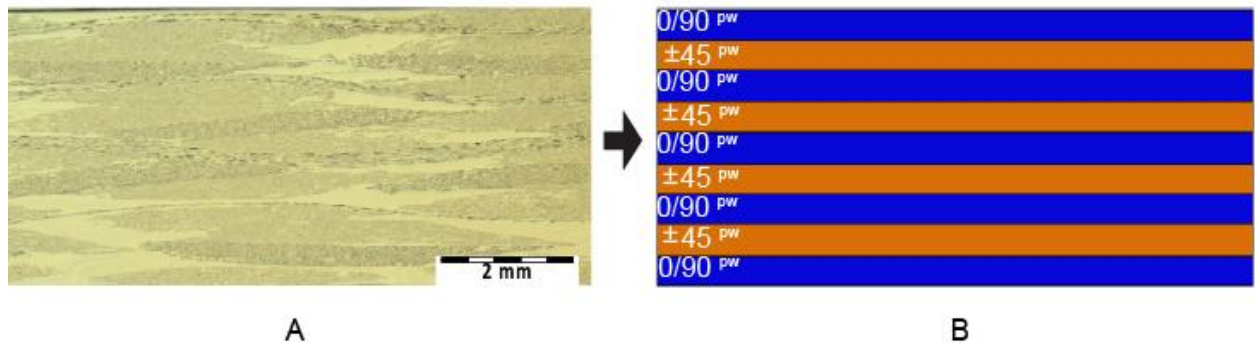


Figure 4-5. 2D plain woven composite. A) Cross-section of 2D plain laminated composite. B) Homogenized FE model.

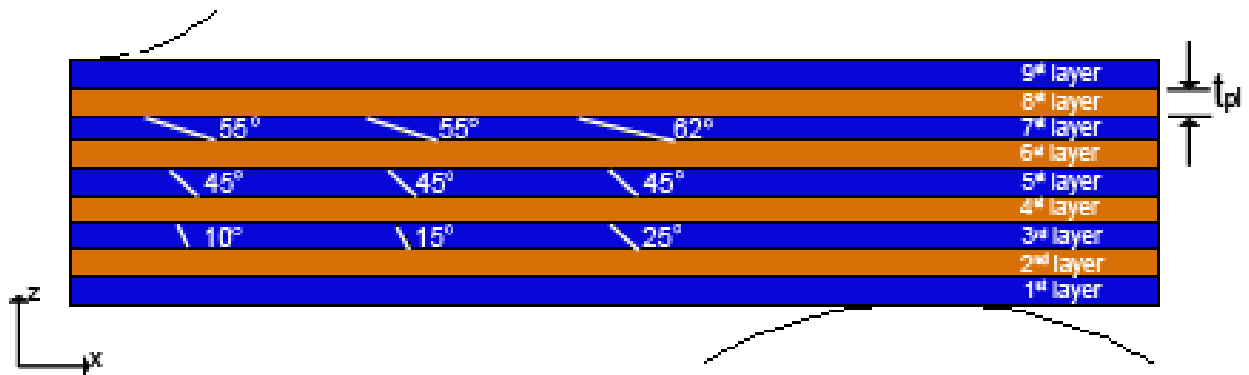


Figure 4-6. Implementation of the cohesive element on homogenized 2D plain woven composite.

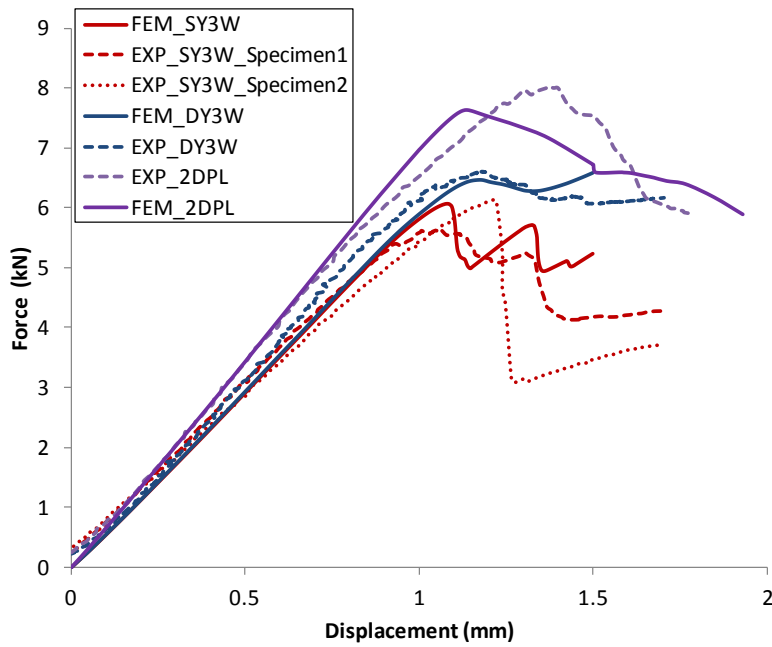


Figure 4-7. Force-displacement curves of the single/double z-yarn 3D woven composites.

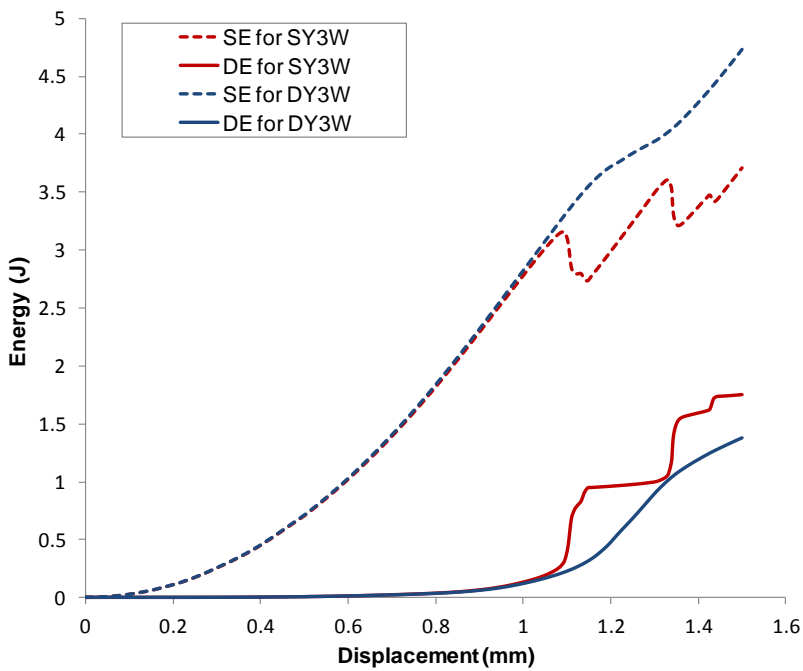


Figure 4-8. Strain energy and damaged energy versus displacement curves of the SY3W and DY3W. SE and DE indicate strain energy and damage energy, respectively.

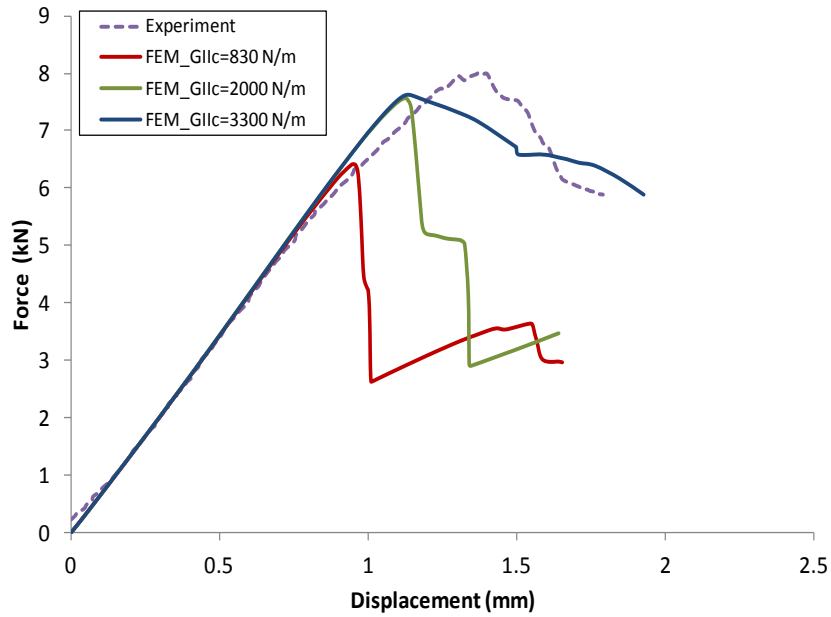


Figure 4-9. Force-displacement curves of the single and double z-yarn 3D woven composites.

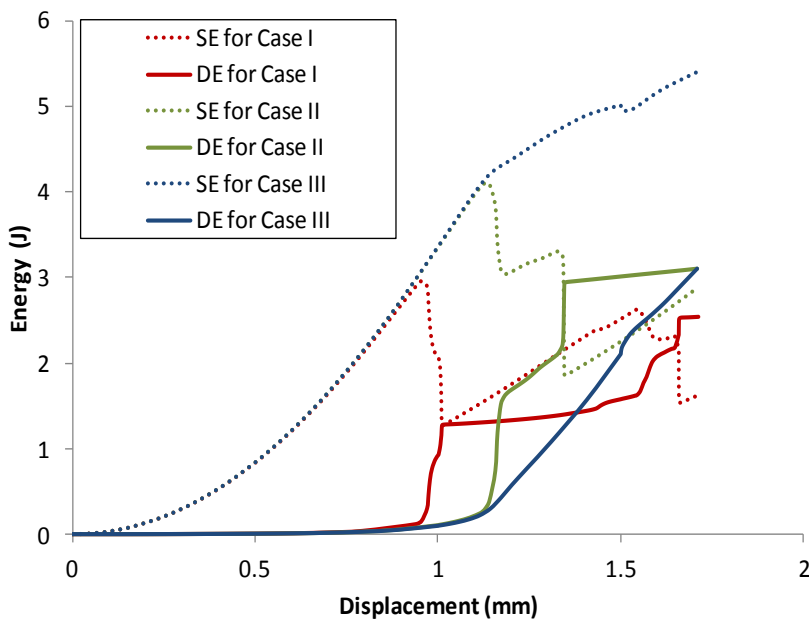
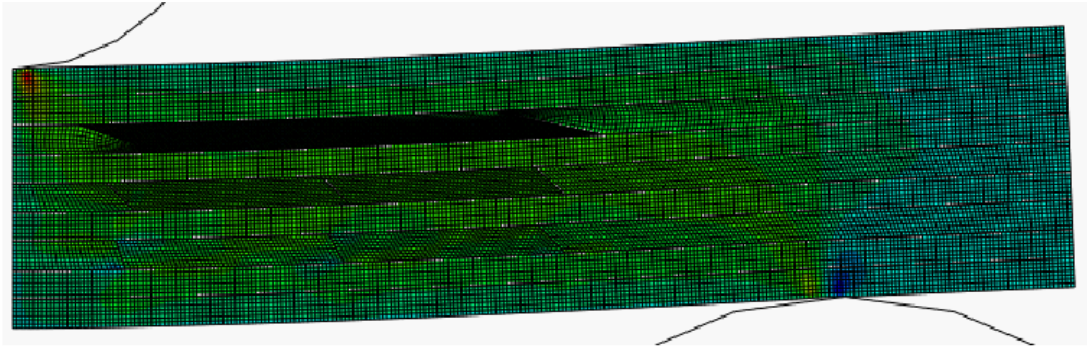
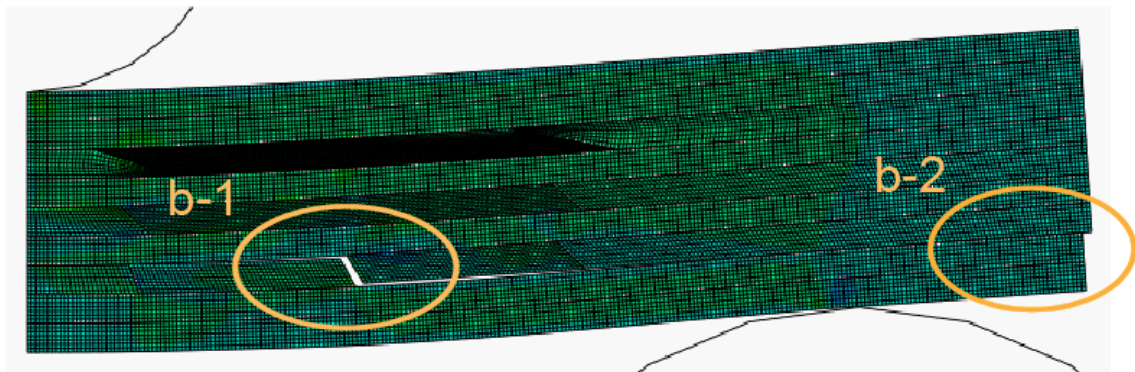


Figure 4-10. Strain energy and damage energy versus displacement curves of the 2DPW. SE and DE indicate strain energy and damage energy, respectively.

A



B



C

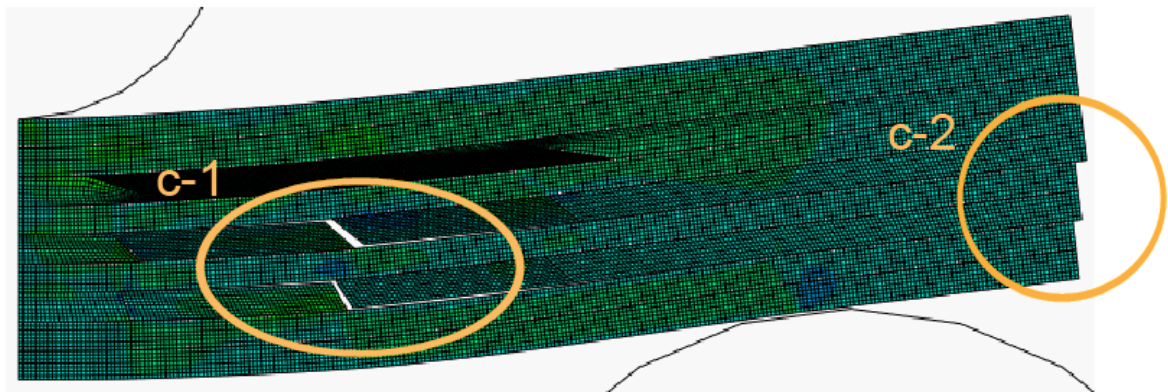


Figure 4-11. Damage evolution of baseline composite-Case I. A)  $d=0.8\text{mm}$ . B)  $d=1.1\text{mm}$ . C)  $d=1.7\text{ mm}$ .



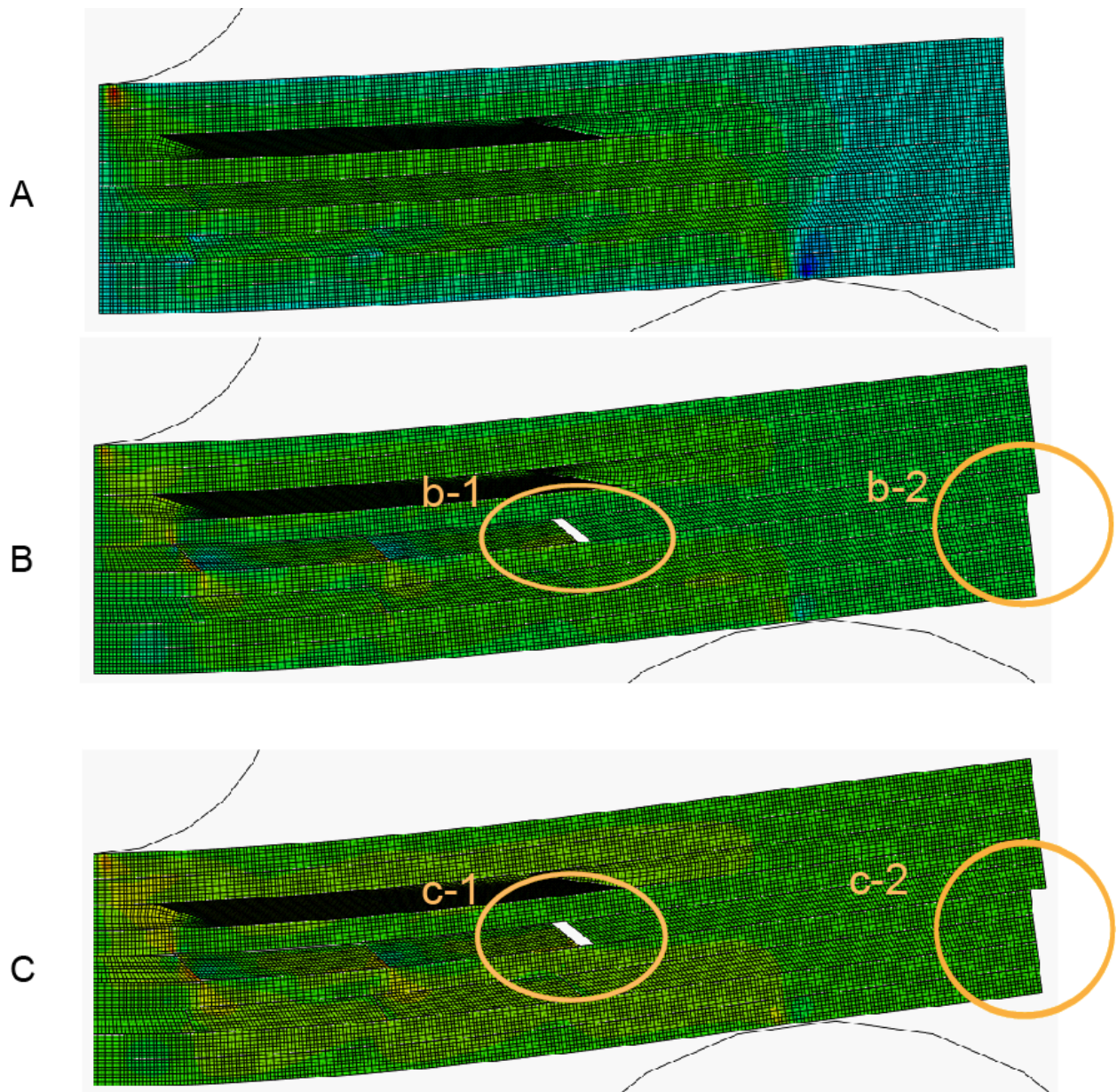
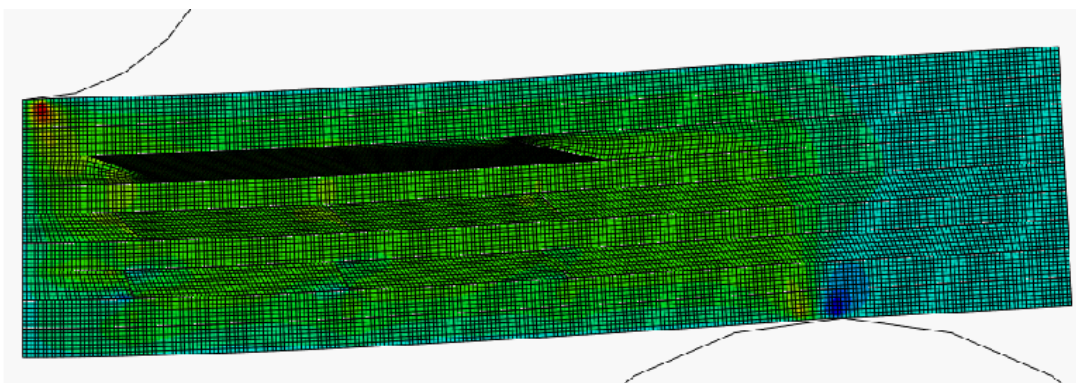
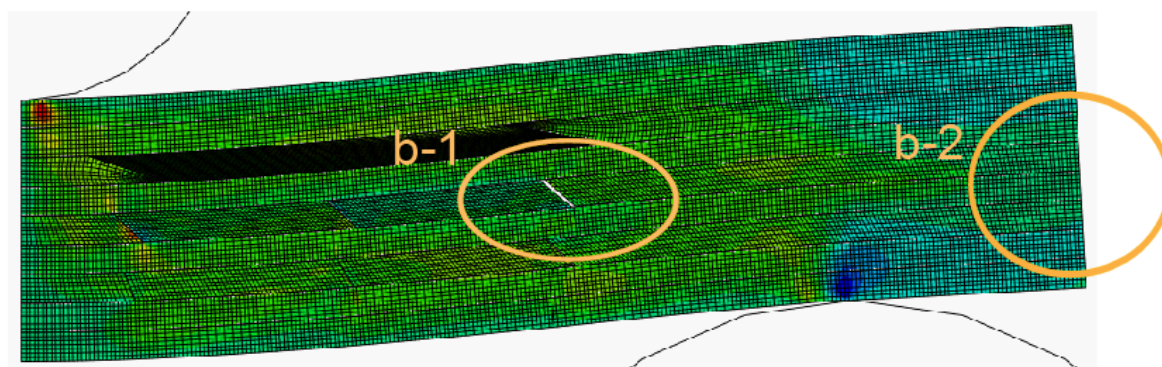


Figure 4-12. Damage evolution of baseline composite-Case II. A)  $d=1\text{mm}$ . B)  $d=1.5\text{mm}$ . C)  $d=1.75\text{ mm}$ .

A



B



C

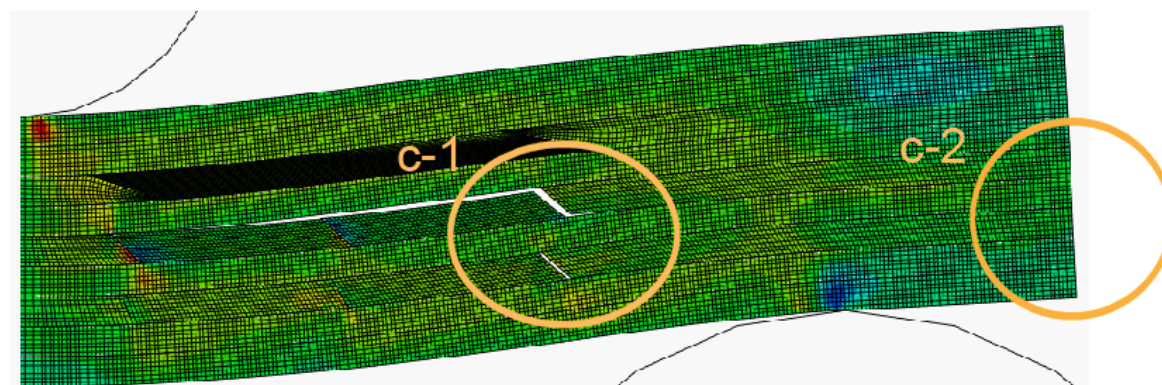


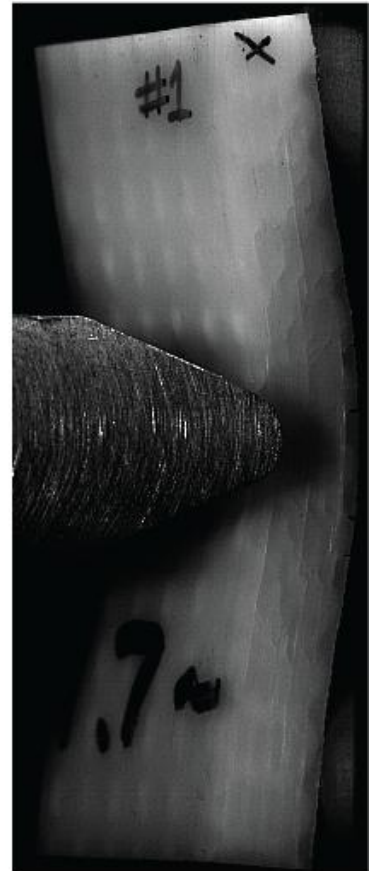
Figure 4-13. Damage evolution of baseline composite-Case III. A)  $d=1\text{mm}$ . B)  $d=1.5\text{mm}$ . C)  $d=1.75\text{ mm}$ .



A



B



C

Figure 4-14. Delamination patterns in the composites. A) 2DPL. B) SY3W. C) DY3W.  
[Walter 2012].

Table 4-1. Dimensions of geometric model of RVE. The subscripts 'x', 'y' and 'z' indicate warp yarn, weft yarn and z yarn, respectively. (unit: mm)

$L_s$	$w_z$	$t_x$	$t_y$	$t_z$	$w_y$	$t_g$
1.8	0.4	0.5	0.6	0.8	2.8	0.075

Table 4-2. Material properties of the constituents the 3D woven composites

Yarns, Epoxy and Cohesive element								
Yarns (Transversely isotropic)								
$E_1$ (GPa)	$E_2$ (GPa)	$E_3$ (GPa)	$\nu_{12}$	$\nu_{13}$	$\nu_{23}$	$G_{12}$ (GPa)	$G_{23}$ (GPa)	$G_{31}$ (GPa)
54.9	11.4	11.4	0.26	0.26	0.29	4.4	4.4	4.4
Epoxy			Cohesive element					
$E$ (GPa)	2.7	$\nu$	0.3	Mode I/II Strength (MPa)	23/33	Mode I/II Fracture toughness (N/m)	370/830	

Table 4-3. Elastic properties for plain woven composites

$E_1=E_2$ (GPa)	$E_3$ (GPa)	$G_{13}=G_{23}$ (GPa)	$G_{12}$ (GPa)	$\nu_{13}=\nu_{23}$	$\nu_{12}$
27.5	11.8	2.14	2.9	0.4	0.11

Table 4-4. Parameters for cohesive element in baseline composite model

	$\sigma_{\max}$ (MPa)	$G_{Ic}$ (N/m)	$\tau_{\max}$ (MPa)	$G_{IIc}$ (N/m)
Case I	23	370	33	830
Case II	23	1,000	33	2,000
Case III	23	1,000	33	3,300



## CHAPTER 5

### DAMAGE RESISTANCE OF HYBRID COMPOSITES WITH FUNCTIONALLY GRADED MATERIALS

Along with the attempts to enhance material properties such as strength and fracture toughness a way to reduce stress or strain energy release rate (SERR) subjected by external loading can be a significant consideration in the design and operation of composite structures. That is because the stress or strain energy release rate values in the material should be less than the strength or fracture toughness of the material in order to prevent failure of a material. For laminated structures, interlaminar shear stress can be a proper measure to evaluate the damage resistance of materials. As discussed in previous chapters the beam-like specimens subjected to quasi-static or low velocity impact loading exhibit a typical shear stress distribution wherein the maximum value occurs beneath the contact surface. Although the shear stresses at this location create delamination, they do not propagate due to rapidly diminishing shear stresses away from the loading point. The shear stresses are almost negligible near the top surface of the beam away from the point of contact. There is another location where the shear stresses are high enough to cause delaminations. This is at the mid-plane of the beam where the parabolic shear stress profile attains a maximum. In fact this region of maximum shear stress is substantially large. Hence, delaminations can propagate all along the length of the specimen until they reach the ends as the shear force is constant in SBS specimens extending the region of maximum shear stress. In general, the delamination due to an impact loading initiates when interlaminar shear stress exceeds interlaminar shear strength.

As a method to reduce the maximum interlaminar shear stress, hybrid composites comprised of more than two materials or functionally graded materials (FGM) with

continuously varying material property can be considered. In the present study impact damage resistance of hybrid laminated composites and functionally graded laminated composites are investigated. The motivation for this approach comes from some earlier studies on functionally graded beams [Sankar 2001] and hybrid laminates [Sankar 1989]. It was found that the transverse shear stresses get redistributed in FG beams and hybrid laminates.

The specimens of hybrid composites studied have various combinations based on the volume fraction of carbon fiber composite (CFC) and glass fiber composite (GFC), stacking sequence while the functionally graded composite have three different aspects. The descriptions of those specimens are shown in Table 5-1.

### **Effect of Hybrid Composites on Reducing the Maximum Shear Stress**

#### **Finite Element Model for Maximum Shear Stress**

The shear stress profiles including maximum values in various specimens under an assumed force were found using FEM since the evaluation of damage resistance of various materials could be achieved by comparing the maximum interlaminar shear stress. The force in the FE model was assumed as a Hertzian contact force given by

$$p = 100 \sqrt{1 - \left(\frac{x}{3}\right)^2} \text{ N/mm}, |x| \leq 3 \text{ mm}$$

The FE model to determine the shear stress profiles is shown in Figure 5-1. Due to symmetry, one half of the specimen was modeled using plane strain elements. The dimensions of the half-specimen was 100 mm x 15.4 mm. Symmetric conditions were implemented at  $x=0$ , and the vertical displacements at  $x=100$  mm were constrained. The shear stress profiles at the location of  $x=50$  mm (50 mm from the symmetry plane) were obtained from the FE model.

The material properties used in the FE model are given in Table 5-2. The properties for the FGM were found using the weighted average based on volume fraction of the CFC and the GFC. This approach was based on the recent results obtained by Banerjee [Banerjee 2012] using micromechanics methods for hybrid composites.

## **Results and Discussion**

**Hybrid composites with loading on the harder (stiffer) side.** Figure 5-2 shows the shear stress profiles of hybrid composites with carbon fiber laminates placed on the loading side. In the same figure shear stress results for FGM with linearly decreasing stiffness from the loading side to the free side are also presented. The maximum shear stress increases with the amount of carbon fiber layer. The maximum shear stress value of the LS36Hybrid is almost same as that of homogeneous composite such as the GFC or the CFC. It should be noted that the shear stress profile of the GFC is exactly the same as that of the CFC. The maximum shear stress in the LSFGM is higher than that of the GFC or CFC. Interestingly, the location of the maximum shear stress is shifted from the midplane toward the loading side, and thus can affect the point where delamination will occur.

**Hybrid composites with loading on the softer side.** Figure 5-3 shows the shear stress profiles of the hybrid composites with carbon fiber laminates placed on the bottom (free) side. As the volume fraction of carbon fiber is increased, the maximum shear stress becomes higher. The FSFGM has higher maximum shear stress than the homogeneous material. The location of the maximum shear stress is shifted from the middle toward the free side direction.

**Hybrid composites stiffened on the top and bottom sides.** Figure 5-4 shows the shear stress profiles of the hybrid composites with carbon fiber laminates placed on the both loading and free sides. The locations of the maximum shear stress values in all the hybrid composites stiffened on both sides are at the middle. The maximum shear stress values of both the hybrid composites and the FGM are lower than those of the composites made of a single material. The DS18Hybrid composite has the lowest value while the DSFGM has the value between the hybrid composites and the composites of a single material.

**Functionally Graded Composites.** Figure 5-5 shows the shear stress profiles of the FGMs. The DSFGM has lower maximum shear stress level compared to homogeneous composites while the LSFGM and the FSFGM have higher maximum shear stress values. Like the hybrid composites, the locations of the maximum shear stress in the LSFGM and the FSFGM are away from the midplane.

**Comparison of maximum shear stresses.** Figure 5-6 shows the comparison of the maximum shear stress values. The hybrid composite DS18Hybrid has the lowest value which is about 11 percent less than the homogeneous beam (GFC or the CFC) while both the LSFGM and the FSFGM have the highest value which is about 2.8 percent more. It can be expected that the specimen with lower shear stress level has higher damage resistance because an extra force or energy would be required to reach the shear strength value.

#### **Delamination Behavior of Hybrid Composites under a Quasi-static Indentation Finite Element Model for Delamination**

It can be expected that the hybrid composite stiffened on both sides would show higher peak load over the one-material composite specimens since lower shear stress



has more margin to reach the strength value. Two FE models to determine peak loads of various specimens described in Table 5-1 under 3 points bending were considered. (Figure 5-7C) One has only delaminations. (Figure 5-7A) The other has matrix cracks and delaminations (Figure 5-7B). All specimens in the FE models consist of 22 layers. Cohesive elements were placed between layers as mentioned in Chapter 4 thus delaminations were allowed to be included in the FE models. In the case of the specimen with matrix cracks, both the matrix cracks and the delaminations are modeled using the cohesive elements. The matrix cracks were placed at the location of  $x=37.5$  mm from the symmetry line. Plane strain elements were used for the half model due to symmetry. Both the indenter and the support were modeled using rigid bodies. The displacement of indenter was defined as a boundary condition and the load corresponding to each displacement was found. The peak loads from both FE models were compared so as to analyze the effect of matrix cracks on damage resistance. It is found that the matrix cracks altered the layer in which delaminations occurred.

## **Results**

Figure 5-8 shows the peak loads of all hybrid specimens considered in this study. Figures 5-9 through 5-20 show the load-deflection curves and the damage patterns in various specimens. Obviously the specimens with matrix cracks exhibit lower peak loads. This is because there is stress concentration at the tip of the matrix cracks enabling the delaminations to propagate at lower loads. As the matrix cracks were introduced the location of delamination shifts from the maximum interlaminar stress location to the interface that contains the crack tip. The DS18Hybrid composite has the highest peak load and hence highest damage resistance. Detailed discussions about

the location of delamination as well as load-displacement curve for individual specimens are given in the following.

Figure 5-9 and Figure 5-10 show the load-displacement curve and the deformations after delamination of the GFC and the CFC, respectively. The location of delamination changed from the 11<sup>th</sup> interface (the middle of the specimen) to the 8<sup>th</sup> interface. As long as the specimen has a symmetric configuration delamination occurs at the middle since the shear stress is maximum at the center. However the matrix cracks cause the stress field to be redistributed and change the delamination site.

Figures 5-11 through Figure 5-14 show the load-displacement curve and the deformations after delamination of the LS9Hybrid composite, the LS18Hybrid composite, the LS36Hybrid composite and the LSFGM composite (Loading side was stiffened). Figure 5-15 through 5-18 show the load-displacement curves and the deformations after delamination of the FS9Hybrid composite, the FS18Hybrid composite, the FS36Hybrid composite and the FSFGM composite (Free side was stiffened). Figure 5-19 shows the load-displacement curves and the deformations after delamination of the DS9Hybrid and Figure 5-20 shows the load-displacement curves of other cases in which both sides were stiffened. In the case of the specimens without matrix cracks the location of delamination can be determined as the location of the maximum shear stress. Therefore the location of delamination varied based on the configurations. However, in all cases with matrix cracks the delamination occurred at the 10<sup>th</sup> interface for the case of loading on the stiffer side, at the 6<sup>th</sup> interface for the case loading on the softer side, and at the 8<sup>th</sup> interface when both sides were stiffened (symmetric beam).

## Conclusions

Hybrid composites including FGM composites can reduce the maximum shear stress, and thus can enhance damage resistance. However the un-symmetric FGM composites results in higher maximum shear stress. The effects of reducing the maximum shear stress become noticeable when stiff materials are symmetrically used in both sides. The locations of delamination of the doubly stiffened specimens are identical with the homogeneous composite. However, the delaminations of the singly stiffened specimen occur at the interface toward the stiffened side. Matrix cracks alter the locations of delamination and decrease damage resistance.

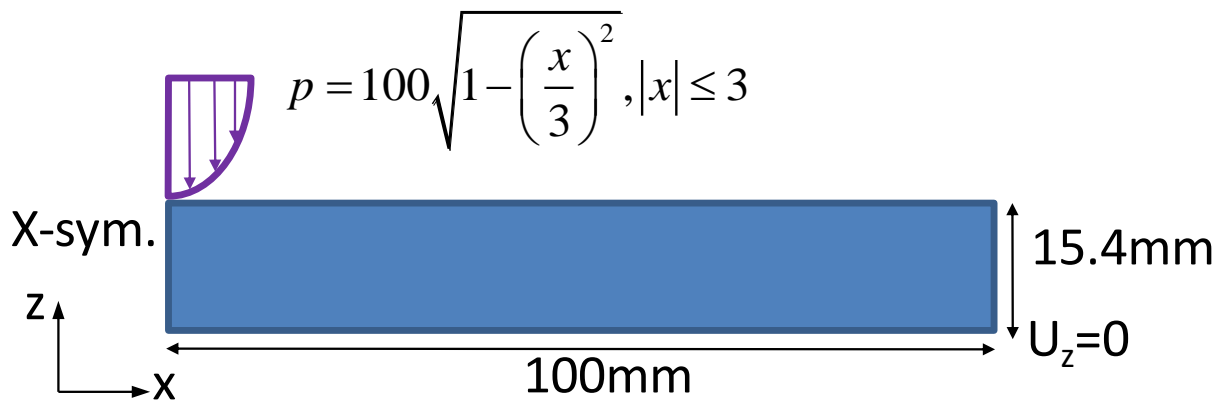


Figure 5-1. FE model to determine the shear stress profile

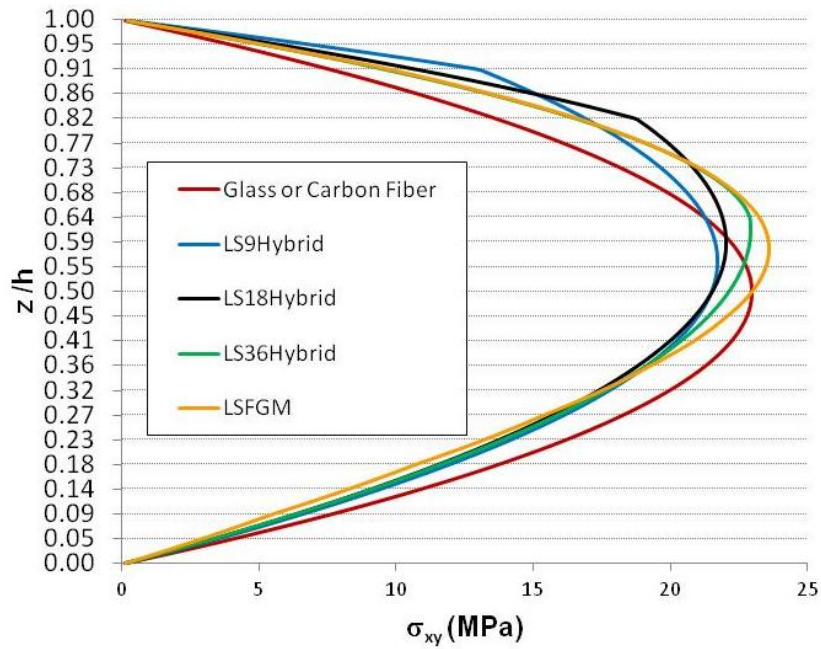


Figure 5-2. Shear stress profiles of the hybrid composites stiffened on the loading side

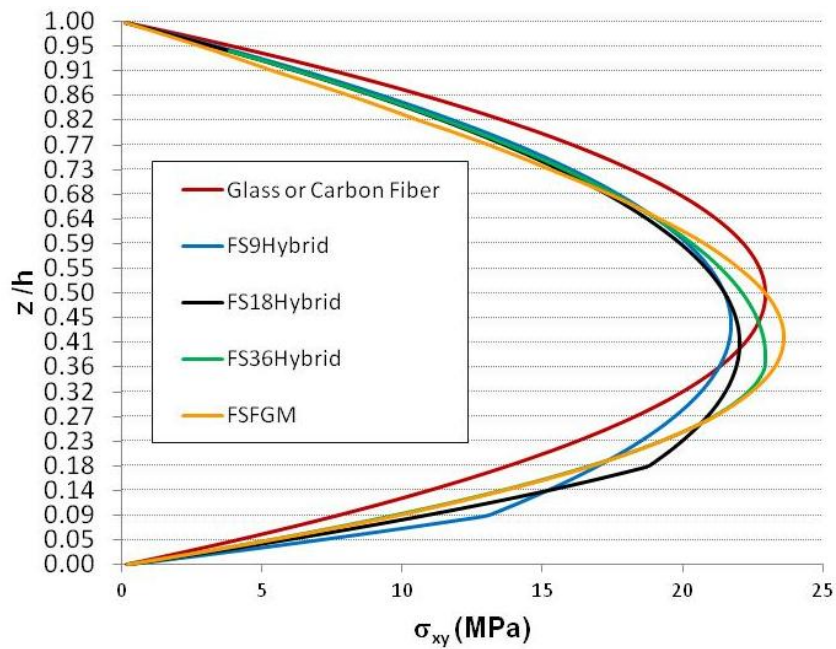


Figure 5-3. Shear stress profiles of the hybrid composites stiffened on the free side

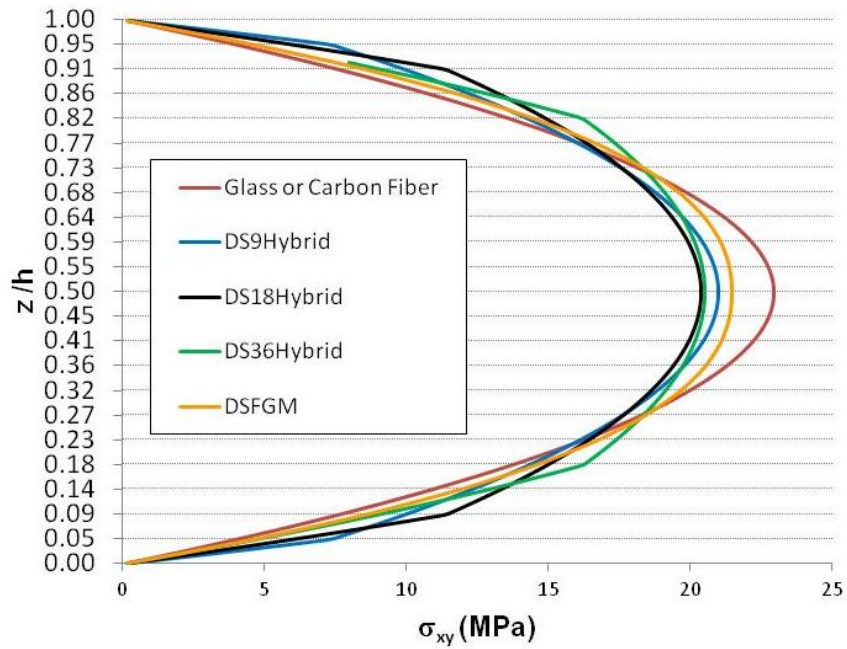


Figure 5-4. Shear stress profiles of the hybrid composites stiffened on the top and bottom sides

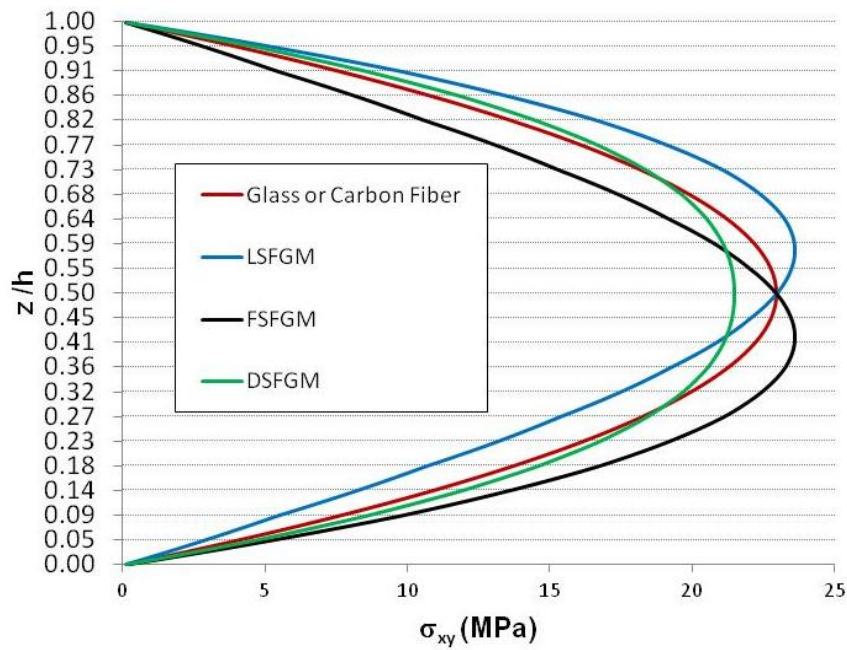


Figure 5-5. Shear stress profiles of homogeneous the FGMs

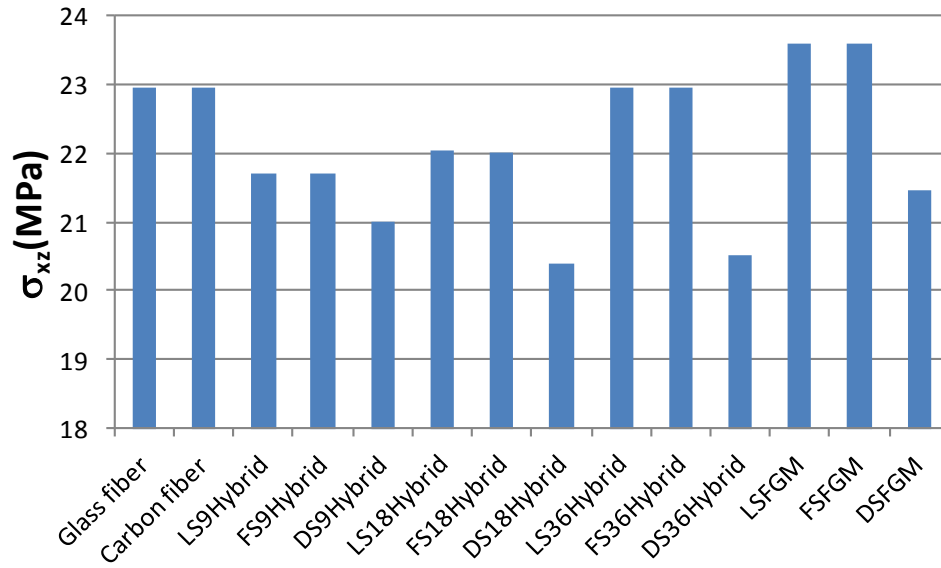


Figure 5-6. The maximum shear stress of various composites

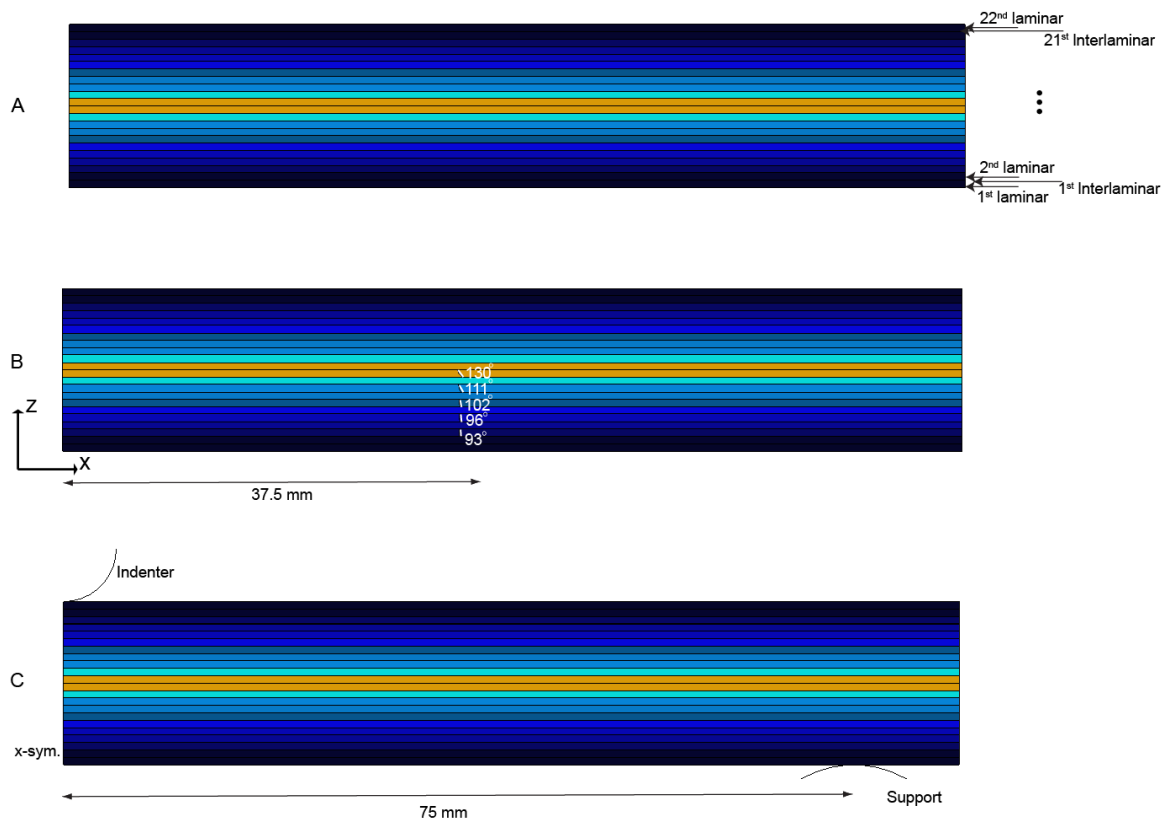


Figure 5-7. The DSFGM specimen. A) Without matrix cracks. B) With matrix cracks. C) FE model to demonstrate the SBS test.

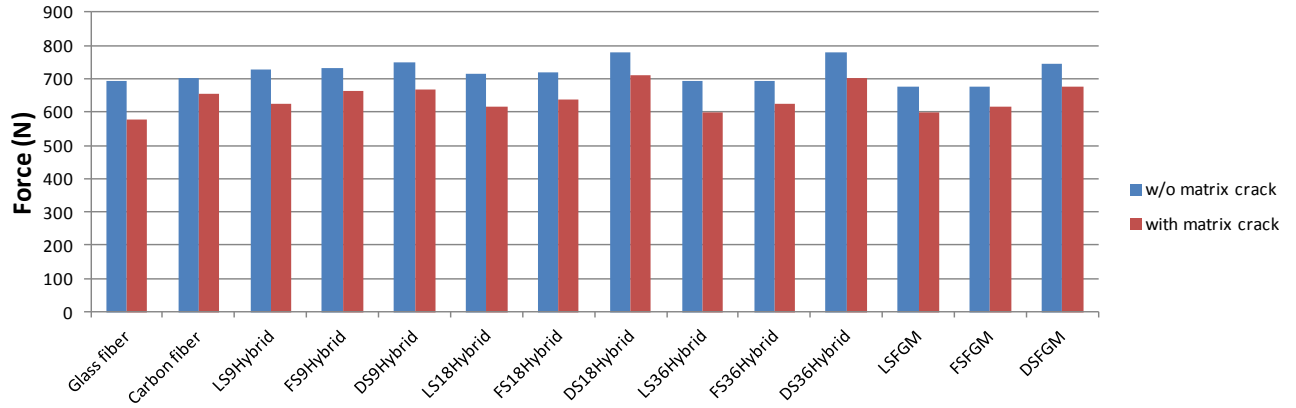


Figure 5-8. Comparison of peak loads of various specimens with and without matrix cracks

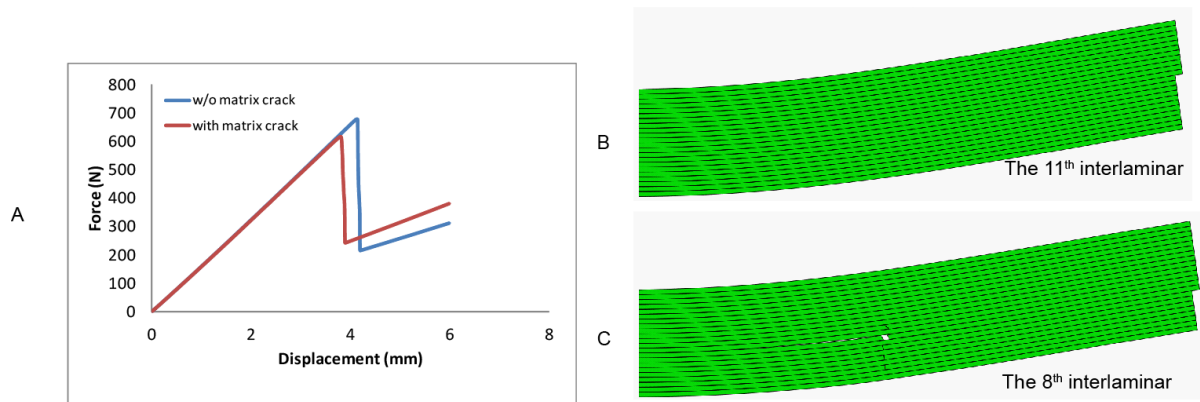


Figure 5-9. The GFC. A) Load-displacement curve. B) Delamination behavior of the specimen without matrix crack ( $d=6\text{mm}$ ). C) Delamination behavior of the specimen with matrix crack ( $d=6\text{mm}$ ), where  $d$  denotes the displacement of the indenter.

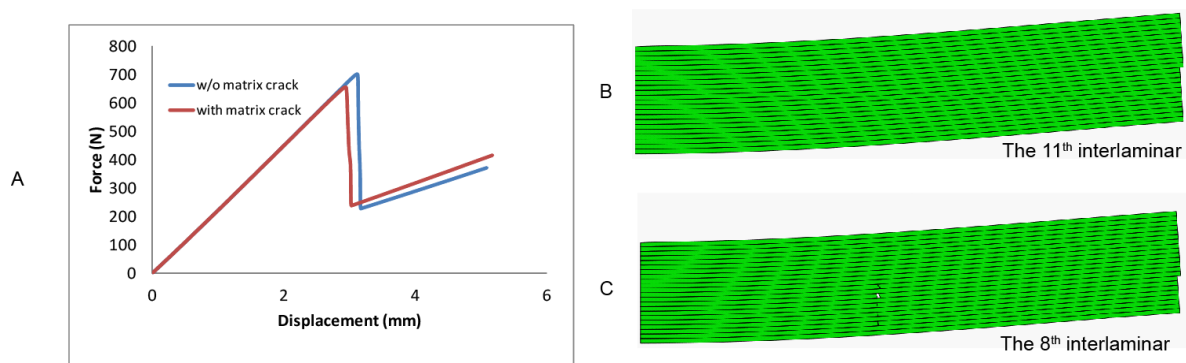


Figure 5-10. The CFC. A) Load-displacement curve. B) Delamination behavior of the specimen without matrix crack ( $d=4\text{mm}$ ). C) Delamination behavior of the specimen with matrix crack ( $d=4\text{mm}$ ).

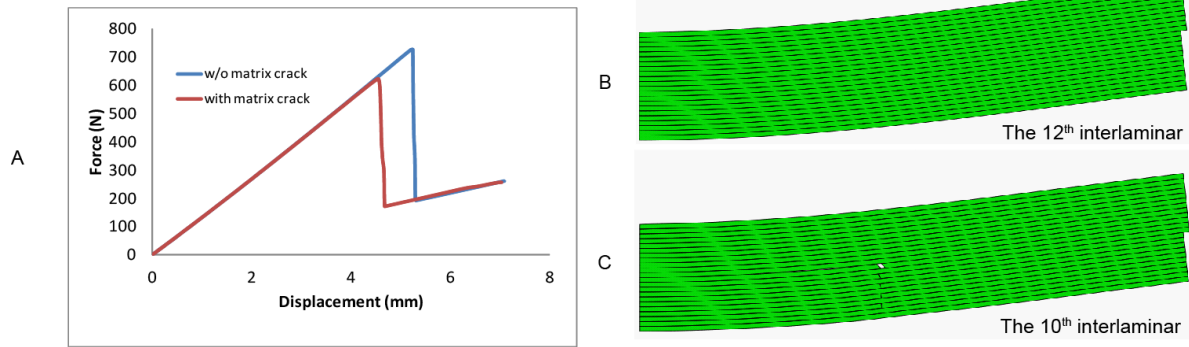


Figure 5-11. The LS9Hybrid composite. A) Load-displacement curve. B) Delamination behavior of the specimen without matrix crack ( $d=6\text{mm}$ ). C) Delamination behavior of the specimen with matrix crack ( $d=6\text{mm}$ ).

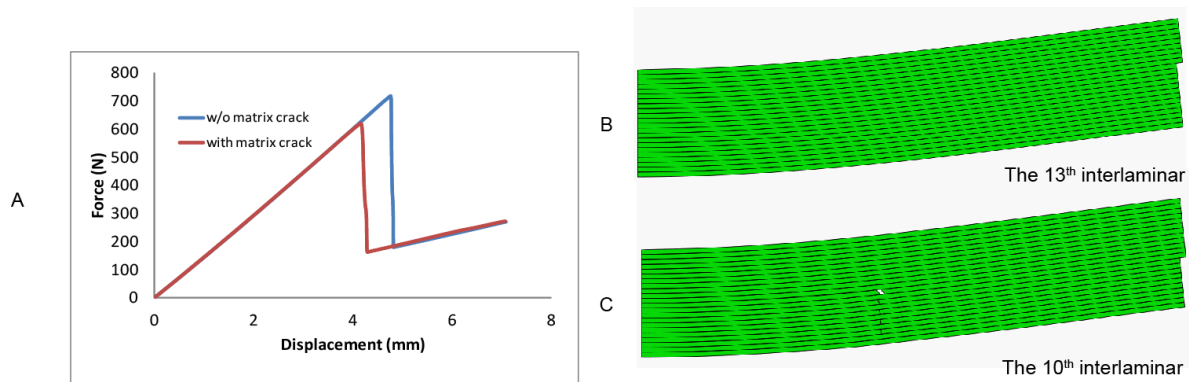


Figure 5-12. The LS18Hybrid composite. A) Load-displacement curve. B) Delamination behavior of the specimen without matrix crack ( $d=6\text{mm}$ ). C) Delamination behavior of the specimen with matrix crack ( $d=6\text{mm}$ ).

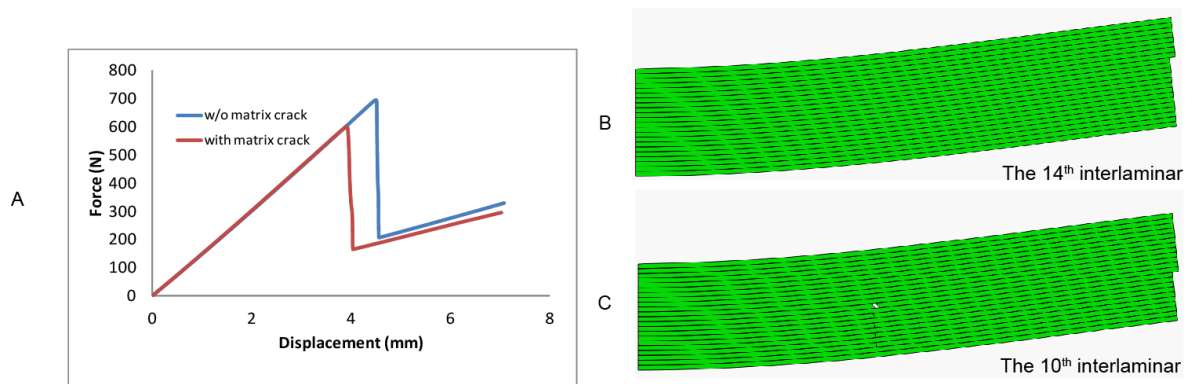


Figure 5-13. The LS36Hybrid composite. A) Load-displacement curve. B) Delamination behavior of the specimen without matrix crack ( $d=6\text{mm}$ ). C) Delamination behavior of the specimen with matrix crack ( $d=6\text{mm}$ ).



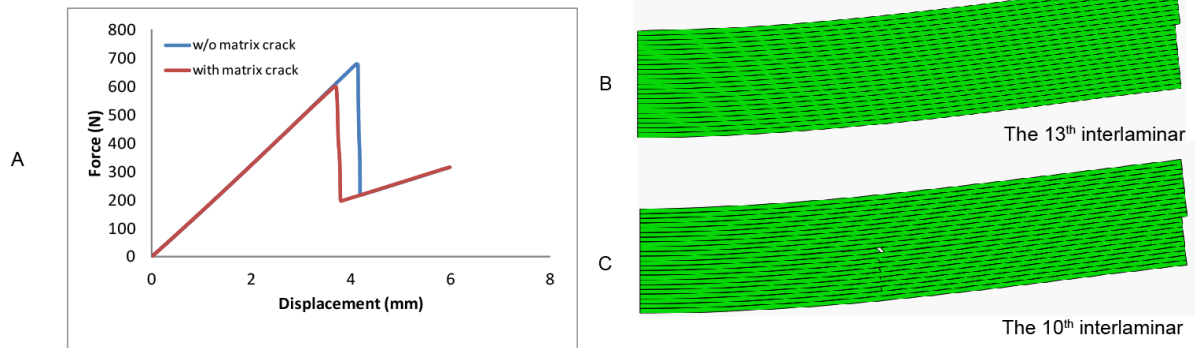


Figure 5-14. The LSFGM composite. A) Load-displacement curve. B) Delamination behavior of the specimen without matrix crack ( $d=6\text{mm}$ ). C) Delamination behavior of the specimen with matrix crack ( $d=6\text{mm}$ ).

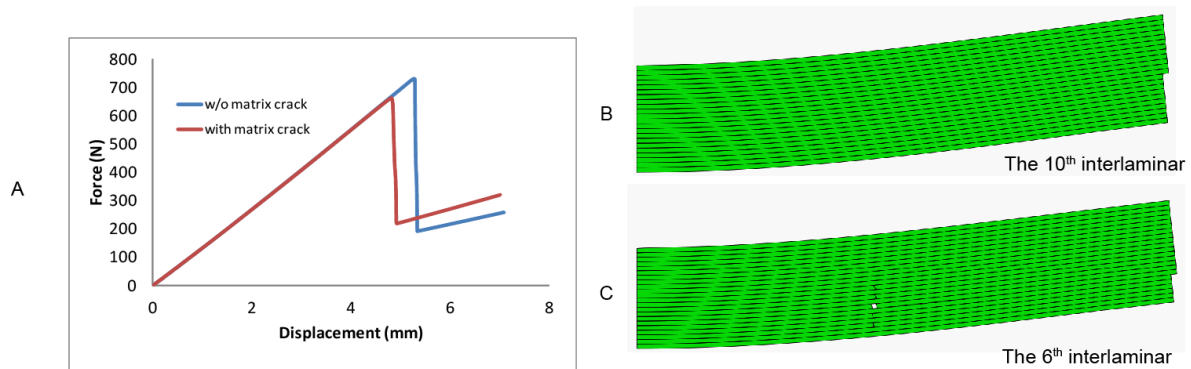


Figure 5-15. The FS9Hybrid composite. A) Load-displacement curve. B) Delamination behavior of the specimen without matrix crack ( $d=6\text{mm}$ ). C) Delamination behavior of the specimen with matrix crack ( $d=6\text{mm}$ ).

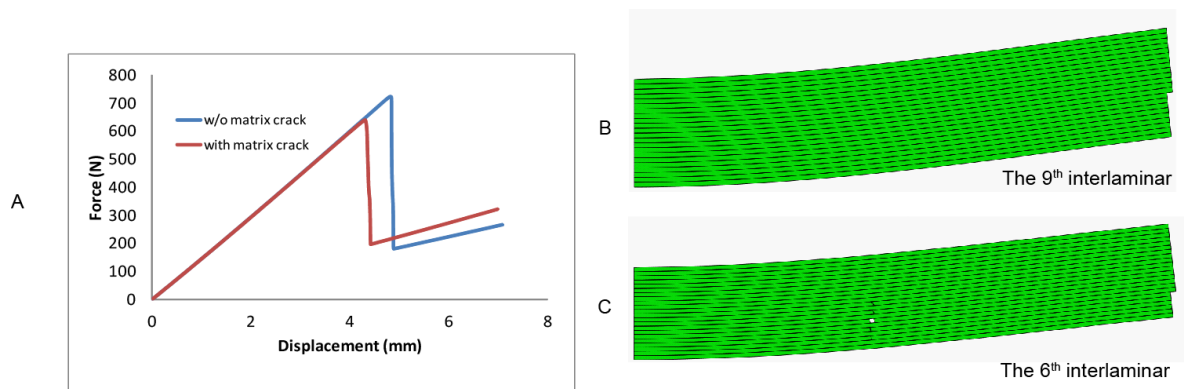


Figure 5-16. The FS18Hybrid composite. A) Load-displacement curve. B) Delamination behavior of the specimen without matrix crack ( $d=6\text{mm}$ ). C) Delamination behavior of the specimen with matrix crack ( $d=6\text{mm}$ ).

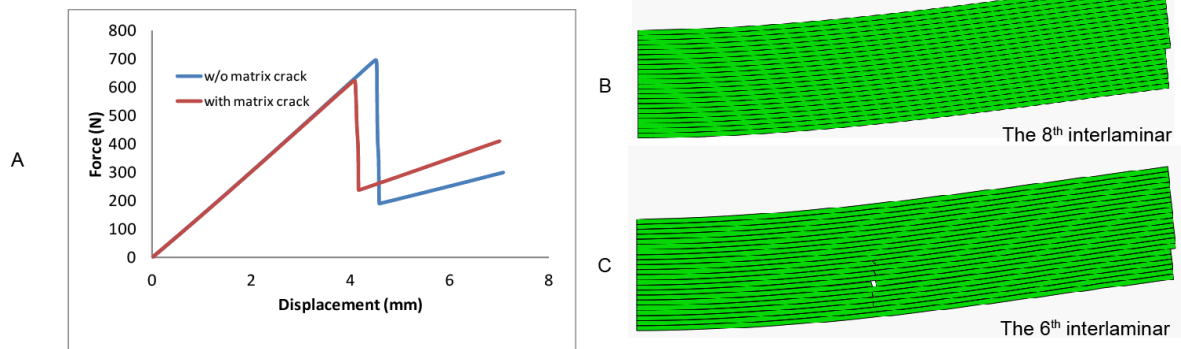


Figure 5-17. The FS36Hybrid composite. A) Load-displacement curve. B) Delamination behavior of the specimen without matrix crack ( $d=6\text{mm}$ ). C) Delamination behavior of the specimen with matrix crack ( $d=6\text{mm}$ ).

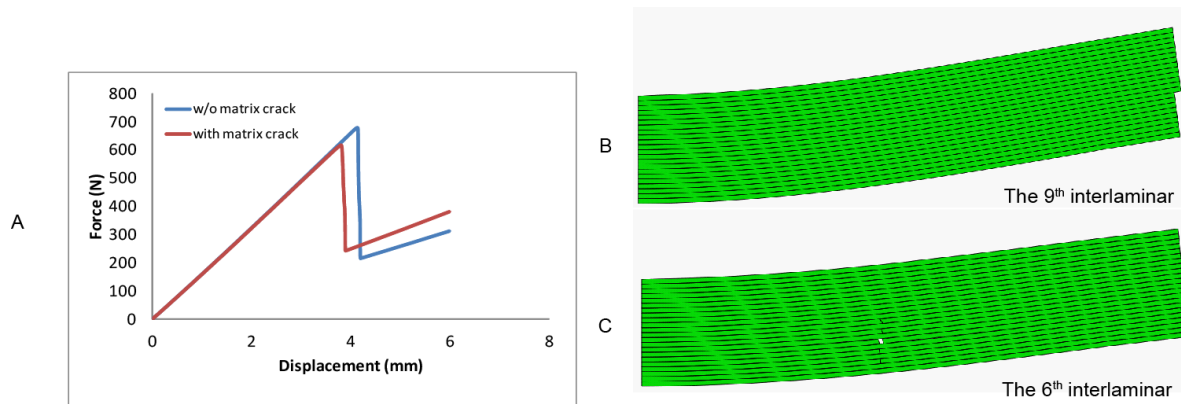


Figure 5-18. The FSFGM composite. A) Load-displacement curve. B) Delamination behavior of the specimen without matrix crack ( $d=6\text{mm}$ ). C) Delamination behavior of the specimen with matrix crack ( $d=6\text{mm}$ ).

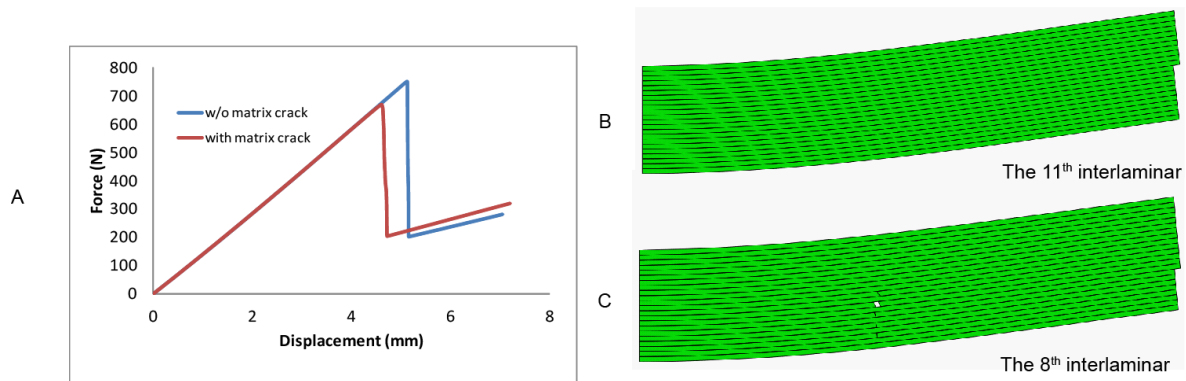
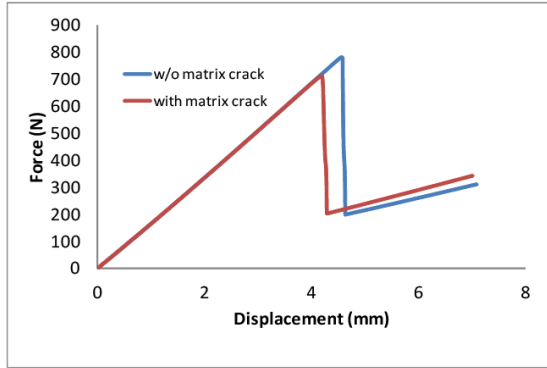
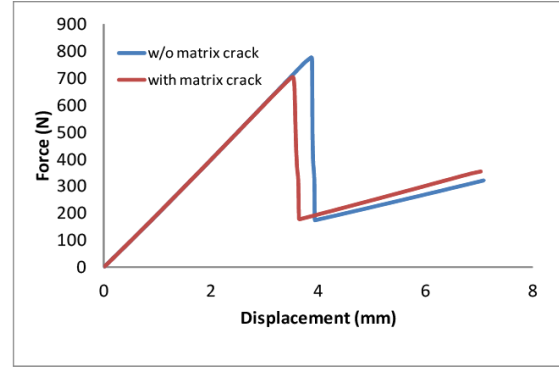


Figure 5-19. The DS9Hybrid composite. A) Load-displacement curve. B) Delamination behavior of the specimen without matrix crack ( $d=6\text{mm}$ ). C) Delamination behavior of the specimen with matrix crack ( $d=6\text{mm}$ ).

A



B



C

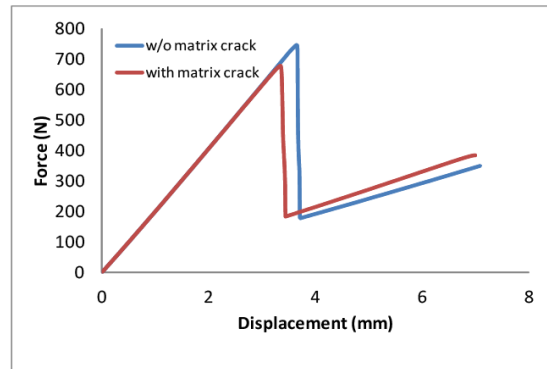


Figure 5-20. Load-displacement curves. A) DS18hybrid. B) DS36hybrid. C) DSFGM:  
The locations of delamination in the symmetric specimens are same as those  
of the DS9hybrid shown in Figure 5-19.

Table 5-1. Various hybrid composite laminates and FGM

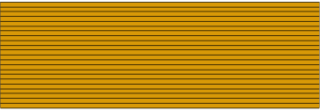
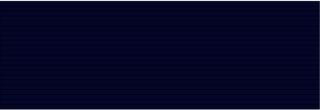




Name	Description
Glass fiber composite	
	Consists of unidirectional glass fiber composites (GFC).
Carbon fiber composite	
	Consists of unidirectional carbon fiber composites (CFC).
LS9Hybrid composite	
	Consists of 9 percent CFC and 91 percent GFC. CFC was placed on the loading side.
LS18Hybrid composite	
	Consists of 18 percent CFC and 82 percent GFC. CFC was placed on the loading side.
LS36Hybrid composite	
	Consists of 36 percent CFC and 64 percent GFC. CFC was placed on the loading side.
FS9Hybrid composite	
	Consists of 9 percent CFC and 91 percent GFC. CFC was placed on the free side (opposite to the loading side).

Table 5-1. Continued






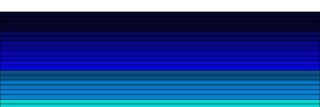
Name	Description
FS18Hybrid composite 	Consists of 18 percent CFC and 82 percent GFC. CFC was placed on the loading side (opposite to the loading side).
FS36Hybrid composite 	Consists of 36 percent CFC and 64 percent GFC. CFC was placed on the loading side (opposite to the loading side).
DS9Hybrid composite 	Consists of 9 percent CFC and 91 percent GFC. CFC was placed on the top and bottom faces (symmetric).
DS18Hybrid composite 	Consists of 18 percent CFC and 82 percent GFC. CFC was placed on the top and bottom faces (symmetric).
DS36Hybrid composite 	Consists of 36 percent CFC and 64 percent GFC. CFC was placed on the top and bottom faces (symmetric).
LSFGM composite 	Volume fraction of CFC is varied from 100 percent at the loading side to 0 percent at the free side in 11 steps.

Table 5-1. Continued

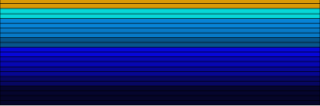

Name	Description
FSFGM composite 	The volume fraction of CFC at layers is varied from 100 percent at the free side to 0 percent at the loading side in 11 steps.
DSFGM composite 	The volume fraction of CFC is varied from 100 percent both at the loading and free side to 0 percent at the center in 11 steps (symmetric).

Table 5-2. Elastic properties for composite materials in the FEM

	$E_1=E_2$ (GPa)	$E_3$ (GPa)	$G_{13}=G_{23}=G_{12}$ (GPa)	$\nu_{13}=\nu_{23}$	$\nu_{12}$
Glass fiber composite	26.9	8.6	3.1	0.28	0.16
Carbon fiber composite	70.0	6.8	3.3	0.15	0.13

## CHAPTER 6 CONCLUSIONS AND FUTURE WORK

### **Conclusions**

It was shown that the damage resistance and tolerance of laminated composites can be enhanced by the employment of translaminar reinforcements (TLR) such as stitching, z-pinning and 3D weaving and also by hybrid composites.

A non-dimensional analytical model focused on Mode I delamination was developed to understand the role of the TLR on delamination behavior. An explicit formula for the apparent interlaminar fracture toughness was derived in terms of the inherent fracture toughness of original materials and the bridging force due to z-pins. This model is capable of estimating the apparent fracture toughness, the bridging length and allowable bridging force thus can be useful in the design of TLR for composite laminates.

Along with understanding advantages of TLR in increasing the damage tolerance of laminated composites, the damage behavior of laminated composites subjected to low velocity impact loading was studied. Based on the similarity in damage development between quasi-static and dynamic loadings observed through the short beam shear (SBS) tests, the FE analyses of the SBS specimens for quasi-static indentation and at several rates of low-velocity impact loadings were performed. The results reveal that inertia effects in the typical velocity range of the striker in SHPB, around 10m/s, can be negligible, and hence the quasi-static analysis is useful and valid in the study of damage in composite specimens under low velocity impact loading.

The delamination behavior of 3D woven composites was investigated focusing on the effect of z-yarn. The 3D woven composites containing both single and double z-

yarns were chosen and compared with the 2D plain woven laminate. The double z-yarn woven composite exhibited enhanced damage tolerance compared to the single z-yarn and the plain woven laminate. The relative sliding motion between two layers is constrained by z-yarns thus the crack propagation of delamination is suppressed. This mechanism increases the apparent interlaminar fracture toughness of the composites.

The interlaminar shear stress profiles in the various hybrid composites were obtained from linear FE analyses and compared within the framework of damage resistance. Some hybrid configurations resulted in reduced maximum shear stress value for a given contact force thus demonstrating higher damage resistance. Although matrix cracks may change the location of delamination and decrease damage resistance, hybrid composites can still be superior in structural applications.

### **Recommendations for Future Work**

It is expected that more studies in these areas would provide a good design tool and insights into application of composite materials in structures subjected to impact loading.

First of all, methodologies for accurate prediction of intralaminar failure in yarns and matrix regions are needed and their implementation in the FE models should be studied. Some useful experimental data provided several assumptions for using cohesive elements in this study. However, an analysis scheme that does not require *a priori* knowledge of crack location would be desirable.

In addition to matrix cracks and delamination, debonding of yarns should be considered although this effect is less than delamination in orthogonal woven composites. The study including debonding can be used in modeling of different types of materials such as angle-interlock composites.



Finally, hybrid woven composites should be analyzed. Each layer and individual yarns can be made of various materials. The synergistic effect due to z-yarns and hybridization should be evaluated for the best performance of composite materials subjected to impact loading.

## LIST OF REFERENCES

- AGY. [http://www.agy.com/technical\\_info/graphics\\_PDFs/Advanced\\_Materials.pdf](http://www.agy.com/technical_info/graphics_PDFs/Advanced_Materials.pdf).
- Applied Poleramic Inc. [http://www.appliedpoleramic.com/specs/vartm\\_rtm.php](http://www.appliedpoleramic.com/specs/vartm_rtm.php).
- Barenblatt GI. The Mathematical Theory of Equilibrium Cracks in Brittle Fracture. *Advances in Applied Mechanics*. 1962; 7: 55-129.
- Belytschko T, Cracie R, Ventura G. A Review of Extended/Generalized Finite Element Methods for Material Modeling. *Modelling and Simulation in Materials Science and Engineering*. 2009; 17(4): 043001.
- Benzeggagh ML, Kenane M. Measurement of Mixed-Mode Delamination Fracture Toughness of Unidirectional Glass/Epoxy Composites with Mixed-Mode Bending Apparatus. *Composites Science and Technology*. 1996; 56: 439–449.
- Boesi BP, Bourne GR, Sankar BV. Insitu Multiscale Analysis of Fracture Mechanisms in Nanocomposites. *Composites Part B*. 2011; 42: 1157-1163.
- Brandt J, Drechsler K, Arendts FJ. Mechanical Performance of Composites Based on Various Three-Dimensional Woven-Fibre Preforms. *Composite Science and Technology*. 1996; 56: 381–386.
- Brandt J, Drechsler K, Filsinger J. Advanced Textile Technologies for the Cost Effective Manufacturing of High Performance Composites. RTO AVT Specialists' Meeting. 1996.
- Byun JH, Gillespie Jr. JW., Chou TW. Mode I Delamination of a Three-Dimensional Fabric Composite. *Journal of Composite Materials*. 1990; 24: 497-518.
- Byrd LW Birman V. The Estimate of the Effect of Z-Pins on the Strain Energy Release rate, Fracture and Fatigue in a Composite Co-Cured Z-Pinned Double Cantilever Beam Composite Structure. 2005; 68: 53–63.
- Byrd LW Birman V. Effectiveness of Z-Pins in Preventing Delamination of Co-Cured Composite Joints on the Example of a Double Cantilever Test. *Composites Part B*, 2006; 37: 365-378.
- Camacho GT, Ortiz M. Computational Modeling of Impact Damage in Brittle Materials. *International Journal of Solids and Structure*. 1996; 33: 2899–2938.
- Camanho PP, Dávila CG, de Moura MF. Numerical Simulation of Mixed-Mode Progressive Delamination in Composite Materials. *Journal of Composite Materials*. 2003; 37(16): 1415–1438.
- Cartié DDR. Effect of Z-fibres<sup>TM</sup> on the Delamination Behaviour of Carbon-Fibre/Epoxy Laminates. PhD thesis. Cranfield University, UK. 2000.

- Cartié DDR, Cox BN, Fleck NA. Mechanisms of Crack Bridging by Composite and Metallic Rods. *Composites Part A*. 2004; 34: 1325-1336.
- Cartié DDR, Anno GD, Poulin E, Partridge IK. 3D reinforcement of Stiffener-to-Skin T-Joints by Z-Pinning and Tufting. *Engineering Fracture Mechanics*. 2006 ; 73: 2532–2540.
- Chamis CC, Handler LM, Manderscheid J. Composite Nanomechanics: A Mechanistic Properties Prediction. NASA/TM—2007-214673, Glenn Research Center, Cleveland, OH. 2007.
- Chang P, Mouritz AP, Cox BN. Flexural Properties of Z-Pinned Laminates. *Composites Part A*. 2007; 38: 244–251.
- Chang P, Mouritz AP, Cox BN. Properties and Failure Mechanisms of Pinned Composite Lap Joints in Monotonic and Cyclic Tension. *Composites Science and Technology*. 2006; 66: 2163–2176.
- Chen L, Sankar BV, Ifju PG. Analysis of Mode I and Mode II Tests for Composites with Translaminar Reinforcements. *Journal of Composite Materials*. 2005; 39: 1311-1333.
- Chen L, Sankar BV, Ifju PG. A New Mode I Fracture Test for Composites with Translaminar Reinforcements. *Composites Science and Technology*. 2002; 62: 1407-1414.
- Cui W, Wisnom MR, Jones M. A Comparison of Failure Criteria to predict Delamination of Unidirectional Glass/Epoxy Specimens waisted through the Thickness.” *Composites*. 1992; 23(3):158-66.
- Dai SC, Yan W, Liu HY, Mai YW. Experimental Study on Z-Pin Bridging Law by Pullout Test. *Composites Science and Technology*. 2004; 64: 2451-2457
- Dantuluri V, Maiti S, Geubelle PH, Patel R, Kilic H. Cohesive Modeling of Delamination in Z-Pin Reinforced Composite Laminates. *Composites Science and Technology*. 2007; 67: 616-631.
- Davila CG, Camanho PP, Turon A. Cohesive Elements for Shells. NASA-TP-2007-214869. 2007.
- Dransfield KA, Baille C, Mai YW. Improving the Delamination Resistance of CFRP by Stitching - A Review. *Composites Science and Technology*. 1994; 50: 305-317.
- Dransfield KA, Jain LK, Mai YW. On the Effects of Stitching in CFRPs—I. Mode I Delamination Toughness, *Composites Science and Technology*. 1998; 58: 815-827.

- Dransfield KA, Jain LK, Mai YW. On the Effects of Stitching in CFRPs—II. Mode II Delamination Toughness. *Composites Science and Technology*. 1998; 58: 829-837.
- Dugdale DS. Yielding of steel sheets containing slits. *Journal of the Mechanics and Physics of Solids*. 1960; 8: 100-108.
- Farley GL, Smith BT, Maiden J. Compression Response of Thick Layer Composite Laminates with through-the-Thickness Reinforcement. *Reinforced Plastics and Composites*. 1992; 11: 787-810.
- Geubelle PH, Baylor J. The Impact-Induced Delamination of Laminated Composites: a 2D Simulation. *Composites Part B*. 1998; 29: 589–602.
- Gibson RF. *Principles of Composite Material Mechanics*. New York: McGraw-Hill, Inc. 1994.
- Gong JC, Sankar BV. Impact Properties of Three-Dimensional Braided Graphite/Epoxy Composites. *Journal of Composite Materials*. 1991; 25: 715-731.
- Grassi M, Zhang X. Finite Element Analyses of Mode I Interlaminar Delamination in Z-Fibre Reinforced Composite Laminates. *Composites Science and Technology*. 2003; 63: 1815–1832.
- Grujicic M, Pandurangan B, Koudela KI, Cheeseman BA. A Computational Analysis of the Ballistic Performance of Light-Weight Hybrid Composite Armors. *Applied Surface Science*. 2006; 253: 730-745
- Hallett SR, Jiang WG, Khan B, Wisnom MR. Modelling the Interaction between Matrix Cracks and Delamination Damage in Scaled Quasi-Isotropic Specimens. *Composites Science and Technology*. 2008; 68: 80-89
- Huang HJ. In-Plane Response and Mode II Fracture Response of Z-Pin Woven Laminates. PhD thesis. Univ. of Michigan. 2008.
- Jain LK, Mai YW. Analysis of Stitched Laminated ENF specimens for Interlaminar Mode II Fracture Toughness. *International Journal of Fracture*. 1994; 68(3): 219-244.
- Jain LK, Mai YW. On the Effect of Stitching on Mode I Delamination Toughness of Laminated Composites. *Composites Science and Technology*. 1994; 51(3): 331-345.
- Jang I, Sankar BV. Analysis of a Composite Double Cantilever Beam with Stitched Reinforcements under Mixed Mode Loading: Formulation (I). *Journal of Mechanical Science and Technology*. 2005; 19(2): 567-577.

- Kalarikkal S, Sankar BV, Ifju PG Effect of Cryogenic Temperature on the Fracture Toughness of Graphite/Epoxy Composites. ASME Journal of Engineering Materials and Technology 2006; 128(2):151-157
- Kim BC, Park SW, Lee DG. Fracture Toughness of the Nano-Particle Reinforced Epoxy Composite. Composite Structures. 2008. 86: 69-77.
- Krueger R. The Virtual Crack Closure Technique: History, Approach and Applications.”, NASA/CR-2002-211628. 2002.
- Kumar P, Singh RK. Impact Damage Area and Interlaminar Toughness of FRP Laminates.”, Adv Compos Mater. 2000; 9: 77–88.
- Kwon YS, Sankar BV. Indentation-Flexure and Low-Velocity Impact Damage in Graphite/Epoxy Laminates”, ASTM Journal of Composites Technology and Research. 1993; 15:101-111.
- Lander JK. Designing with Z-Pins: Locally Reinforced Composite Structures”, PhD thesis. Cranfield University, UK. 2008.
- Mabson GE, Deobald LR. Design Curves for 3d Reinforcement Laminated Double Cantilever Beams. In Mechanics of Sandwich Structure ASME 2000. 2000; 89-99.
- Madhukar MS, Drzal LT. Fiber-Matrix Adhesion and Its Effects on Composite Mechanical Properties: IV. Mode I and Mode II Fracture Toughness of Graphite/Epoxy Composites. Journal of Composite Materials. 1992; 26 (7);936–968
- Mahmood A, Wang X, Zhou C. Modeling Strategies of 3D Woven Composites: A Review. Composites Structure. 2011; 93: 1947-1963.
- McBeath S. Safety Pins. International Journal of Racecar Engineering. 2002; 12: 56-62.
- Mouritz AP, Leong KH, Herszberg I. A Review of the Effect of Stitching on the In-Plane Mechanical Properties of Fibre-Reinforced Polymer Composites. Composites Part A. 1997; 28A: 979-991.
- Mouritz AP. Fracture and Tensile Fatigue Properties of Stitched Fibreglass Composites. Proceedings of the Institution of Mechanical Engineers, Part L: Journal of Materials Design and Applications 2004. 2004; 218: 87.
- Mouritz AP. Review of Z-Pinned Composite Laminate. Composites Part A. 2007 ; 38: 2383-2397.
- Mouritz AP. Tensile Fatigue Properties of 3D Composites with through-Thickness Reinforcement. Composites Science and Technology. 2008; 68: 2503–2510

- Nettles AJ, Douglas MJ. A Comparison of Quasi-Static Indentation to Low-Velocity Impact. NASA/TP-2000-210481. 2000.
- Ling DS, Fang XJ, Cox BN, Yang QD. Nonlinear Fracture Analysis of Delamination Crack Jumps in Laminated Composites. *Journal of Aerospace Engineering*. 2011; 24: 181-188.
- Ling DS, Yang QD, Cox B. An Augmented Finite Element Method for Modeling Arbitrary Discontinuities in Composite Materials. *International Journal of Fracture*. 2009; 156: 53-73.
- Nishikawa M, Okabe T, Takeda N. Numerical Simulation of Interlaminar Damage Propagation in CFRP Cross-Ply Laminates under Transverse Loading. *International Journal of Solids and Structures*. 2007; 44: 3101–3113.
- Okabe T, Yashiro S. Damage Detection in Holed Composite Laminates using an Embedded FBG Sensor. *Composites Part A*. 2012; 43: 388-397.
- Pankow M, Waas AM, Yen CF, Ghiorse S. Resistance to Delamination of 3D Woven Textile Composites Evaluated using End Notch Flexure (ENF) Tests: Cohesive Zone Based Computational Results. *Composites Part A*. 2011; 42(12):1863-1872.
- Rao MP, Sankar BV, Subhash G. Effect of Z-yarns on the Stiffness and Strength of Three-Dimensional Woven Composites. *Composites Part B* 2009; 40:540-551.
- Ratcliffe JG, O'Brien TK. Discrete Spring Model for Predicting Delamination Growth in Z-Fiber Reinforced DCB Specimens. NASA/TM-2004-213019, ARL-TLR-3190. 2004.
- Ratcliffe JG, Kruger RA. Finite Element Analysis for Predicting Mode I-Dominated Delamination Growth in Laminated Structure with through-Thickness Reinforcement. America Society for Composites 21<sup>th</sup> annual technical conference, Dearborn, Michigan. 2006.
- Rice JR. A Path Independent Integral and the Approximate Analysis of Strain Concentration by Notches and Cracks. *Journal of Applied Mechanics*. 1968; 35: 379–386.
- Robinson P, Das S. Mode I DCB Testing of Composite Laminates Reinforced with z-Direction Pins: a Simple Model for the Investigation of Data Reduction Strategies. *Engineering Fracture Mechanics*. 2004; 71: 345-364.
- Rugg KL, Cox BN, Massabò R. Mixed Mode Delamination of Polymer Composite Laminates Reinforced through the Thickness by z-fibres. *Composites*. 2002; 33: 177–190.
- Rybicki EF, Kanninen MF. A Finite Element Calculation of Stress Intensity Factors by a Modified Crack Closure Integral. *Engineering Fracture Mechanics*. 1977; 9: 931–938.

- Rys T, Sankar BV, Ifju PG. Investigation of Fracture Toughness of Laminated Stitched Composites Subjected to Mixed Mode Loading. *Journal of Reinforced Plastics and Composites*. 2010; 29(3): 422-430.
- Sankar BV. Interlaminar Shear Stresses in Composite Laminates Due to Static Indentation. *Journal of Reinforced Plastics and Composites*. 1989; 8(5): 458-471.
- Sankar BV, Hu S. Dynamic Delamination Propagation in Composite Beams, *Journal of Compos Materials*. 1991; 25(11): 1414-1426.
- Sankar BV, Sonik V. Pointwise Energy Release Rate in Delaminated Plates. *AIAA Journal*. 1995; 33(7): 1312-1318.
- Sankar BV, Sharma SK. Mode II Delamination Toughness of Stitched Graphite/Epoxy Textile Composites. *Composites Science and Technology*. 1997; 57: 729-737.
- Sankar BV, Zhu H. The effect of Stitching on the Low-Velocity Impact Response of Delaminated Composite Beams. *Composites Science and Technology*. 2000; 60: 2681-2691.
- Sankar BV, Dharmapuri SM. Analysis of a Stitched Double Cantilever Beam." *Journal of Composite Materials*. 1998; 32: 2204-2225.
- Sankar BV. An elasticity solution for functionally graded beams. *Composites Science and Technology*. 2001; 61: 689-696.
- Sharma SK, Sankar BV. Effect of Stitching on Impact and Interlaminar Properties of Graphite/Epoxy Laminates. *Journal of Thermoplastic Composite Materials*. 1997; 10(3): 241-253.
- Sridhar N, Massabo R, Cox BN, Beyerlein IJ. Delamination Dynamics in through-Thickness Reinforced Laminates with Application to DCB Specimen Delaminated Composite Beams. *International Journal of fracture*. 2002; 118: 119-144.
- Steeves CA, Fleckln NA. In-Plane Properties of Composite Laminates with through-Thickness Pin Reinforcement. *International Journal of Solids and Structures*. 2006; 43: 3197–3212.
- Tan KT, Watanabe N, Iwahori Y. Experimental investigation of bridging law for single stitch fibre using Interlaminar tension test. 2010; 92(6): 1399-1409.
- Tanoglu M, Robert S, Heider D, McKnight SH, Brachos V, Gillespie Jr JW. Effects of Thermoplastic Performing Binder on the Properties of S2-Glass Fabric Reinforced Epoxy Composites. *International Journal of Adhesion & Adhesives*. 2001; 21(3): 187-195.

- Tvergaard V, Hutchinson JW. The Relation between Crack Growth Resistance and Fracture Process Parameters in Elastic–Plastic Solids. *Journal of Mechanics and Physics of Solids*. 1992; 40: 1377–1397.
- Wallace BT, Sankar BV, Ifju PG. Pin Reinforcement of Delaminated Sandwich Beams under Axial Compression. *Journal of Sandwich Structures and Materials*. 2010; 3(2):117-129.
- Walter TR, Subhash G, Sankar BV, Yen CF. Monotonic and Cyclic Short Beam Shear Response of 3D Woven Composites. *Composites Science and Technology*. 2010; 70: 2190-2197
- Walter TR. Characterization of Delamination in 3d Woven Composites under Static and Dynamic loading. PhD thesis. University of Florida. 2011
- Walter TR, Subhash G, Sankar BV, Song MC, Yen CF. A Novel Method for Dynamic Short Beam Shear Testing of 3D Woven Composites. 2012; Submitted
- Wisnom MR, Reynolds T, Gwilliam N. Reduction in Interlaminar Shear Strength by Discrete and Distributed Voids. *Composites Science and Technology*. 1996; 56: 93-101.
- Wong DWY, Lin L, McGrail PT, Peijs T, Hogg PJ. Improved Fracture Toughness of Carbon Fibre/Epoxy Composite Laminates using Dissolvable Thermoplastic Fibres”, *Composites Part A*. 2010; 41: 759–767
- Wu EM, Reuter Jr. RC. Crack Extension in Fiberglass Reinforced Plastics”, T. &AM Report No. 275, University of Illinois. 1965.
- Xiao JR, Gama GA, Gillespie Jr JW Progressive and Delamination in Plain Weave S-2 Glass/SC-15 Composites under Quasi-Static Punch-Shear Loading. *Composite structures*. 2007; 78: 182-196.
- Xu XP, Needleman A. Numerical Simulation of Fast Crack Growth in Brittle Solids. *Journal of Mechanics and Physics of Solids*. 1994; 42: 1397–1434.
- Yan C, Xiao K, Ye L, Mai YW. Numerical and Experimental Studies on the Fracture Behavior of Rubber-Toughened Epoxy in Bulk Specimen and Laminated Composites. *Journal of Material Science*. 2002; 37: 921–927.
- Zhou ZQ, Fang XJ, Cox, BN, Yang QD. The Evolution of a Transverse Intra-ply Crack Coupled to Delamination Cracks. *International Journal of Fracture*. 2010;165: 77-92.



## BIOGRAPHICAL SKETCH

Min Cheol Song [REDACTED] Seoul, South Korea. He attended Sungdong High School. He earned his Bachelor of Science in mechanical engineering in February of 1994 from the Chung-Ang University in Seoul, South Korea. He earned his Master of Science in mechanical engineering February in 2001 from the Korea Advanced Institute of Science and Technology (KAIST) in Daejeon, South Korea. During this period he conducted research on bending collapse of Glass Fiber Reinforced Plastic (GFRP) and Aluminum co-cured square tube. In January of 2001 he joined Agency for Defense Development in Daejeon, South Korea. During this period, he was working on the topic of damage process and phenomena in various materials. He came to the United of States and started his PhD at the University of Florida, Gainesville in the fall of 2008 under the supervision of Prof. Sankar. Mr. Song defended his Doctor of Philosophy in 2012.